

© **2015** Khaldoon Altahhan

MEASURING SPATIALLY VARYING ELASTIC MODULUS OF MULTI-  
COMPARTMENT 3D COLLAGEN SCAFFOLDS USING INDENTATION

BY

KHALDOON NIZAR ALTAHHAN

DISSERTATION

Summited in partial fulfillment of the requirements  
for the degree of Doctor of Philosophy in Theoretical & Applied Mechanics  
in the Graduate College of the  
University of Illinois at Urbana- Champaign, 2015

Urbana, Illinois

Doctoral Committee:

Professor Taher Saif, Chair  
Professor Michael Insana, Director of Research  
Assistant Professor Brendan Harley  
Professor Iwona Jasiuk

## ABSTRACT

Collagen scaffolds with discrete mineralized and non-mineralized regions that are joined by a continuous interface offer great potential for generating a platform with spatially variant stiffness. Once such platforms are seeded with cells, they have been shown to significantly influence cell behavior and differentiation. Accurate elastic modulus measurements of these scaffolds will greatly influence their ability to engineer tissues with varying degrees of stiffness such as tendon-to-bone junctions (TBJ). This thesis presents a novel indentation method as an accurate measurement technique for estimating the intrinsic elastic modulus in 3-D thin-layer collagen scaffolds with varying degrees of stiffness.

Indentation techniques are widely used to characterize the mechanical properties of biological materials. These methods have received considerable attention during the last 20 years because of their simplicity and low cost, but they are challenging to implement. The challenge is to interpret the intrinsic mechanical properties from force-displacement data when studying very soft polymeric media with a volume on the order of a milliliter. It is especially challenging to estimate the elastic modulus of thin-layer scaffolds when the stiffness varies spatially. In this work we use the hydrated indentation method (w/o surface adhesion) to measure the elastic modulus for very soft (<1kPa) polymeric media and for thin-layer 3-D collagen scaffolds.

We build confidence in our approach by first validating the indentation measurements using an elastic hydro-polymer (gelatin gels) through comparisons with other quasi-static indentation

methods (i.e., using surface adhesion) and with dynamic shear-wave imaging estimates.

We then show our modulus measurements can be biased because of coupling with sample boundaries. Finally, we develop a novel inverse approach for correcting the indentation measurement bias near continuously-varying interfaces between mineralized and non-mineralized regions. For this approach we developed a shift-varying Gaussian filter that we used to uncouple the spread in the applied indenter force from the material interface. We established the correction filter using FEA simulation data where indenter is serially applied across a step interface. We argued that due to system linearity the correction filter should apply equally to a step or ramp interface. Intrinsic values of elastic modulus at and near the interface were obtained by solving the inverse problem the correction filter was found. We then tested our technique using FE models for a range of scaffold-like stiffnesses and interface shapes to evaluate the impact of interface width and indenter size on the inverse solution. Our approach significantly reduced indentation measurement bias near step interfaces by more than 60% when using a 2.5 mm-diameter hemispherical indenter. The improvement was more than 35% for a ramp interface using the same indenter size. These improvements are beneficial as a tight control over scaffold mechanical properties is essential for their success in the development of TBJ. The TBJ stiffness changes two orders of magnitude from relatively compliant tendon to bone over a relatively narrow interface region (600-400  $\mu\text{m}$ ). Therefore, accurate elastic modulus measurements of these scaffolds will greatly improve their manufacturing process, and ability to provide a standardized framework for both in vitro interactions between cells and scaffolds and in vivo tissue engineering studies

## **ACKNOWLEDGMENTS**

First, I would like to thank my advisor, Professor Mike Insana for his support and guidance over the last 4 years. I deeply appreciate his mentorship and willingness to take me under his wing in order to help me achieve my dream. I would also like to thank my department advisor, Professor Taher Saif for taking me in and supporting me throughout my PHD journey. Similarly, I would like to thank Professor Brendan Harley for giving me a very interesting topic that added depth and cross-disciplinary dimension to my research experience. Additionally, I would like to thank the rest of my committee members for their valuable inputs and recommendations.

I would like to thank Dr. Nahil Sobh for his generous time and support throughout the years. I would like to thank and acknowledge my colleagues and lab mates who contributed directly to this work, especially Yue Wang, Sara Bahramina and Laura Mozdzen for all their support and professional insights.

Finally, I would like to thank my family for their continuous support and encouragement. Having their support is what kept me going throughout the years.

## TABLE OF CONTENT

List OF SYMBOLS .....	vii
CHAPTER 1: INTRODUCTION .....	1
1.1    3D Collagen Scaffolds & Their Applications in Engineering Multi-Tissue Junctions....	1
1.2    Our Focus .....	4
1.3    Review of Scaffold Mechanical Characterization.....	5
1.4    Objective .....	9
1.5    Impact of This Study .....	10
1.6    Overview .....	11
CHAPTER 2: INDENTATION & CONTACT MODELS .....	13
2.1    Introduction .....	13
2.2    Hertzian Contact.....	14
2.3    Modified Hertzian Contact for Thin-Layered Samples.....	18
2.4    Initial Contact Point Challenge .....	20
2.5    Hertzian Contact with Adhesion .....	22
2.6    Summary and Conclusions.....	26
CHAPTER 3: INDENTATION TECHNIQUES FOR MEASURING ELASTIC MODULUS IN SMALL SAMPLES OF SOFT ELASTIC HYDROGELS – <i>SAMPLE SYSTEM CONCEPT</i> ...	27
3.1    Introduction .....	27
3.2    Gelatin .....	28
3.3    Indentation Experiments .....	31
3.4    Validation with Shear-wave Imaging.....	37
3.5    Numerical Simulation .....	40
3.6    Statistical Analysis .....	42
3.7    Results .....	43

3.8	Discussion .....	48
3.9	Summary & Conclusions .....	53
CHAPTER 4: NEW QUANTITATIVE METHOD FOR MEASURING ELASTIC MODULUS AT INTERFACE REGION OF 3D COLLAGEN SCAFFOLDS WITH VARYING STIFFNESS .....		55
4.1	Introduction .....	55
4.2	Monolithic Scaffold Testing.....	57
4.3	Numerical Simulation of Indentation Using FE.....	60
4.4	New Proposed Method for Correcting Indentation Measurement Bias .....	65
4.5	Results .....	71
4.6	Inverse Solution.....	84
4.7	Discussion .....	88
4.8	Conclusions and Directions for Future Research.....	100
CHAPTER 5: CONCLUSIONS AND DIRECTION OF FUTURE RESEARCH .....		102
5.1	Conclusions .....	102
5.2	Possible Directions for Future Research .....	105
REFERENCES .....		106

## LIST OF SYMBOLS

<u>Abbreviation</u>	<u>Term, Definition</u>
CG	Collagen-glycosaminoglycan
GaP	Calcium Phosphate
CG GaP	Collagen- Glycosaminoglycan with calcium phosphate
ECM	Extra Cellular Matrix
3D	Three Dimensions
MCG	Mineralized Collagen-Glycosaminoglycan
MSC	Mesenchymal Stem Cells
TBJ	Tendon to Bone Junction
JKR	Johnson-Kendall-Roberts
E	Elastic modulus
FE	Finite Element
FEM	Finite Element Model
$f$	Original (intrinsic) function
$\hat{f}$	Predicted function of the inverse problem
$y_{FE}$	Indentation results based on FEM
$y$	Predicted indentation results based on model
$h(x, x')$	Gaussian shift-variant filter

MSE	Mean Square Error
PBS	Phosphate-Buffered Saline
OCE	Optical-Coherence Elastography
$\mu$ CT	Micro-Computed Tomography
$\nu$	Poisson ratio
$R$	Indenter radius
$\delta$	Displacement
$h$	Sample thickness
$\sigma$	Standard deviation

## CHAPTER 1: INTRODUCTION

### 1.1 3D Collagen Scaffolds & Their Applications in Engineering Multi-Tissue Junctions

Mechanobiology is the study of the mechanical environment surrounding cells of the body with respect to cellular growth and development in health and disease. Variations of tissue mechanical properties are strongly correlated with tissue pathology [1,2]. In addition, it has been shown that stem cells differentiate into different cell types based on substrate stiffness. For example, mesenchymal stem cells can differentiate into osteoblast-like cells on substrates with a matrix stiffness of 25-40 kPa. The Extracellular matrix (ECM), also known as the cells' microenvironment, plays a profound role in the tumorigenic potential of cells. Stresses induced by the expansion of tumor cells are magnified by instantaneous changes in the material and structural properties of the tumor microenvironment. The study of mechanobiology has led researchers to begin investigating the role of the environment surrounding cancer cells in tumor development in order to enhance diagnoses and optimize patient treatment. It has also led tissue engineers to focus attention on characterizing microstructures and the mechanical properties of collagen scaffolds because this knowledge can be of clinical use in tissue regeneration and replacements [3].

Many in vitro tissue generations have utilized systems of cell cultures on biomaterial scaffolds in order to address clinical applications for tissue replacements [5]. Engineered tissues must utilize scaffolding biomaterials that support cellular functions and can help promote the development of

appropriate mechanical characteristics of tissues that are of interest [4]. Scaffolds can also potentially serve several additional functions, such as (1) structurally reinforcing the defect, (2) preventing the ingress of surrounding tissues, and (3) acting as a delivery vehicle for cells, growth factors, or genes [5].

Collagen scaffolds are three dimensional porous matrixes which are analogs of the extracellular matrix (ECM) onto which cells attach, multiply, differentiate, and generate new tissue [4]. Scaffold properties such as pore structure, mechanical strength and degradation play important roles in cellular growth and function [6,7]. Scaffold stiffness is shown to affect cellular adhesion, proliferation, infiltration and phagocytic cellular processes [8-11].

Engineering a multi-tissue interface for the purpose of creating a material which stem cells can be seeded onto and go on to differentiate into tendon, bone, and junction (TBJ) compartments, as shown in Figure 1.1, has attracted considerable attention in recent years. Engineered TBJ tissues can serve as an alternative repair process for rotating cuff injuries. TBJ is a critical anatomical joint that transmits force and supports a wide range of motions.

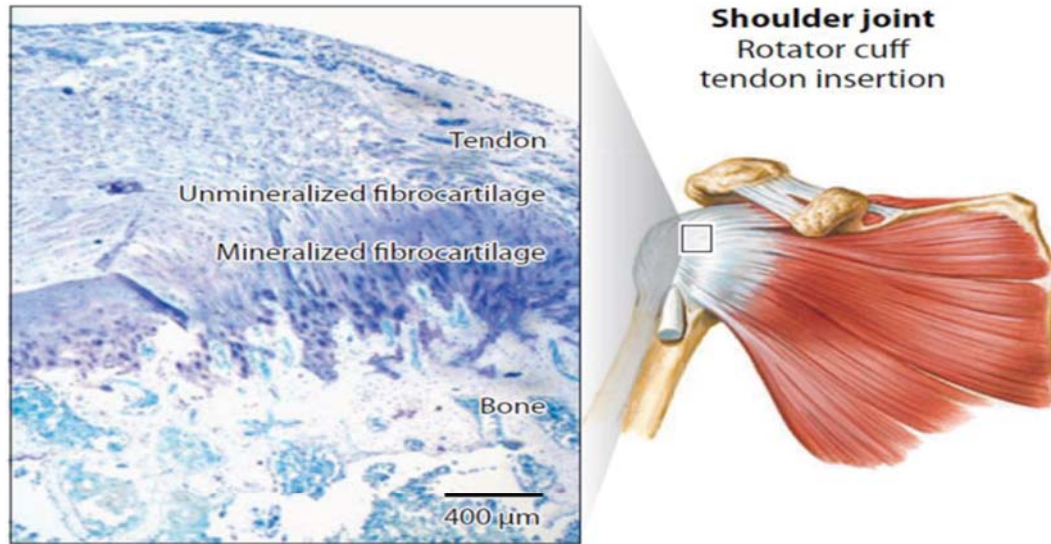


Figure 1.1: Structural anatomy of the TBJ at the rotator cuff consists of tendon and bone bound together by interdigitating non-mineralized and mineralized fibrocartilage [12].

Once TBJ has been subjected to ruptures, it has a very poor repair rate (94% failure rate) using current surgical procedures. Over 75,000 repair surgeries of the TBJ are performed in the US each year [12].

Scaffolds with collagen-glycosaminoglycan CG (red) on the tendon side and mineralized collagen-glycosaminoglycan MCG (blue) on the bone side with stem cells is illustrated in Figure 1.2.

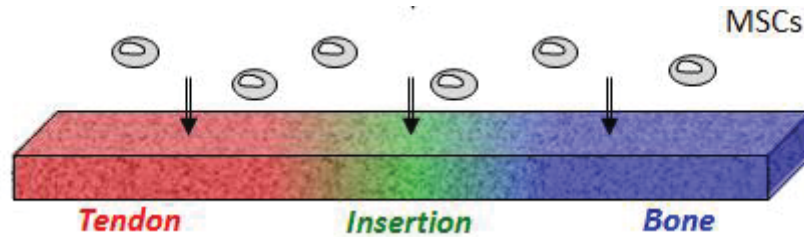


Figure 1.2: Schematic illustrating bilayer collagen scaffold with MCG (blue) at the bone side and CG (red) at tendon side, MSCs are presenting stem cells. This image is from Dr. Harley lab group at U of I.

This emerging subfield of tissue engineering presents a unique challenge to scientists as stiffness changes two order of magnitude away from relatively compliant tendons to bone tissues over a relatively short interface region. Critical questions thus need to be answered regarding methods of fabricating and characterizing the mechanical properties of such composite scaffolds.

## 1.2 Our Focus

The need to fabricate spatially varying stiffness scaffolds is compelling, as described above. It remains unclear how to go about quantifying stiffness variations throughout the scaffold, particularly at the interface region. Our work seeks to develop accurate numerical models for quantifying the spatial variations of scaffold stiffness. These findings will be employed in refining the fabrication process of scaffolds.

We begin working on the challenge by initially developing a measurement technique for accurately determining the elastic modulus of monolithic collagen-glycosaminoglycan CG and

mineralized collagen-glycosaminoglycan MCG scaffolds. Second, we develop and validate a numerical simulation model for the monolithic scaffold. Third, we use the validated simulation model to investigate an inverse technique for depicting the interface region between the CG and MCG.

### 1.3 Review of Scaffold Mechanical Characterization

Collagen scaffolds are fabricated using a freeze-drying slurry containing a co-precipitate of collagen and glycosaminoglycan for CG generation [2] and a co-precipitate of calcium phosphate, collagen and glycosaminoglycan for MCG [12]. Scaffolds with pore structures often resemble low-density, open-cell foams with interconnected networks of struts. Models describing the mechanical behavior of cellular solids such as open-cell foams are well-developed [13]. Gibson and Ashby present a stress–strain curve for low-density elastomeric open-cell foam in compression, as depicted in Figure 1.3. The curve is characterized by three distinct regimes: a linear elastic regime (controlled by strut bending), a collapse plateau regime (struts buckling and pore collapse) and a densification regime (complete pore collapse throughout the material).

Young’s modulus  $E^*$  and compressive plateau stress  $\sigma_{el}^*$  are defined by [13]

$$E^* = C_1 \left(\frac{\rho^*}{\rho_s}\right)^2 E_s, \quad (1.1)$$

$$\sigma_{el}^* = C_2 \left(\frac{\rho^*}{\rho_s}\right)^2 E_s, \quad (1.2)$$

where  $C_1 \sim 1$  and  $C_2 \sim 0.05$  are related to cell geometry,  $E^*$  and  $\sigma_{el}^*$  are the elastic modulus and compressive strength of the scaffold respectively.  $E_s$  is the Young modulus of the solid from which the foam is created.  $E^*$  and  $\sigma_{el}^*$  are related to  $(\rho^*/\rho_s)^2$ , the square of the relative density

between the foam ( $\rho^*$ ) and the solid from which it is made ( $\rho_s$ ), and is not related to cell geometry or pore size [13].

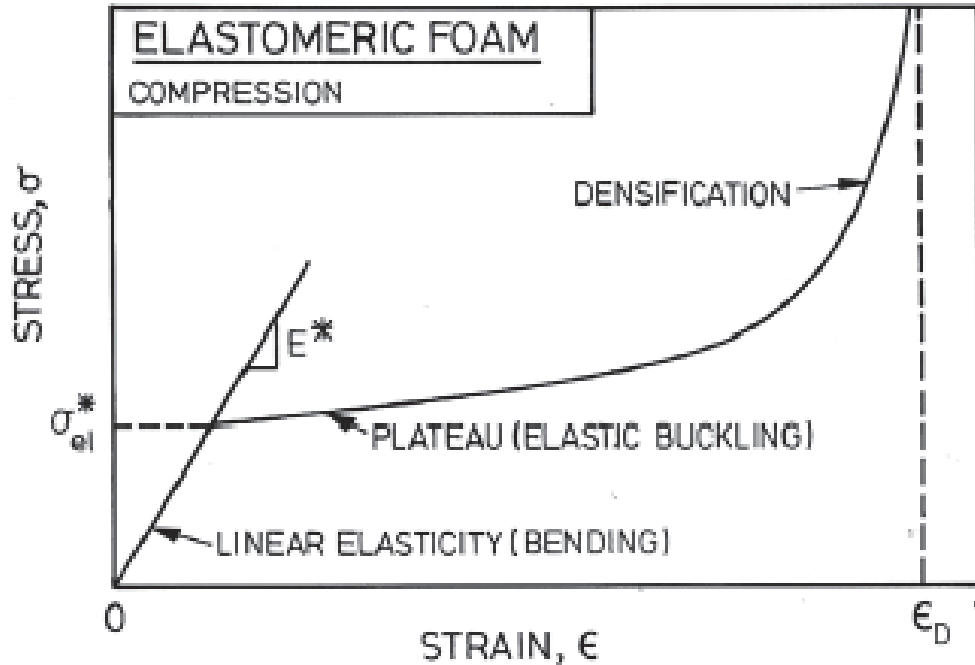


Figure 1.3: Schematic showing linear elastic, collapse plateau and densification phases for compressive stress–strain curve of an elastomeric cellular solid. [13,14]

In tension, the initial linear elastic response is typically the same as is observed in the compression of small strains (<5%). However, as the strain increases, the struts become increasingly oriented in the direction of applied tension, which increases the stiffness until tensile failure occurs [6,7,8,14].

Young’s modulus and the compressive strength of CG scaffolds are of great interest because they impact differentiation, mobility and contraction. Fibroblasts have been shown to bend and buckle individual struts within the scaffold [20,28].

Recent research in this area has taken two different approaches. The first approach focuses on combining microstructure and indentation. It uses the cellular solid low-density open foam model discussed above to characterize the Young modulus, pore size and compressive stiffness. Indentation is used as a secondary tool to help validate results obtained from the microstructure study. The second approach focuses on appropriate contact models of indentations for processing force deflection and predicting elastic modulus values.

Following the first approach, (Harley, et al., 2007)[14] showed that scaffolds with equiaxed pores were found to be mechanically isotropic.

There was good agreement in Young modulus prediction using the cantilever bending test of a single strut, and using open cell foam, in comparison with the elastic modulus values derived from the compression test.

The open-cell foam model over-predicted the measured moduli at  $\left(\frac{\rho^*}{\rho_s}\right)$  values higher than 0.0058, which is most likely due to regions of heterogeneities observed for the higher density scaffolds.

A researcher (Kanungo, et al., 2008) [15,21] similarly characterized the microstructural and mechanical properties of newly-developed mineralized collagen scaffolds for bone regeneration using indentation.

Kanungo confirmed that isotropic mechanical properties scaffolds had equiaxed pore structures. The elastic modulus and strength of individual struts within the scaffolds were measured using an atomic force microscopy cantilevered beam-bending technique and compared with the composite response under indentation and unconfined compression.

Cellular solids models which measured strut properties overestimated the Young modulus for the scaffolds. The discrepancy arises from defects such as disconnected pore walls within the scaffold.

A similar approach was used by Harley (Weisgerber, et al., 2013) [17]. They extended his evaluation of the collagen scaffold mechanical properties to scaffolds with 80 wt% CaP. He analyzed scaffold stiffness variants while increasing mineral content from 40 to 80 wt% CaP. He also showed that individual mineralized and non-mineralized compartments differentially impacted the global properties of the multi-compartment composite. He concluded that the elastic modulus and permeability of the entire construct were governed primarily by the non-mineralized and mineralized compartments respectively, and stated that more effort should be focused on the spatial structural and compositional variations in scaffolds, in order to better understand mechanical properties, which are an important design parameter in orthopedic interface repairs.

The second approach (Martinez-Diaz, et al., 2010) [22] involved in vivo evaluation of polycaprolactone scaffolds in the case of cartilage repair in rabbits, where they used indentation equipment (Seiko Instruments, Inc., Chiba, Japan) with a 1-mm diameter stainless steel probe. Their indentation results were compared with the results of the compression tests in the case of the open foam cell model, and showed that the elastic modulus of the regenerated tissue matched those of the normal articular cartilage (native control). A linear fit of 10% of the initial indentations and stress-strain curves of the loading was constructed from the experimental data in order to determine the Young modulus of all of the cartilage samples. A Poisson's ratio of 0.4

was used to compute the elastic modulus from indentation tests, as has been reported by others [23-25]

Another researcher (Zhu, et al., 2011) [26] presented a quantitative investigation of the stiffness of rat tail collagen type I fibrils at room temperature using AFM nano-indentation. The results were valid for homogeneous, isotropic, and linear material.

This work concerns mapping the stiffness variation along the interface region between mineralized and non-mineralized compartments scaffolds. We follow the second approach, outlined above, by focusing on measuring the intrinsic elastic modulus of the bulk material using macro-indentation. We limit the macro-indentation depth to less than 10% in order to stay within the linear regime limits [13]. In order to prove the feasibility of using macro-indentation to measure materials of low stiffness (elastic modulus  $< 600\text{-}800$  Pa), we begin by intending gelatin hydrogel with different stiffness ranges (gelatin concentration ranging from 2% to 8%, percentage refers to the water weight ratio). We validated the gelatin indentation results with other measurement techniques such as shear-wave elasticity-imaging methods. We intend to leverage the validated indentation technique as a stepping stone for improving the mechanical prediction properties of both the CG and MCG scaffolds and define the pathway for accurately determining the elastic modulus at the interface zone between them.

#### **1.4 Objective**

This thesis seeks to characterize the elastic modulus of the interface region of porous, mineralized and non-mineralized type I collage scaffolds for the application of engineering

tendons of varying degrees of stiffness. This work focuses on developing a method for the accurate measurement of the elastic modulus of 3d collagen scaffolds in order to precisely control and quantify stiffness changes throughout the scaffold, particularly the interface region, which is a substantial area of biomaterial research on tissue repair and replacement. Our aims are:

1. To develop a millimeter-scale indentation technique that offer estimates of the intrinsic elastic modulus of the 3D hydrated collagen scaffold.
2. Minimize the effect of the boundary condition and heterogeneity on elastic modulus measurements.
3. Map heterogeneity using indentation in order to obtain the spatial stiffness gradients of multi-compartment scaffolds.

### **1.5 Impact of This Study**

Approaches to ligament-bone repairs have substantial implications beyond orthopedics. One important area of clinical need is the reconstruction of oral and craniofacial defects, particularly tooth-ligament-bone connections. Advances in these fields hinge on the ability to control 3D collagen scaffold stiffness. Detailed mechanical characterization of these scaffolds constitute a pathway for standardizing manufacturing processes that can deliver needed spatially gradient tissue.

Improving the ability to measure the mechanical properties of collagen scaffolds will greatly broaden their range of potential applications, and will constitute a substantial step toward biomaterial research on tissue repair and replacement. The results of this study can also be useful

for characterizing cell behavior in standardized environments. Characterization of the stiffness of the CG scaffold allows us to determine the effect of the stiffness in the context of a more realistic 3-D environment on cell migration speed [27,28], and promote the development of scaffolds appropriate for mesenchymal stem cell [29] and orthopedic applications [30].

## **1.6** Overview

This thesis is organized as follows. This chapter discussed the connection between biology and the mechanical field. We highlighted the application of collagen scaffolds for tissue engineering and how it can be used to generate tissues of varying degrees of stiffness. Next, we analyze potential applications in the development of new TBJ repairs for rotating cuff injuries. Next, we present literature reviews for the purpose of evaluating mechanical properties and the Young modulus for scaffolds.

Finally, we summarize our study objective and the potential impact on advancement of tissue engineering. In the subsequent indentation and contact models chapter, we provide a thorough description of existing analytical contact models and their limitations. After this, we present the application of these techniques for measuring elastic modulus in small samples of soft elastic hydrogels. We then introduce the concept of a sample system in order to highlight the coupling between measurement, sample geometry and stiffness. Chapter 4 reviews the manufacturing process for CG and MCG scaffolds and the appropriate indentation model that should be used in order to address scaffold thickness.

We then examine the challenge of measuring the elastic modulus for bilayer collagen scaffold for the interface zone using finite elements modeling, where we examine how the measurements are biased due to material heterogeneity. We next present an innovative approach to account for the

bias and proceed to obtain the elastic modulus by solving the inverse problem. Chapter 5 will present our conclusions, a summary of our work and a proposal for future research.

## CHAPTER 2: INDENTATION & CONTACT MODELS

### 2.1 Introduction

Indentation techniques have been widely applied to characterize biological materials, and have received considerable attention during the last 20 years. The use of atomic force microscopy in materials research has established micro-indentation and nano-indentation as two of the leading techniques for the mechanical characterization of material through elastic modulus prediction. AFM has been the focus of recent studies that have sought to understand mechano-transduction within individual cells [31, 32]. Recent advances involve using applied load, indentation displacement, and contact radius based on Hertzian contact to estimate the elastic modulus of finite-volume soft polymers in situations where they deform linearly [33]. Hertzian analysis is limited to homogenous, semi-infinite, elastic materials, while modified Hertzian-contact models have been developed to account for violations of these assumptions. Dimitriadis, et al., [34] applied correction factors to the Hertzian-contact equation in order to estimate an elastic modulus from force-displacement curves in thin-layer samples. Johnson, et al., [35] modified Hertzian-contact theory to include the influences of adhesion energy such as the indenter-tip first contacts and later releases the sample surface. A review of contact models is offered by Lin, et al. [36].

## 2.2 Hertzian Contact

It is well established practice to rely on models based on classical Hertzian theory, which assumes linear elasticity and infinitesimal strains when being used to analyze indentation force displacement curves.

Geometrical effects on local elastic deformation properties have been considered as early as 1880 with the Hertzian Theory of Elastic Deformation [33]. Hertzian theory relates the circular contact area,  $a$ , of a sphere with radius,  $R$ , acting on a plane to the elastic deformation properties of the materials. This can be illustrated by following the analysis put forward by Landua and Lifshitz (1959) [38] and from the book on Contact Mechanics and Friction by V.L. Popov (2010) [39]. As illustrated in Figure 2.1, A spherical probe of radius  $R$  applies force  $F$  in downward direction on a half-space elastic medium, and this will result in  $u_z$ , which can be given for a point on the surface in the contact area with Equation 2.1

$$u_z = d - \frac{r^2}{2R}, \quad (2.1)$$

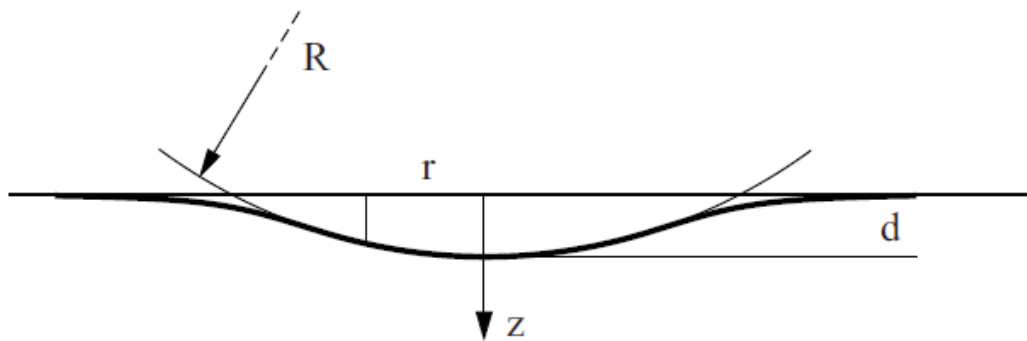


Figure 2.1: Contact between a sphere of radius  $R$  and half-space elastic medium  $d$ , free surface deformation and  $r$ , radius of contact area.

In order to relate the acting force  $F$  to the deformation  $d$  of the half –space we consider the following:

Let  $F$  be a force acting on the free surface of a half-space elastic medium, Figure 2.2, such that the displacement at the origin in the positive  $z$ -direction is given by Equation 2.2

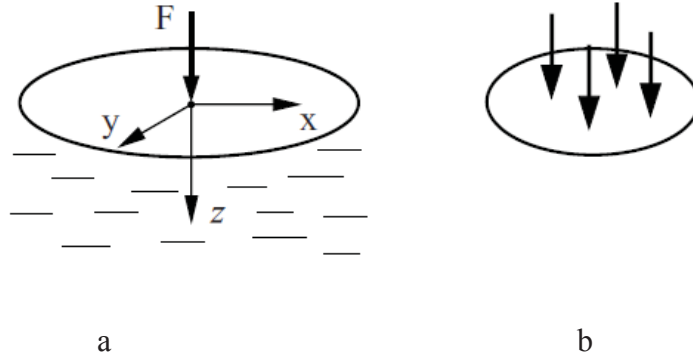


Figure 2.2: (a) Force acting on an elastic half space ; (b) system of forces acting on the surface

$$u_z = \frac{1+\nu}{2\pi E} \left[ \frac{2(1-\nu)}{r} + \frac{z^2}{r^3} \right] F_z, \quad (2.2)$$

where  $r = \sqrt{x^2 + y^2 + z^2}$ , as  $z = 0$  at the free surface  $u_z$  becomes

$$u_z = \frac{(1-\nu^2)}{\pi E} \frac{1}{r} F_z, \quad (2.3)$$

When several forces act simultaneously as shown in Figure 2.2b, a pressure distribution of the form

$$P = P_0 \left( 1 - \frac{r^2}{a^2} \right)^{1/2}, \quad (2.4)$$

will result in vertical displacement  $u_z$

$$u_z = \frac{(1-\nu^2)\pi P_0}{4Ea} (2a^2 - r^2), r \leq a, \quad (2.5)$$

The total force will be

$$F = \int_0^a P(r)2\pi r dr = \frac{2}{3}P_0\pi a^2, \quad (2.6)$$

Substituting  $u_z$  in Equation 2.1 based on the quadratic distribution of the vertical displacement resulting from the pressure distribution shown in Equation 2.4

$$\frac{(1-\nu^2)\pi p_0}{4Ea} (2a^2 - r^2) = d - \frac{r^2}{2R}, \quad (2.7)$$

This result is that  $a$  and  $d$  fulfill the following requirements:

$$a = \frac{\pi P_0 R (1-\nu^2)}{2E}, \quad d = \frac{\pi a p_0 (1-\nu^2)}{2E}, \quad (2.8)$$

$$\text{It follows that for the contact radius } a^2 = Rd, \quad (2.9)$$

$$\text{And for maximum pressure } P_0 = \frac{2(1-\nu^2)}{\pi} \left(\frac{d}{R}\right)^{1/2}, \quad (2.10)$$

Substituting from (2.10) and (2.9) into (2.6), we obtain the Hertzian force to be

$$F = \frac{4}{3} \frac{E}{(1-\nu^2)} R^{1/2} d^{3/2}, \quad (2.11)$$

Substituting  $F$  back into (2.9) and (2.10), we obtain the pressure at the center of the contact as well as the contact radius as a function of the normal force.

$$P_0 = \left(\frac{6FE^2}{\pi^3 R^2 (1-\nu^2)^2}\right)^{1/3}, \quad a = \left(\frac{3FR(1-\nu^2)}{4E}\right)^{1/3}. \quad (2.12)$$

Equation 2.11 shows that force displacement curve of indentation can be an effective means of predicting an elastic modulus of the sample by measuring both force and displacement during indentation and performing some type of curve fitting [33]. However, this is not easy. The process of determining the elastic moduli of soft materials faces two major challenges [34, 36, 37]. The first challenge is related to the incorporation of a finite-size sample's boundary conditions, Figure 2.3.

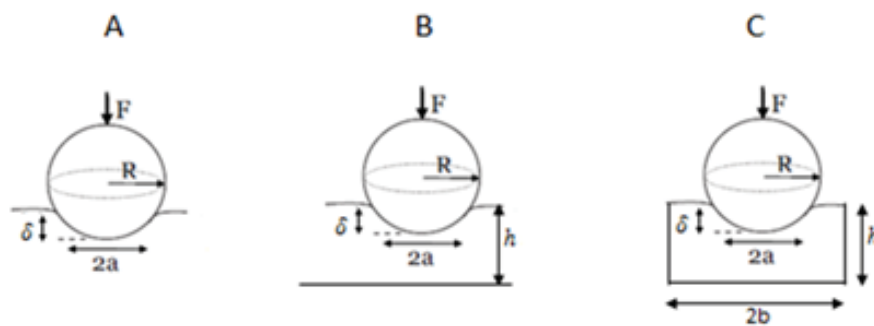


Figure 2.3: Boundary conditions challenge as the boundary moves away from its original half space assumption (A) to an infinite thin layer (B) to a bounded sample (C).

In the course of developing his theory, Hertz made some simplifying assumptions which can be summarized as follows:

- a) Indentation is applied on a half-space ( no boundary condition effect on the solution)
- b) Surfaces are continuous and non-conforming (i.e., initial contact is a point or a line)
- c) Surfaces are frictionless
- d) Strains are small less than 10%
- e) Solids are elastic

In the fields of soft tissue engineering and cell culture development, it is impossible to satisfy the first major assumption mentioned in a). Therefore, over the years several contact models were

developed in order to address these limitation and facilitate the use of Hertzian theory as the basis of an indentation technique and as a means of evaluating material stiffness. In 2002 Dimitriadis, et al., [34] developed a novel approach to addressing three problems which limit the use of the Hertzian contact model when indenting soft materials. The following two sections discuss several relevant modifications of Hertzian contact in order to assist the use of indentation for the purpose of measuring the elastic moduli of soft materials.

### **2.3 Modified Hertzian Contact for Thin-Layered Samples**

Assumptions about infinite specimen thickness impose severe restrictions on the analysis of indentation data for thin specimens, such as collagen scaffolds, the subject of our study.

Collagen scaffold are manufactured with 5-6 mm of thickness and enforcing Hertzian restrictions necessitates very low indentation ranges which are close to the noise range of the indenter used, and this complicates indentation data analysis.

It is possible to reduce the sphere size  $R$  as a means of enforcing Hertzian assumptions. Very small probe tips with radii in the nm-range pose the risk of not obtaining any reliable measurements. They will fall inside the pore for such prose materials, or obtain only very local responses when pushing against one trust structure. The ultimate objective is to seed the scaffold with cells and mentoring how cells proliferate with substrates that have different degrees of stiffness. Contributions from the substrate can cause permanent damage to the scaffold tissue.

Having an optimum range of  $R$  that is between 2.5 and 0.625 mm will ensure low stress concentrations in the tissue specimens, and will also assist in averaging local tissue heterogeneity. Due to these practical experimental difficulties, it becomes necessary to account

for the inevitable violations of Hertzian theory assumptions in the contact modeling framework. The most seminal contribution in this field is the work of Dimitriadis and his co-workers.

Dimitriadis, et al., appended correction terms to the Hertz contact model, and this led to the discovery of an analytical force-indentation relationship. They derived Green's function for an infinite thickness sample bounded to the substrate and used that to compute the approximate indentation. Details of mathematical development are presented in [34], and are given by

$$F = \frac{4E}{3(1-\nu^2)} R^{1/2} \delta^{3/2} \left[ 1 - \frac{2\alpha_0}{\pi} \chi + \frac{4\alpha_0}{\pi^2} \chi^2 - \frac{8}{\pi^3} \left( \alpha_0^3 + \frac{4\pi^2}{15} \beta_0 \right) \chi^3 + \frac{16\alpha_0}{\pi^4} \left( \alpha_0^3 + \frac{3\pi^2}{5} \beta_0 \right) \chi^4 \right], \quad (2.13)$$

Where  $R$  and  $\delta$  are based on Hertzian theory,  $h$  is the sample thickness,

$$\chi = \sqrt{R \delta / h}, \text{ and constant } \alpha_0 \text{ and } \beta_0 \text{ are functions of the material Poisson's ratio } \nu.$$

Parameters  $\alpha_0$  and  $\beta_0$  depend on  $\nu$ , and when the sample is bounded or not bounded to the substrate, they are given by

$$\alpha_0 = -0.347 \frac{3-2\nu}{1-\nu}, \quad \beta_0 = 0.056 \frac{5-2\nu}{1-\nu}, \quad (2.14)$$

When the sample is bounded to substrate, they are given by

$$\alpha_0 = -\frac{1.2876-1.4678\nu+1.3442\nu^2}{1-\nu}, \quad \beta_0 = \frac{0.6387-1.0277\nu+1.5164\nu^2}{1-\nu}, \quad (2.15)$$

It is clear that the term outside of the bracket is the Hertzian solution for indentation on semi-infinite surfaces. Inside are the correction factors that account for thickness reduction.

It vanishes as the thickness of the sample becomes larger and approaches semi-infinite space.

This correction is valid for all ranges of force  $F$ , the indenter radius and sample thicknesses. It is also valid for all values of Poisson's ratio. Long recently extended the Dimitriadis approach to appending correction factors to the Hertzian contact model by assuming neo-Hookean hyperelastic effects.

The focus of that study was mechanical characterization of heterogeneous specimens, not the investigation of elasticity variations in a specific biological material [40, 41].

## **2.4 Initial Contact Point Challenge**

The second major challenge involving indentation data that needs to be analyzed based on Hertzian contact theory is that surfaces must be continuous and non-conforming (i.e., initial contact is a point or a line). This challenge arises in cases of indenting compliant sample or samples of hydrated biomaterials. Both are characteristic of our scaffold samples, and this will be discussed in chapter 3.

Therefore, this issue needs to be addressed and reviewed. Equation (2.11 and 2.13) for Hertzian contact and Modified Hertzian contact for thin layer show that both indentation depth  $d$  and applied force  $F$  are zero at the point of initial contact between the prop tip and the sample's free surface. However, the interaction between the surfaces of macroscopic bodies through a third medium is controlled by so-called surface forces. These forces vary in nature based on their strength and based on the distance through which they act [42]. Due to condensation, capillary forces and the meniscus force are known to be present when micro-contact acts as the nuclei of condensation. The presence of these surface forces, meaning attractive forces, result from applying tension force on the indenter tip during tip extension toward the sample surface. This will result in nonzero force (negative), and is usually referred to as pull-on force [43], as shown in Figure 2.4.

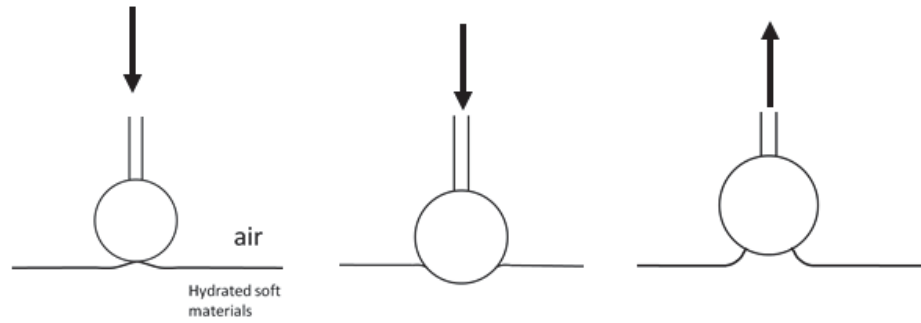


Figure 2.4: illustration of Initial contact point challenges as probe approach soft materials from air, material will jump to probe resulting negative force.

Various data analysis techniques have been used to determine initial contact point. Dimitriadis, et al., used the manual method referred to as visual truncation.

This occurs where the negative part of the force deflection curve is eliminated and the point where indentation force crosses the displacement axis to become the initial contact point with zero displacement and zero load. A more rigorous method of establishing the initial loading point involves the implementing algorithm [36]

Other ways of addressing the initial contact point occurs during indentation, (Deuschle, et al., 2007) [44] describes different methods of obtaining surface findings. The first method involves applying a certain amount of preloading ( $\sim 1\text{N}$ ) for the purpose of identifying the surface, regardless of the degree of stiffness of the specimen being tested. This can cause a considerable degree of indentation in softer materials. The result is that the measured contact depth and area are in error. [45-47, 50] When the contact area is used to calculate the hardness and modulus values, [45-47] incorrect surface detection leads to erroneous results.

In general, it can be assumed that for softer materials the contact area will tend to be underestimated, which leads to an overestimation of modulus and hardness values. This is in agreement with the experimental findings [44, 45, 50].

The second way is an improved method which involves defining a preset load value. The loading starts and displacement values are set to zero. This requires some prior knowledge of the properties of the specimen when choosing a proper preload value. Once the preload value is reached, the loading cycle starts. The load is not set to zero. It remains equal to the preload value for zero displacement. This means that the preload is accounted for as part of the load on the surface, but the corresponding penetration into the surface is neglected, which introduces an error into the calculation of the contact depth and area.

A third method proposed for the purpose of facilitating contact-finding is based on dynamic indentation technique [continuous stiffness measurement (CSM)] which involves the tip of the indenter being oscillated at very low amplitudes while being displaced. Applications of CSM are presented by Guillonneau and colleagues [51].

Ebenstein, et al., (2005) [43] used hydrated indentation to eliminate the ambiguity associated with determining the initial contact point. We used this approach in our indentation. This topic will be discussed in greater details in the following chapter.

## **2.5 Hertzian Contact with Adhesion**

In the previous section we showed how issues related to surface detection and tip-sample adhesion must be eliminated in order to apply Hertzian contact theory. On the other hand, adhesion dominated contact mechanics has been modeled by taking surface energy into account.

In 1971, Johnson-Kendall-Roberts (JKR) [35] extended Hertzian contact theory to include the effect of adhesion. Johnson, et al., suggested that in order to separate bodies which are in intimate contact, mechanical work must be expended in order to overcome the attractive force between the two surfaces.

When two bodies are in contact, the total energy  $U_T$  of the system consists of three terms, the stored elastic energy  $U_E$ , the mechanical energy in the applied load  $U_M$  and the surface energy  $U_S$ . Equilibrium will be established when

$$\frac{dU_T}{da} = 0, \quad (2.16)$$

When no surface forces exist, the contact radius  $a_0$  can be given based on Hertzian Equation 2.8 Elastic energy  $U_E$  may be calculated, considering that  $U_1$  is the energy at load  $P_1$  and contact radius  $a_1$ . When keeping the contact radius at  $a_1$ , and reducing the force to  $P_0$ , the system will have the final state of energy  $U_2$  and the total elastic energy  $U_E = U_1 - U_2$

$$U_E = \frac{1}{K^{2/3} R^{1/3}} \left[ \frac{1}{15} P_1^{5/3} + \frac{1}{3} P_0^2 P_1^{-1/3} \right], \quad (2.17)$$

The mechanical potential energy  $U_M$  of the applied load  $P_0$  is

$$U_M = -P_0 \delta_2$$

$$U_M = -P_0 \left[ \delta_1 - \frac{2(P_1 - P_0)}{3 K a_1} \right]$$

$$U_M = \frac{-P_0}{K^{2/3} R^{1/3}} \left[ \frac{1}{3} P_1^{2/3} + \frac{2}{3} P_0 P_1^{-1/3} \right]$$

Additional details on energy calculation can be found in [35].

The surface energy  $U_s$  is given by  $U_s = -\pi a^2 \gamma$ , where  $\gamma$  is the energy per unit of contact area.

$$U_s = -\gamma \pi \left( \frac{RP_1}{K} \right)^{2/3}$$

Total energy  $U_T = U_E + U_M + U_s$

$$U_T = \frac{1}{K^{2/3} R^{3/5}} \left[ \frac{1}{15} P_1^{5/3} + \frac{1}{3} P_0^2 P_1^{-1/3} \right] + \frac{-P_0}{K^{2/3} R^{1/3}} \left[ \frac{1}{3} P_1^{2/3} + \frac{2}{3} P_0 P_1^{-1/3} \right] - \gamma \pi \left( \frac{RP_1}{K} \right)^{2/3}$$

Equilibrium is ensured when  $\frac{dU_T}{da_1} = 0$ . Or, it can be achieved by  $\frac{dU_T}{dP_1} = 0$ . Therefore, at equilibrium

$$P_1^2 - 2P_1(P_0 + 3\gamma\pi R) + P_0^2 = 0$$

$$P_1 = P_0 + 3\gamma\pi R \mp \sqrt{\{(P_0 + 3\gamma\pi R)^2 - P_0^2\}}$$

In order for equilibrium to be stable, it is necessary to take the positive sign so that

$$P_1 = P_0 + 3\gamma\pi R + \sqrt{\{(6\gamma\pi R P_0 + (3\gamma\pi R)^2)\}}$$

This shows that  $P_1$ , the load acting between two bodies of surface energy  $\gamma$ , is larger than the applied load  $P_0$ . Therefore, the Hertzian contact area, including the surface energy effect, can be expressed as

$$a^3 = \frac{R}{K} \left[ P + 3\pi R \gamma_{12} + (6\pi R \gamma_{12} + (3\pi R \gamma_{12})^2)^{1/2} \right], \quad (2.16)$$

When  $\gamma = 0$ , we return to Hertzian Equation  $a^3 = RP/K$ . At zero, the applied load contact area can be expressed as

$$a_0^3 = 6\gamma\pi R^2/K, \quad (2.17)$$

When the applied load is negative for Equation 2.16, this will give a real solution when

$$6\pi RP\gamma = (3\pi R\gamma)^2$$

$P \geq -3/2\gamma\pi R$  and separation will accrue when

$$P = -\frac{3}{2}\gamma\pi R$$

$$\delta = \frac{a^2}{K} \left[ 1 - \frac{2}{3} \left( \frac{a_0}{a} \right)^{\frac{3}{2}} \right], \quad (2.18)$$

where  $P$  is the external load,  $\gamma_{12}$  is the interfacial energy,  $a_0$  is the contact radius under zero external load,  $\delta$  is the sample deformation,  $R = \frac{R_1 R_2}{R_1 + R_2}$  is the normalized radius of the two spheres with radii of  $R_1$  and  $R_2$ ,  $K = 4/3\pi(k_1 + k_2)$ .  $k_1$  and  $k_2$  are the elastic constants of each sphere, that is  $k_1 = \frac{1-\nu_1^2}{\pi E_1}$  and  $k_2 = \frac{1-\nu_2^2}{\pi E_2}$  where  $\nu, E$  are the Young modulus of each material.

Under a negative load, the spherical tip adheres until the surfaces suddenly comes apart.

Using the retraction curve means that  $E$  can be obtained by solving Equations 2.16, 2.17 and 2.18.

First,  $a_0$  and  $a_1$  can be solved from Equation 2.18 because  $\delta_0$  and  $\delta_1$  are known forms of the force displacement plot. In addition, combining Equation 2.16 and 2.17

$$a_1 = \frac{R}{K} \left[ P_1 + \frac{a_0^3 K}{2R} + \left( \frac{P_1 a_0^3 K}{R} + \left( \frac{a_0^3 K}{2R} \right)^2 \right)^{\frac{1}{2}} \right], \quad (2.20)$$

Allows us to obtain  $K$

In 2004, Sun, et al., introduced a new method for estimating elastic modulus using adhesive interaction between Atomic Force Microscopy (AFM) in cases where it is difficult to accurately locate the initial contact point. The method is based on adhesive interactions, and it is helpful because it does not require locating the tip-sample contact point when fitting the entire retraction force curve [53].

## **2.6 Summary and Conclusions**

This chapter introduced the Hertzian-contact model as the basis of our indentation. We then discussed the correction factor put forward by Dimitriadis, et al., for the purpose of determining the thickness of our scaffold samples.

We also discussed the challenge of defining the initial contact point in order to apply these theoretical models to indentation data for soft hydrated materials, and how we chose to overcome that problem using hydrated indentation. We presented the JKR contact model as a modified Hertzian-contact theory which correlates the contact area with elastic material properties and the interfacial interaction strength. Adhesive contact means that contacts can be formed during the unloading cycle as well as in the negative loading (pulling) regime. As regards Hertzian theory, the JKR solution is also restricted to elastic sphere contacts. We present the JKR contact model as a modified Hertzian-contact theory that includes the influences of adhesion energy. We intend to use that as a further validation of the hydrated indentation method we used.

## **CHAPTER 3: INDENTATION TECHNIQUES FOR MEASURING ELASTIC MODULUS IN SMALL SAMPLES OF SOFT ELASTIC HYDROGELS – *SAMPLE SYSTEM CONCEPT***

### **3.1 Introduction**

Another approach to generate a 3D microenvironment for cells is to encapsulate them within a hydrogel. Gelatin hydrogel is one of many materials can be used for that purpose [6]. Changing gelatin to water mass concentration ratio can be easily incorporated into making soft hydrogels and can cause drastic changes in mechanical properties, stiffness is roughly proportional to the square of gelatin concentration.

In this chapter we use soft gelatin hydrogel to explore practical application for macro-indentation methods that probe mechanical properties on the scale of a millimeter, which is an area influenced by tens to hundreds of cells embedded within the collagen matrix. We focus our study to low stiffness ranges between 600 Pa to 12,000 Pa to address potential challengers arise when indenting low stiffness materials in order to pave the path for using indentation as a reliable mean for measuring elastic modulus for CG scaffolds.

When adapting traditional indentation with compliant samples several issues become critical such as surface detection, tip –sample adhesion and fluid interaction, hence in this chapter we introduce the experimental details we considered during our indentation testing for both materials and methods.

We compared quasi-static indentation (w and w/o surface adhesion) with shear-wave imaging methods for estimating the elastic modulus of soft hydrogels. Assuming a Voigt model for the viscoelastic gel, we show measurement techniques gave equivalent modulus estimates when the sample dimensions exceeded 10 times the indenter radius [37], we also show how each estimation method uniquely biases modulus estimates as it couples to the sample geometry and boundaries. This chapter will address our effort toward developing an indentation method for estimating the elastic modulus in 3-D cell cultures and engineered tissue scaffolds that is consistent with measurements made using elasticity imaging.

### **3.2 Gelatin**

Gelatin hydrogels are denatured collagen molecules that form large, overlapping, isotropic molecular aggregates that strongly adsorb water. Gel sample stiffness is roughly proportional to the square of gelatin concentration and gelatin deforms up to 10% as a linear-viscoelastic material [23] consistent with the Voigt mechanical model under both measurement conditions. Consistency with the Voigt model means that the elastic modulus of gelatin is constant with load frequency and thus quasi-static and dynamic measurements should be equal in the linear regime. Elastic-modulus estimates for gelatin hydrogels at different sample sizes and different mass concentration are made using a quasi-static (<1 Hz) macro-indentation method. Results are compared with a dynamic shear-wave imaging method where the material is mechanically stimulated at harmonic frequencies between 50-200 Hz.

### *3.2.1 Gelatin Sample Preparation*

Gelatin hydrogel samples are made by mixing 250-bloom, Type-B, animal-hide gelatin powder (Rousselot Inc. Dubuque, IA) into deionized water. Sample composition and manufacturing procedures are precisely maintained to ensure reproducible mechanical properties.

Gelatin powder was added to water at  $21^{\circ}\pm 1^{\circ}\text{C}$  in a glass beaker, mixed thoroughly, and placed in a heated water bath at  $70^{\circ}\pm 2^{\circ}\text{C}$  for 45 minutes. The mixture is gently stirred with a spoon for 1 minute after every 10 minutes of heating. The molten gelatin, now visibly clear of undissolved powder and air bubbles, is removed from the heat and allowed to cool at room temperature from  $70^{\circ}\text{C}$  to  $45^{\circ}\text{C}$  before being poured into one of three different-size cylindrical containers described below. After pouring, samples are covered with plastic wrap as they quiescently congealed for  $24\pm 2$  hours. Congealing time begins when molten gelatin is poured into a container and ends at the time of mechanical testing. Three to six identical gel samples were made for each data point reported. Three sample sizes each at four different mass concentrations of gelatin powder were studied: 2%, 4%, 6%, and 8% gelatin. At the time of measurement, the plastic wrap was removed from the sample and mechanical measurements were made at  $23^{\circ}\text{C}$  within the rigid container that surrounded all surfaces except the top surface.

### *3.2.2 Gelatin Sample Sizes*

It is well known that close proximity of boundaries to an indentation measurement site can bias elastic modulus estimates. Therefore three gelatin hydrogel samples with different sizes, illustrated in Figure 3.1, each at four different mass concentrations of gelatin powder were studied: 2%, 4%, 6%, and 8% gelatin.

Cylindrical sample sizes are labeled small, medium, and large based on the diameter ( $D$ ) and height ( $H$ ) of the gel within. Values given in Table I are also compared with the radius of the spherical indenter ( $R = 2.5$  mm). The small sample size is similar to standard well-plate geometries, while the large sample size approached the semi-infinite geometry for both measurement techniques. A very good approximation to the semi-infinite geometry was obtained when  $D/R, H/R > 10$ , as predicted by others [11].

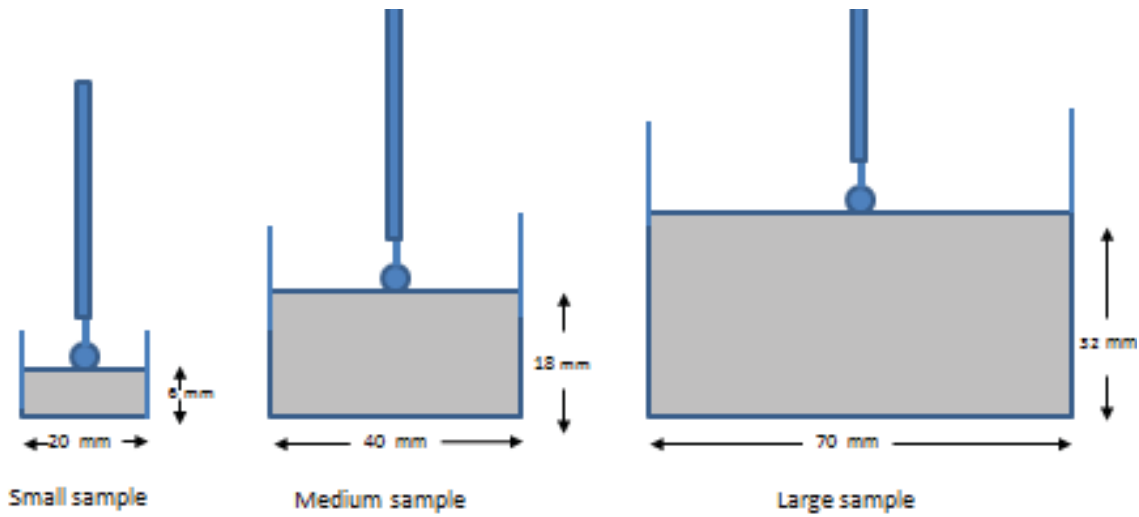


Figure 3.1: Three different sample sizes are considered for both indentation and shear wave.

Size	Small	Medium	Large
$D$ (mm)	20	40	70
$H$ (mm)	6	18	32
$D/R$	8	16	28
$H/R$	2.4	7.2	12.6

Table 3.1: Sample sizes.

The biggest challenge to defining sample height was accounting for the concave meniscus that formed at the exposed top sample surface. The sample heights listed are the minimum thickness of a sample. The meniscus was a larger factor for small samples than large samples, but it appeared the same for all samples of a fixed size. A very good approximation to the semi-infinite geometry was obtained when  $D/R, H/R > 10$ , as predicted by others [26]. Finite-element simulations (described in coming section) were conducted to establish that indentation of large samples produced stress fields that did not interact with the boundaries.

### **3.3 Indentation Experiments**

We applied two different quasi-static indentation tests to each sample. In tests where the indentation probe adhered to the sample, the contact surface was exposed to air. Note that gelatin was a major component of wood glue until recently, so its surfaces are sticky. Whenever adhesions influenced the indentation force-displacement curve, the JKR method (described in details in chapter 2) was applied to estimate moduli.

In tests where adhesions were minimized, the top sample surface was covered with a layer of water and the indentation probe tip was lubricated (Pol-Ease2300, Polytek Development Corp. Easton, PA). These data were reduced using the Hertzian method for elastic modulus estimation.

#### *3.3.1 Indentation Device*

All indentation experiments were performed using the TA.XTplus Texture Analyzer, Figure 3.2, (Stable Micro Systems Ltd., Surrey, U.K.) with a 1-kg load cell (15.3 mg force resolution) and a 5 mm diameter stainless steel indenter tip (1  $\mu\text{m}$  positioning resolution).

Indenter speed was set to 0.01 mm/s to implement quasi-static compressions that minimized weak porous and viscous effects. The visual onset and cessation of sample contact corresponded with features of the force-displacement curve as described below.

Initial contact was used to measure the height of a sample. Furthermore, the shaft of the indenter probe was machined down to 1.5 mm diameter to reduce force bias from water meniscus on the shaft during submerged indentation.



Figure 3.2: TA.XT plus Texture Analyzer used for all indentation experiments.

### *3.3.2 Indentation with Sample Adhesion*

In chapter 2 we described the theory behind JKR model and how it is adequate to address indentation when adhesion is presents.

Here we will discuss the experimental details and the method was followed to calculate the elastic modulus when adhesion is present.

Figure 3.3 is an example of a force  $P$  versus displacement  $\delta$  curve measured for spherical indentation with sample adhesions.

It indicates the probe path from initial contact at  $(\delta_{contact}, P_{contact})$ , 0.45 mm of compressive-load indentation, followed by unloading and separation from the surface. The sample surface was drawn upward at first contact, producing a small negative force.

The hysteresis of the unload cycle is due almost entirely to surface adhesions that cause a substantial tensile force just before the probe separates from the surface.

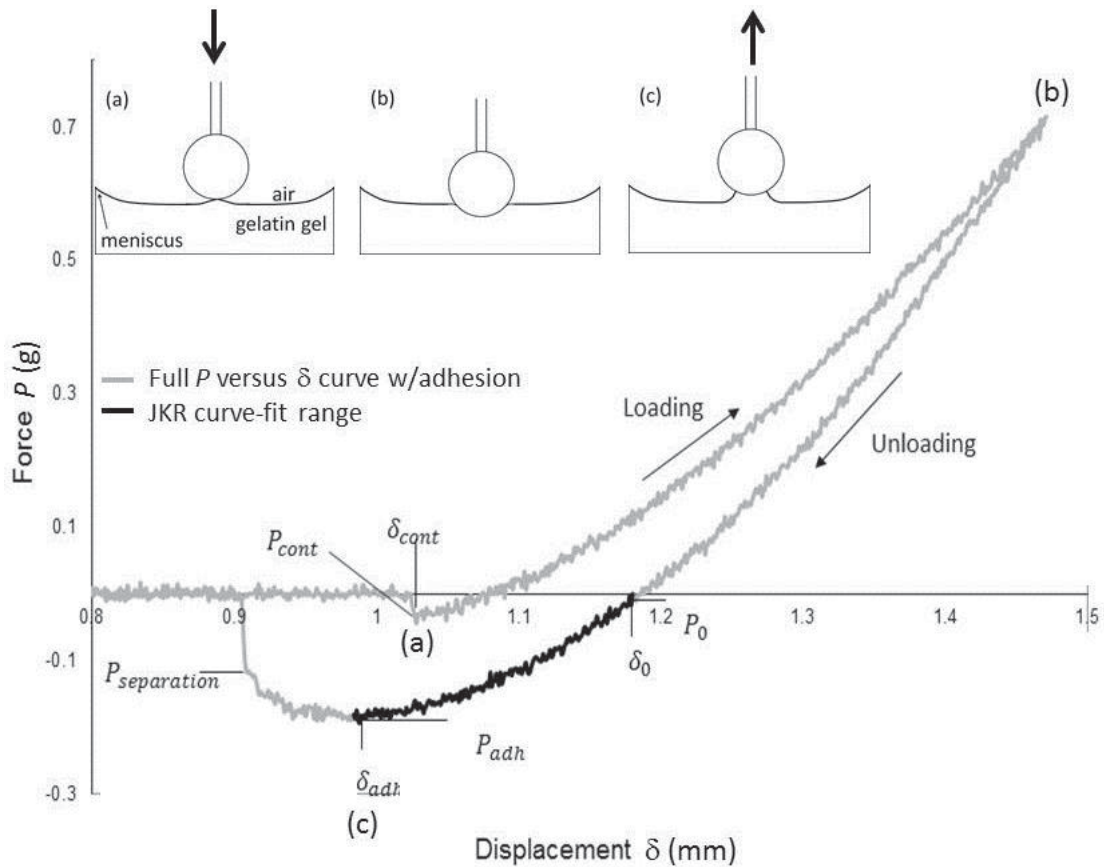


Figure 3.3: Full loading and unload portions of a force-displacement curve (gray line) when there are indenter-sample adhesions. The sample is 8% gelatin. Time-varying force  $P(t)$  is plotted as a function of displacement  $\delta(t)$ . The inserts diagram the experiments at three time points: (a) at initial contact, (b) at the deepest part of the indentation, and (c) just before the adhesion releases.

Arrows indicate direction of the applied force. Significant points for JKR theory are labeled. The solid black line segment is the section of curve fit to the JKR equation based on Sun et al work in 2004.

As mentioned in previous chapter Sun et al, in 2004 introduced a new method estimating elastic modulus using adhesive interaction between Atomic Force Microscopy (AFM) for the case where it is difficult to accurately locate the initial contact point. The method is based on adhesive Interactions and it is helpful because it does not require locating the tip-sample contact point when fitting the whole retraction force curve [53]. To assist the introduction of their approach, Sun et al. first briefly review some of the main conclusions of the JKR theory we introduced in chapter 2. Starting with Equation 2.16 where contact radius  $a$  of two elastic spheres with adhesion and elastic force can be written as

$$a^3 = \frac{R}{K} [P + 3\pi R\gamma + (6\pi R\gamma + (3\pi R\gamma)^2)^{\frac{1}{2}}], \quad (3.1)$$

$$a_0^3 = 6\gamma\pi R^2 / K, \quad (3.2)$$

$$\delta = \frac{a^2}{K} \left[ 1 - \frac{2}{3} \left( \frac{a_0}{a} \right)^{\frac{3}{2}} \right], \quad (3.3)$$

where  $P$  is the external load,  $\gamma$  is the surface energy,  $a_0$  is the contact radius under zero external load,  $\delta$  is the sample deformation,  $R = \frac{R_1 R_2}{R_1 + R_2}$  is the normalized radius of the two spheres with radii of  $R_1$  and  $R_2$ ,  $K = 4/3\pi(k_1 + k_2)$ .  $k_1$  and  $k_2$  are the elastic constants of each sphere, that is  $k_1 = \frac{1-\nu_1^2}{\pi E_1}$  and  $k_2 = \frac{1-\nu_2^2}{\pi E_2}$  where  $\nu, E$  are the Young modulus of each material.

Under negative load the spherical tip adheres until the surfaces suddenly come a part.

From the retraction curve part between point b and point c (highlighted in black)  $E$  can be obtained by solving (Equations. 3.1, 3.2 and 3.3)

First  $a_0$  and  $a_{adh}$  can be solved from Equ 3.1 because  $\delta_0$  and  $\delta_{adh}$  are known from the force displacement plot. Also from combining Equations 3.1 and 3.2

$$a_{adh} = \frac{R}{K} \left[ P_{adh} + \frac{a_0^3 K}{2R} + \left( \frac{P_{adh} a_0^3 K}{R} + \left( \frac{a_0^3 K}{2R} \right)^2 \right)^{\frac{1}{2}} \right], \quad (3.4)$$

From which we can obtain  $K$ .

Similarly Ebenstein et al. [43, 49, 50], used JKR theory to find the elastic modulus from the unload phase of the curve using the equation

$$\delta - \delta_{contact} = \frac{a_0^2}{R} \left( \frac{1 + \sqrt{1 - \frac{P}{P_{adh}}}}{2} \right)^{\frac{4}{3}} - 2/3 \frac{a_0^2}{R} \left( \frac{1 + \sqrt{1 - \frac{P}{P_{adh}}}}{2} \right)^{\frac{1}{3}}$$

Where  $a_0$  [50] is the contact radius between the spherical probe and the sample at point  $(\delta_0, P_0)$  (see Fig. 3), and  $P_{adh}$  is the load at the point of maximum adhesive force. Experimental constants  $a_0$  and  $P_{adh}$  are obtained by fitting the measured force-displacement data during the unload phase at points between  $(\delta_0, P_0)$  and  $(\delta_{adh}, P_{adh})$ .

Once  $a_0$  and  $P_{adh}$  are found using curve fitting using MATLAB and elastic modulus was calculated based on

$$E = \frac{(1-\nu^2)(-3RP_{adh})}{a_0^3}, \quad (3.5)$$

where  $\nu \cong 0.5$  is Poisson's ratio for incompressible gelatin,  $R$  is the indenter radius.

### 3.3.3 Indentation without Sample Adhesion

The same samples used in the indentation experiments described above were tested without the effects of indenter-sample adhesions. Adhesive forces were minimized by adding a layer of water to the gel sample and coating the probe surface with a polymer mold release (Pol-Ease2300, Polytek Development Corp. Easton, PA). We verified that the water did not significantly swell gelatin samples during these measurements by weighing the 2% and 8% gelatin-concentration samples before water was added to the surface and after the water was removed. Sample weight changed less than 0.1% during the measurement time. Figure 3.4 shows an example of the resulting force-displacement curve, where minimizing adhesions minimized load-unload hysteresis. The loading portion of the curve was numerically fit to the classical Hertzian contact equation 2.16 for an incompressible semi-infinite elastic medium, We used measurements of  $(\delta, P)$  pairs and a power-law to fit to the form  $P = a \delta^b$  to find  $b = 1.5$  and with  $a = 16E\sqrt{R}/3$ . Since  $R$  is known precisely, we were able to estimate  $E$ .

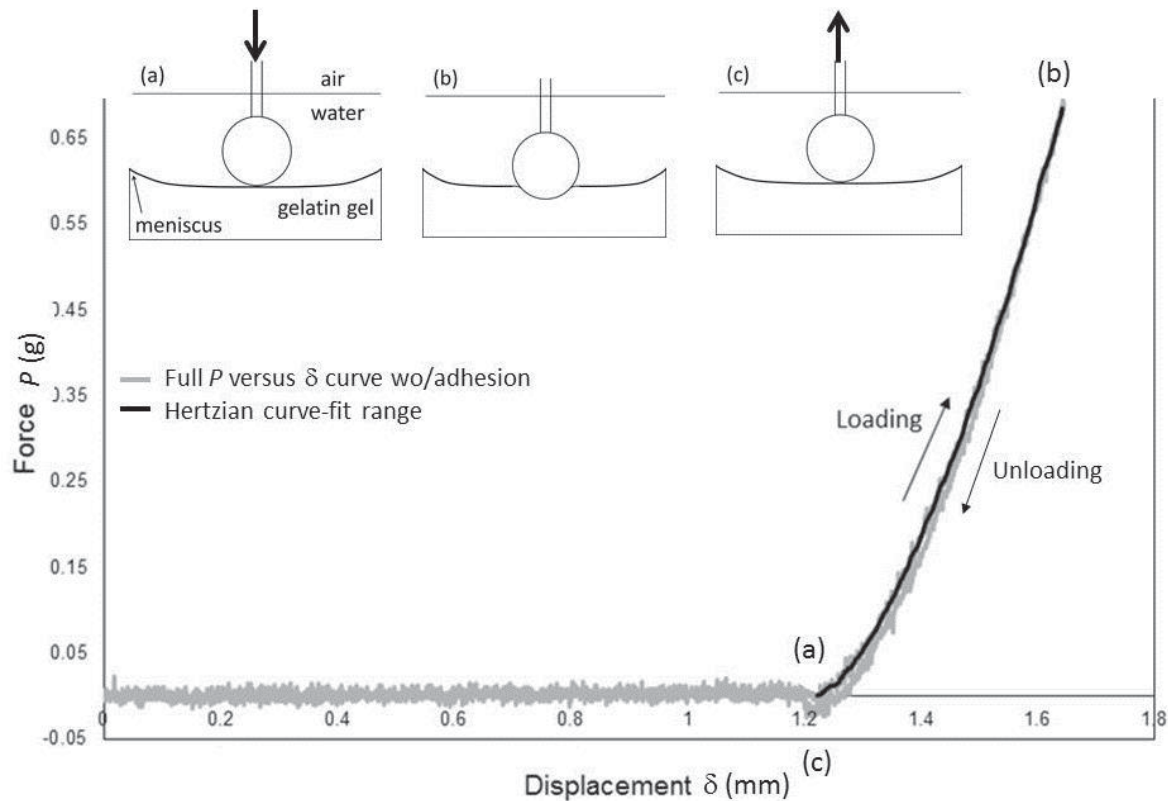


Figure 3.4: The full loading and unloading portions of a force-displacement curve (gray line) when indenter-sample adhesions are eliminated by placing the contact surface under water. The sample is 8% gelatin. The inserts diagram the experiments at three time points: (a) at initial contact, (b) at the deepest part of the indentation, and (c) just as the indenter leaves the sample surface. Arrows indicate direction of the applied force. The solid black line segment is the section of curve fit to the Hertzian equation, Eq. (2.11).

### 3.4 Validation with Shear-wave Imaging

Shear-wave imaging is a popular technique for measuring viscoelastic properties of tissues, in vivo [16, 17]. External forces are applied to induce shear waves that propagate through the medium, while Doppler methods image the shear-wave patterns in tissues. From the images of shear-waves, spatial maps of shear modulus are estimated.

Imaging methods used in this study have been described elsewhere [18, 19]. In medium and large-size samples, ultrasonic methods were used as follows.

Shear waves were excited in the gelatin samples with a needle inserted into the central axis. The needle was vibrated along its long axis at narrow-band frequencies of 50, 100, 150, and 200 Hz to generate radially symmetric shear waves. Unlike the indentation experiments, these gelatin samples contained a sparse concentration of corn starch to provide backscatter for ultrasonic motion tracking. The amplitude of particle displacements in the shear waves was within the linear range of gel deformations [18].

To ensure sample consistency, indentation measurements were made on gelatin samples with and without cornstarch particles. No significant difference was found between measurements on these samples. Detailed information about the experiment, motion detection algorithms, and modulus estimation are found in [18]. Because gelatin is weakly dispersive, homogeneous and incompressible, shear wave velocity  $c_s$  is approximately constant spatially and with needle vibration frequency. Therefore values of  $c_s$  were averaged over samples at four vibration frequencies  $\omega_n$ , and a single value for the dynamic elastic modulus  $E$  was estimated for samples using the equation

$$E = \frac{3\rho}{4} [\sum_{n=1}^4 c_s(\omega_n)]^2, \quad (3.4)$$

Where  $\rho$  is sample mass density: 1.02 at 2% gelatin concentration, 1.04 and 4%, 1.06 at 6% and 1.08 at 8%.

To decrease the estimation errors for shear-wave modulus estimation on small-size gelatin samples (Table I), we used optical-coherence elastography (OCE) methods [20].

A single-element ultrasonic transducer was used to apply a narrow-band acoustic-radiation force

to sample surfaces while a paraxial OCT system scanned the sample from the opposite direction to image shear-wave movements. We showed that ultrasonic and OCT-based estimates of  $c_s$  (and elastic modulus) are equivalent once small differences between surface and bulk shear waves are accounted for.

Small-size gelatin samples were extracted from their rigid molds. They were placed atop a stiff 4% agar-gel pad that coupled samples to the transducer that applied an oscillating force from the bottom surface, through the sample, to oscillate the top sample-air interface. Amplitude-modulated ultrasound pulses generated sinusoidal shear waves at 200 Hz. As the acoustic force was applied, the OCT system scanned the top sample-air surface to image shear waves in the sample at a depth between 1 and 2 mm from the top surface. The large air-sample impedance difference on all surfaces except the bottom provided a strongly reflecting sound-wave impedance difference.

Gelatin gels are elastic materials well represented by the Voigt rheological model. In principle the elastic modulus estimated by indentation should equal the dynamic elastic modulus estimated using shear-wave imaging methods. Nevertheless, each measurement technique can bias modulus estimates differently depending on how that technique couples to the sample boundaries.

Modulus estimates from indentation measurements are biased high when nearby rigid boundaries bonded to the sticky gel increase the deformation resistance. Shear-wave methods are biased when shear waves reflect off boundaries to mix with primary shear waves.

However, shear waves are highly attenuated by the high-water-content gelatin even though the responses to quasi-static indentation are predominantly elastic. So reflections from boundaries in large samples were expected to have a relatively minor effect on modulus estimates.

The geometry of sample boundaries couples uniquely to each measurement. For these reasons, we consider each sample as a combination of the material and its unique boundary as a sample system. We are not reporting intrinsic gelatin properties at each sample size; we are reporting measurements of gel-container systems.

### **3.5 Numerical Simulation**

Finite-element simulations were generated to examine two important aspects of the submerged indentation experiment. First, we hoped to establish the minimum sample size where boundaries do not bias the force-displacement curve, and hence the Hertzian assumption is valid provided adhesions are minimal or accounted for in data reduction. Second, we sought experimental evidence that the layer of water added to the gelatin surface does not bias modulus estimates.

ABAQUS 6.12 finite-element software [68] was employed to simulate the quasi-static experiment of indentation without surface adhesions. A 4-noded, axisymmetric, 2-D element (CAX4RH) was applied to model gelatin samples, where the element size was initially set to 0.0625 mm.

The sample mesh density was increased near the surface that is in contact with a rigid spherical indenter by setting the ABAQUS bias interval parameter to 0.99 as shown in Figure 3.5 a,b. These parameters allowed the model to converge while maintaining a manageable computational

load. The model led to a force-displacement curve that agrees with Hertzian theory for an infinitesimal indentation depth as shown in Figure 3.5 c.

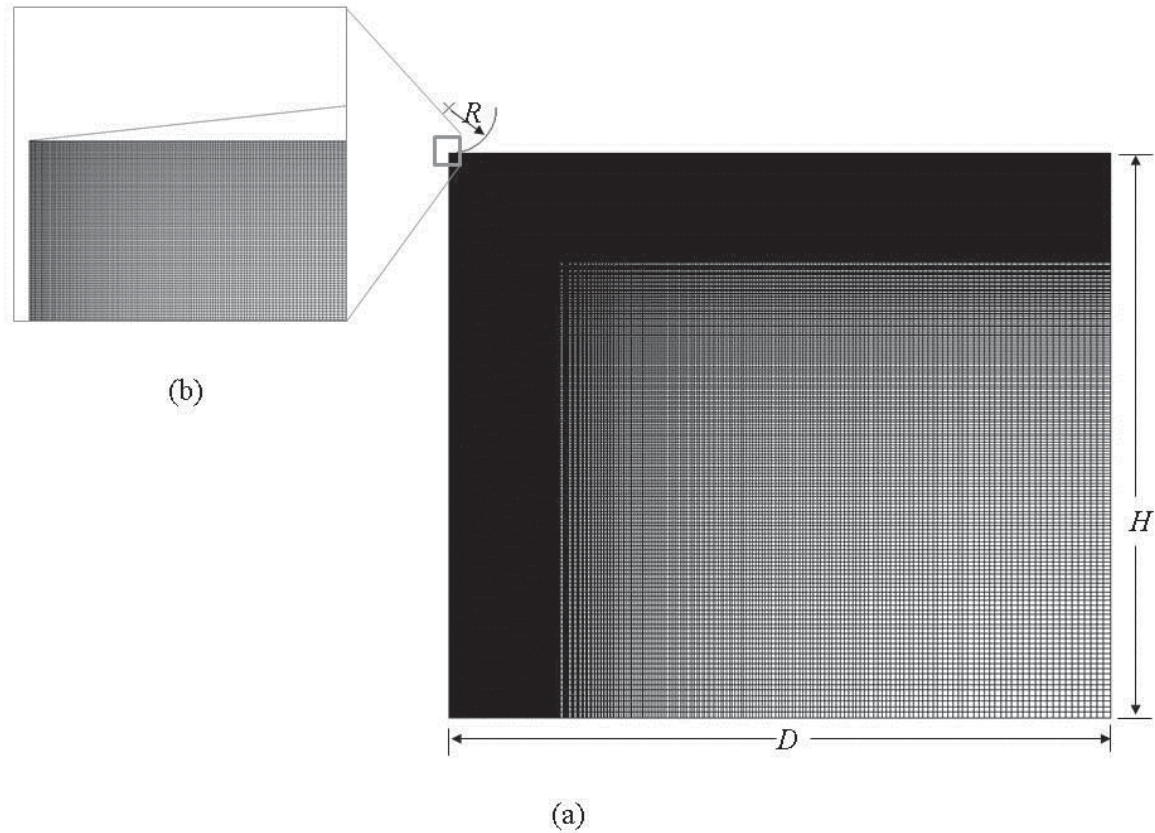
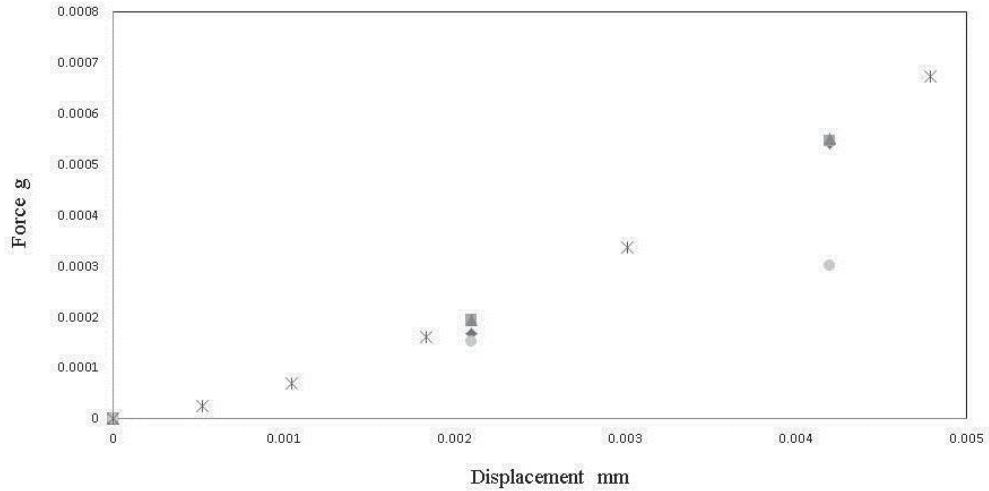


Figure 3.5: (a) Axisymmetric finite-element model for validating indentation without adhesions. Large-size sample with diameter  $D$  is 28 times the size of indenter radius  $R$ . Sample height  $H$  is 12.6 times  $R$ . Both  $D$  and  $H$  are approaching semi-infinite geometry. Black regions (top and left edges) show a very high mesh density under the rigid spherical indenter. This is achieved by setting the mesh bias interval parameter to 0.99 to ensure contact convergence. (b) Zoomed in image under indenter showing fine mesh needed to achieve convergence.



(C)

Figure 3.5 (cont.): (C) Mesh size and contact convergence is achieved by comparing FE force displacement curve to Hertzian force displacement curve at very low indentation depth. Hertz (square symbol) vs. different element sizes in the range 0.25mm, 0.125mm, 0.0625mm to 0.03125mm (circular, diamond, triangle and asterisk, respectively). Convergence is achieved with 0.0625 mm.

The indenter is modeled as a rigid sphere. Frictionless contact is assumed between the indenter and the sample surfaces, and no-slip boundary conditions are applied at all sample surfaces except the top surface. We found that the finite-element simulations of the large-sample indentation experiments closely agreed with those from measurements for indentation without adhesion.

### 3.6 Statistical Analysis

The mean values reported in this paper are averaged from measurements on at least three samples. Error bars indicate one standard deviation. An analysis of variance (ANOVA) method was used to analyze the consistency of measurements made among the different testing

conditions. To compare methods at a single gelatin concentration, one-way ANOVA was applied to test the null hypothesis that all elastic moduli measurements are from the same population. We rejected the null hypothesis from results of Tukey's post hoc test after one-way ANOVA when  $p < 0.05$ .

For comparison of methods at all four gelatin concentrations, two-way ANOVA was applied instead. To compare the effects from different sample geometries on measurements, we used only the measurement results from indentation with adhesion method. We rejected the null hypothesis when  $p < 0.05$ .

## **3.7 Results**

### ***3.7.1 Measurements in Semi-infinite Samples***

Elastic modulus estimates (mean  $\pm$  1 sd,  $N = 3$ ) all made from large-size, 8%-gelatin-concentration samples are presented in Figure 3.6 for the three measurement techniques summarized in the Materials and Methods section. Measurement technique is the only experimental variable.

ANOVA analysis of the data suggests that the three groups cannot be differentiated at the  $p = 0.05$  level of significance.

Agreement among the methods was expected by assuming the elastic modulus is frequency independent and the dimensions of the large sample size are essentially semi-infinite so that boundary interactions do not bias modulus estimates.

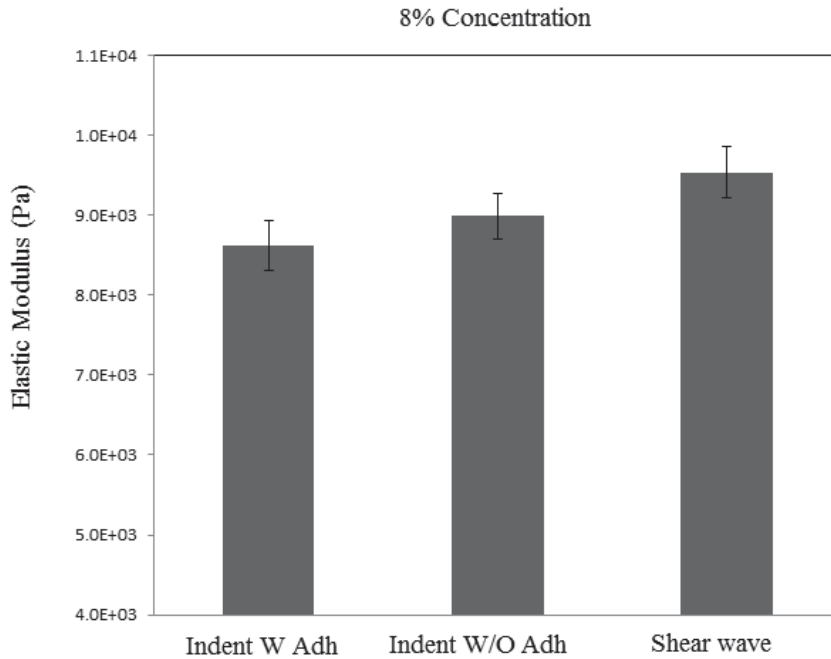


Figure 3.6: Comparing mean elastic modulus measurements for large-size, 8% gelatin-concentration samples for three measurement techniques: indentation with surface adhesion, indentation without adhesion and shear wave imaging. Error bars indicate  $\pm 1$  standard deviation.

In Figure 3.7, the results of Figure 3.6 are expanded to also include samples with lower gelatin concentrations: 6%, 4%, and 2%.

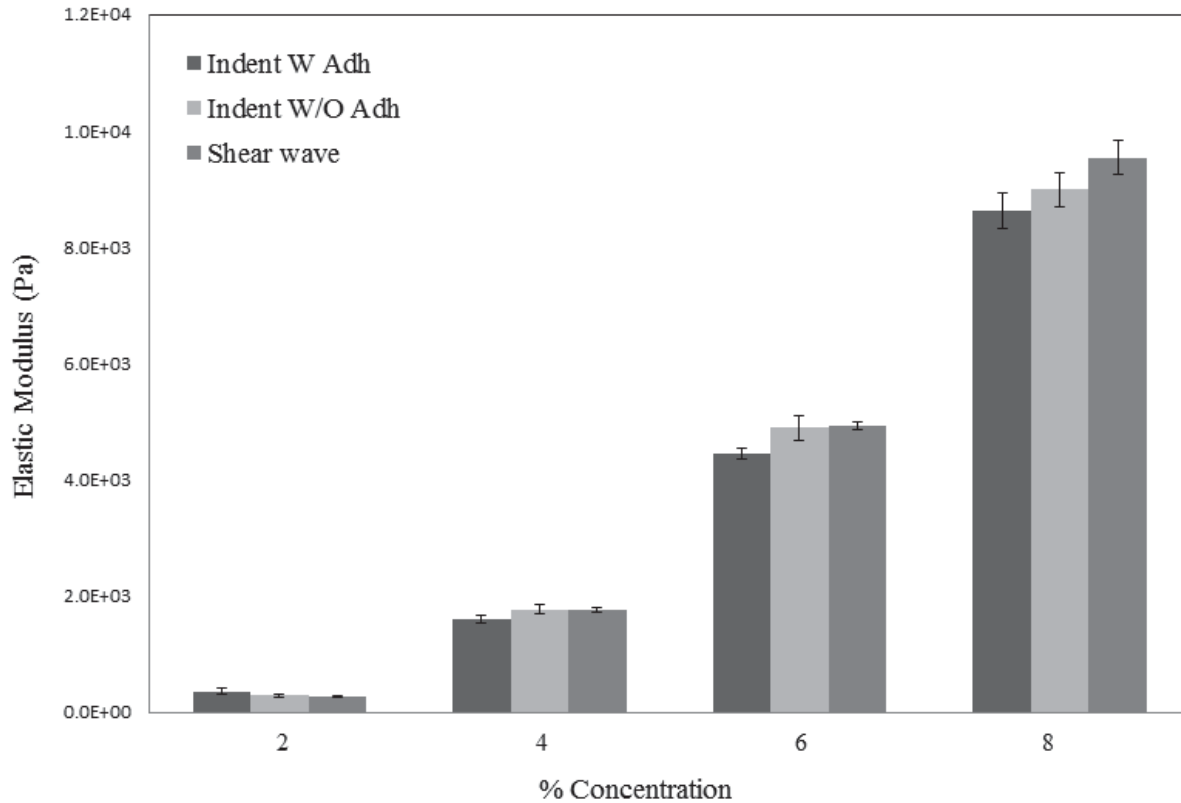


Figure 3.7: Comparing mean elastic modulus measurements for four concentrations of gelatin and the three measurement techniques identified in Fig 6. Error bars indicate  $\pm 1$  standard deviation.

Measurement conditions are otherwise identical. In Figure 3.7, the two experimental variables are measurement technique and gelatin concentration. The three techniques gave statistically equivalent estimates at a fixed gelatin concentration, as determined using two-way ANOVA. The high level of measurement consistency observed suggests that elastic moduli estimated using indentation methods with or without indenter-tip adhesions can predict results from shear-wave imaging techniques in large-size, linear-elastic sample media, where the measurement technique does not sense the boundaries.

We further measured the dependence of  $E$  on gelatin concentration  $C$  by fitting the data in Figure 3.7 to the power law  $E/E_0 = C^n$ , where  $E_0$  and  $n$  are constants. Gilsenan and Ross-Murphy [21] reported that a relative shear modulus that varied with the square of gelatin concentration between 1% and 5%, i.e.,  $G/G_0 = C^2$ . Since  $E \cong 3G$ , the ratio for elastic modulus is the same. Similarly Orescanin et al. [22] reported  $n = 2.7$ . From the data in Figure 6, we find the power-law exponents for the three techniques are in this range and very similar to each other. These results are listed in Table 2.

Method	$n$	$R^2$
Indent W Adhesions	2.29	0.999
Indent WO Adhesions	2.50	0.999
Shear-wave Imaging	2.53	0.998

Table 3.2: Measured exponents  $n$  found by fitting data in Figure 5 from the three measurement techniques to  $E/E_0 = C^n$ .  $R^2$  is the correlation coefficient for the linear fit to  $\ln E/E_0 = n \ln C$ .

### 3.7.2 Measurements of Finite-size Samples

In Figure 3.8, the results of Figure 3.7 are expanded to include variable sample sizes. The experimental conditions are otherwise identical. There are three measurement variables: measurement technique, gelatin concentration, and sample size. Percent deviation in mean modulus estimates relative to the corresponding large-sample results are listed in Table 3.

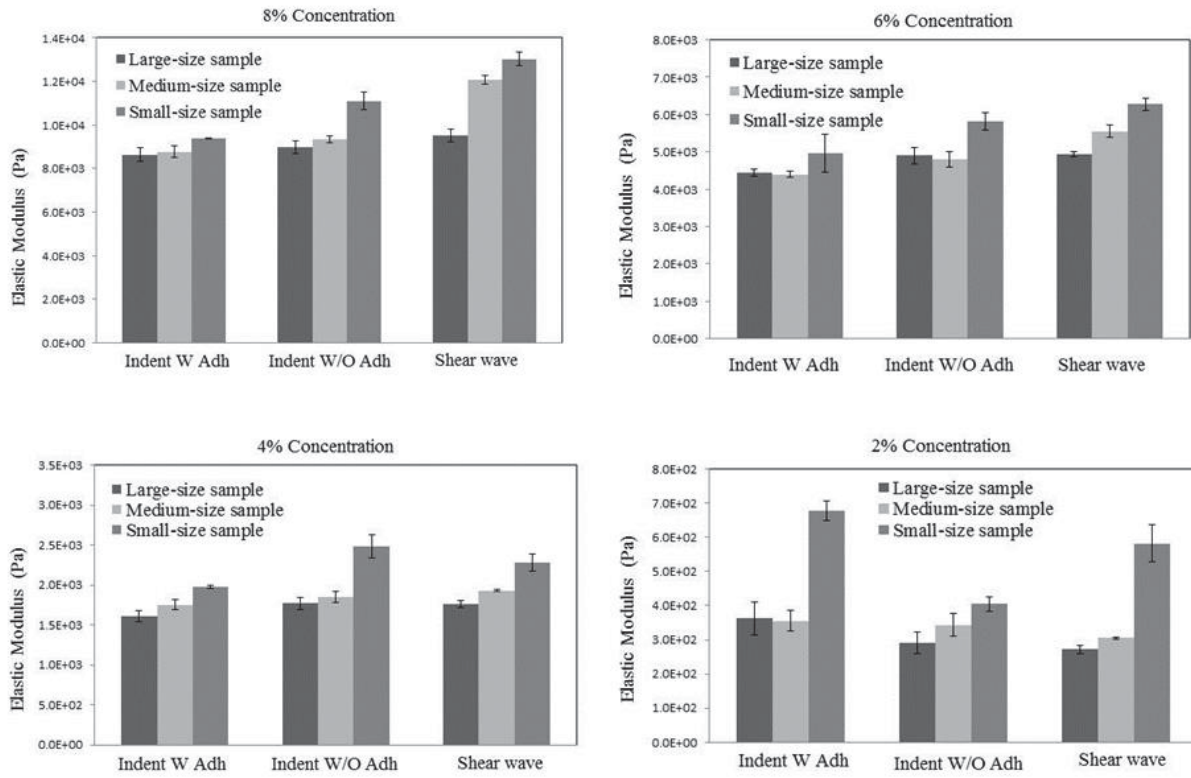


Figure 3.8: Mean moduli for three measurement techniques, four concentrations of gelatin, and three sample sizes (small, medium, and large) as identified in Table 1. Error bars indicate  $\pm 1$  standard deviation.

% Concentration	Small-size			Medium -size		
	Indent W Adh	Indent WO Adh	Shear Wave	Indent W Adh	Indent WO Adh	Shear Wave
2	86%	38%	60%	<5%	17%	5%
4	22%	30%	29%	9%	<5%	9%
6	<5%	18%	27%	<5%	<5%	12%
8	8.3%	23%	40%	<5%	<5%	26%

Table 3.3: The elastic moduli measured for small and medium-size samples  $E_i$  are compared to values measured for the same gelatin concentration and measurement technique made on the large sample size  $E_{\text{large}}$ . The percent difference values in the table indicate  $100 \times (E_i - E_{\text{large}}) / E_{\text{large}}$ , where index  $i$  indicates either a small or medium-size sample. We consider differences less than 5% to be negligible such that boundary conditions do not significantly influence the elastic modulus measurement.

### 3.8 Discussion

Elastic moduli estimated using indentation methods agree with the shear-wave imaging estimates within experimental error for large-size, gelatin samples. Specifically, for the hypothesis that the indentation and shear-wave imaging measurements were from different populations, we could not reject the null hypothesis. Since none of these measurements is considered a calibration standard we cannot claim overall accuracy, and yet statistical equivalence among disparate techniques lends confidence that the measurements are accurate as well as precise.

Furthermore, our application of the JKR technique, which accounts for probe adhesions when reducing force-displacement data to estimate elastic moduli, appears to be effective because these estimates are consistently equivalent with results obtained when the adhesions are

eliminated. The JKR approach avoids the need to identify the time of initial contact for indentation. This approach will be important for studying 3-D cell cultures, which also have sticky surfaces.

The method for eliminating adhesion forces by coating the indenter probe with an oil-based polymer and adding a water layer to the gelatin sample for a few minutes appears to be effective. We know this because measured force-displacement curves are identical to finite-element simulations assuming classic Hertzian contact. Samples submerged more than one hour absorb water, which changes gel properties. This issue is not a concern in 3-D cell cultures since they are naturally saturated in a growth medium fluid.

When the ratio of any sample dimension to the indenter radius falls below 10, the sample has finite size and boundaries influence modulus estimates. The amount of bias (for fixed sample geometry) depends on the material stiffness and measurement technique. Boundary effects are made more complex by the differences in the concave meniscus shape that forms on the top surface at different sample diameters; Figure 3.9 shows how meniscus affects material distribution for low concentration gel, resulting in amplified bottom boundary influence on indentation results.

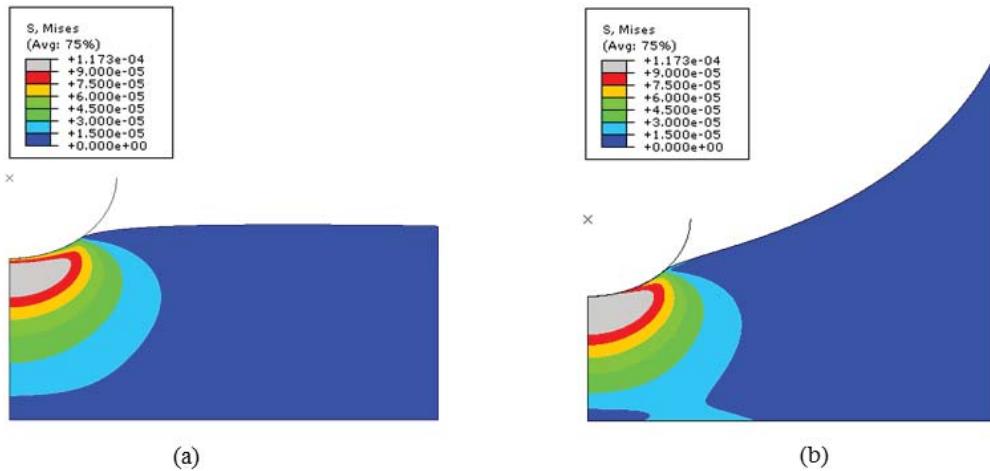


Figure 3.9: (a) Finite-element simulation of stress fields during maximum indentation of 2% gelatin gels for the small sample size without a meniscus. (b) The same simulation was repeated with the meniscus geometry. With the material distribution changing as a result of the meniscus, the bottom boundary has an amplified influence on indentation results.

Our smallest sample (20-mm diameter) appeared to have a flat top surface near the center, but smaller diameter samples, e.g., those from a 48-well culture plate, could pose difficulties not experienced in this study.

As shown in Figure 3.10, the JKR model is prone to sample-size variability when studying the softest materials, where the cube of the contact radius  $a_0^3$  in Eq. (1) varies significantly with sample size. In addition, the softest samples use the least amount of dynamic range on the force sensor, which adds force quantization errors to measurement variability.

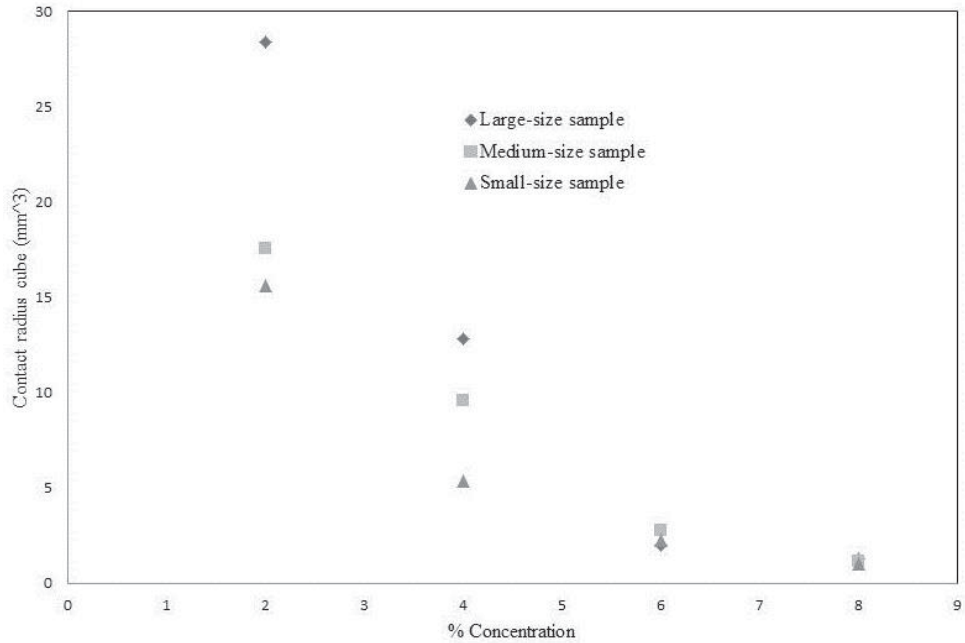


Figure 3.10: Contact radius changes with concentration and sample size.

As shown in the simulations of Figure 3.11, the stress field is most likely to interact with the boundaries in small samples even for small indentations. Hence the most challenging environments for generating bias-free modulus estimates is in small, soft samples where the volume in the meniscus is relatively large. These are the challenging conditions common in 3-D collagen cell culture measurements.

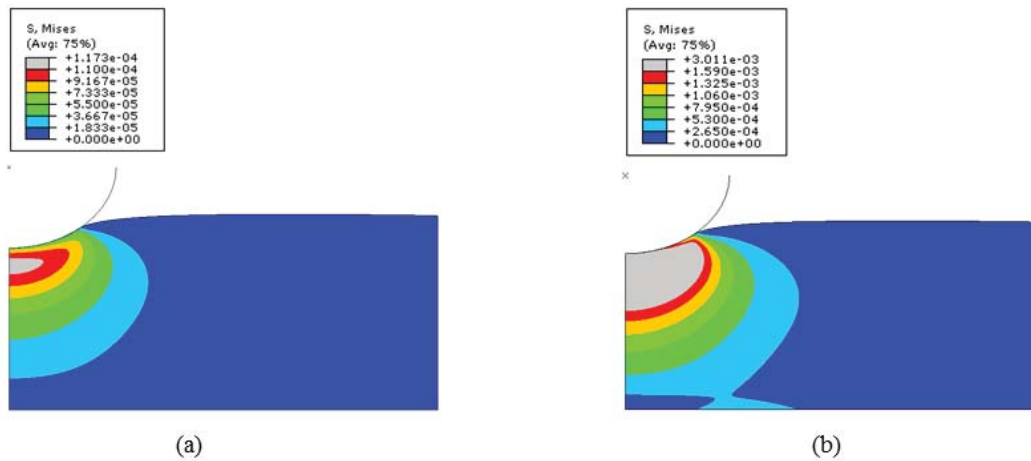


Figure 3.11:(a) Finite-element simulation of stress fields during maximum indentation of 2% gelatin gels for the small sample size without the inclusion of meniscus. (b) The same simulation was repeated for 8% gelatin. Notice that stress extends further in the stiffer 8% gel to interact with the lower rigid boundary.

There is a complicating issue with gelatin gel samples that is not expected to contribute in 3-D cell-culture measurements. The elastic modulus of gelatin (denatured collagen) is highly dependent on its thermal history [27], much more so than what occurs during the polymerization of natural collagen. Since smaller samples lose heat and congeal more quickly than large-size samples, it is possible that the materials at the smaller size really are a little stiffer, so boundary effects do not entirely explain the differences seen in Table 3.

The shear-wave estimation method is mostly affected by wave reflections at boundaries. Hence we see the highest shear-wave attenuations, which are found in the lowest gelatin concentration samples, produce the least bias from boundary effects. For example, this is the trend for medium size samples in Figure 8.

However, shear-wave attenuation is not strong enough to eliminate biasing reflections at the smallest sample size. There is no reason to suspect that differences using of ultrasonic wave tracking versus OCT wave tracking contributes to the data in Figure 3.8.

The next challenge is to repeat the study using viscoelastic polymers saturated in fluids to observe these effects on elastic modulus estimates. Cell-culture samples have moduli on the order of that for 2% gelatin gel samples, 100-500 Pa. Much less is known about the viscous responses of culture media. Indentation methods may need to become dynamic for more complete comparisons with shear-wave imaging methods.

### **3.9 Summary & Conclusions**

We compare hydrated indentation measurements of elastic modulus of gelatin to two other measurement techniques (indentation with surface adhesion and shear wave imaging). We chose gelatin hydrogel because it is linear isotropic for all measurements and because its stiffness can easily controlled by changing the gelatin concentration inside the hydrogel. We showed how each measurement was coupled with material and geometric properties of the gel sample in unique way, therefore we classified the material-geometry combination as a *sample system* so that we can focus on comparing indentation and shear-wave measurement techniques without developing methods to uncouple the measurement from the sample geometry. Finally through consistency of elastic modulus values, we concluded that hydrated indentation with a sterile probe on the spatial scale of 1-5 mm could provide reliable mean to measuring elastic modulus on 3D cell culture and 3D collagen scaffolds once the effects of sample geometry are eliminated from the measurements.

In the next chapter we focus our effort on eliminating the elastic modulus measurement bias imposed by boundary condition so we can get to the intrinsic values of the elastic modulus which is much needed for the controlled spatially gradient stiffness required for manufacturing scaffold needed for TBJ generation.

# **CHAPTER 4: NEW QUANTITATIVE METHOD FOR MEASURING ELASTIC MODULUS AT INTERFACE REGION OF 3D COLLAGEN SCAFFOLDS WITH VARYING STIFFNESS**

## **4.1 Introduction**

3D Collagen Scaffolds with varying degrees of stiffness are great platforms for cultivating spatially-organized tissues such as TBJ. After they are seeded with cells, these newly engineered scaffolds can significantly influence cell behavior and differentiation. Tight control over these scaffolds mechanical properties is essential for their success in development of TBJ. The TBJ stiffness changes by two orders of magnitude from relatively compliant tendon to bone over a relatively narrow interface region. Therefore, accurate elastic modulus measurements of these scaffolds will greatly improve the manufacturing process, and the ability to provide a standardized framework for both in vitro interactions between cells and scaffolds and in vivo tissue engineering studies. This chapter focused on developing a novel method for accurately measuring the elastic modulus of 3D collagen scaffold using indentation. Our work will offer an easy method of precisely quantifying stiffness changes throughout the scaffold, particularly at the interface region.

These scaffolds are manufactured by joining homogeneous mineralized and non-mineralized regions with continuous varying stiffness interfaces [12, 14]. The challenge faced by traditional indentation when measuring these scaffolds is two-fold. The first challenge involves eliminating uncertainties when measuring the elastic modulus of soft materials (the non-mineralized part of

the scaffolds), such as the correct detection of the initial point of contact between the indenter probe and the scaffold surface. In order to address this challenge we will use our previous work which was highlighted in chapter three. The second challenge is to properly resolve the heterogeneity near the interface region. In order to address this challenge we present a novel inverse approach to correct the measurement bias which arises arising out of the heterogeneity of the materials.

We begin by developing a validated FE simulation model from the testing of monolithic scaffolds. The validated FE simulation model will allow us to perform a series of numerical indentations on the two compartment model on both sides of the interface. These indentations will show how measurements are biased due to boundary conditions which arise out of material heterogeneity. We then model the measurement bias using a shift variant filter, which we use to solve the inverse problem in order to obtain the intrinsic elastic modulus of the materials. We also rely on a validated FE indentation model in order to obtain more insight into the effect of probe size on measurement accuracy and will go on to propose a recommended indentation procedure to guide multi-compartment testing.

The FEM validation was established by comparing simulation results with the experimental indentation results performed on series of monolithic scaffolds. We start the chapter by examining the manufacturing process of monolithic scaffolds with five different mineral concentration (0%, 10%, 20%, 30% and 40%). We will then process force displacement curves from hydrated macro-indentation on all of the scaffolds using the Dimitriadis contact model [34].

## 4.2 Monolithic Scaffold Testing

In the absence of samples of multi-compartment scaffolds, indentation tests of monolithic scaffolds with five different mineral concentration (0%, 10%, 20%, 30% and 40%) were used to validate the FE simulation model for the multi-compartment scaffolds.

The five monolithic scaffolds with distinct mineral concentrations were chosen based on prior micro-computed tomography ( $\mu$ CT) analysis performed on two-compartment scaffolds, in which 0% mineral content represented the non-mineralized part and 40% mineral content represented the mineralized one. Figure 4.1 shows mineral gradient across the length of the scaffolds obtained by performing  $\mu$ CT [12]. Stacks of images were compiled to create a high-resolution image representing the full depth of the sample that provided insight concerning the interface zone width. The interface was determined to be where the intensity of the line scan increased by 2 standard deviations ( $\sigma$ ) above and  $1.5 \sigma$  below the baseline measurements for CG and CGCaP compartments, respectively. This distance was then measured to find the interfacial width of 500-800  $\mu\text{m}$  as shown in Figure 4.1[12].

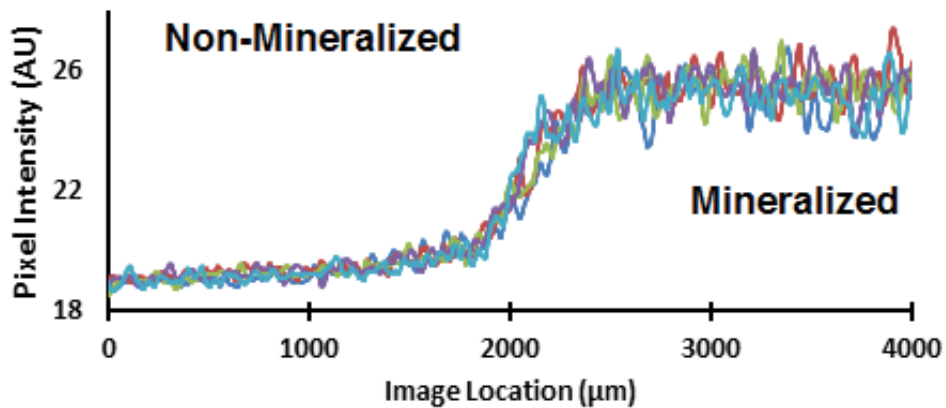


Figure 4.1: Mineral gradient across the length of the collagen scaffolds obtained by performing 2D  $\mu$ CT scan using Xradia MicroXCT- 400 at 25KEV and 5W. Each data point is the average of pixel intensity in XY plan as the sample was scanned along the Z axis. Significant gradient change is shown at the interface of a two-compartment scaffold with 0% minerals on one end

(left-side) and 40% minerals on the other side of the interface (right-side). This image is taken by Professor Harley's laboratory at University Of Illinois [12].

#### *4.2.1 Collagen scaffolds sample preparation*

Collagen scaffolds are prepared in Professor Harley's Laboratory at the University of Illinois [12]. It is a biphasic porous material fabricated using the freeze drying process, sample preparation process is obtained from [12], where 1% mineral scaffolds (CG) were prepared from type I collagen (1.0% w/v) isolated from bovine dermis (Sigma-Aldrich, St. Louis, MO) and chondroitin sulfate (0.1% w/v) derived from shark cartilage in 0.05 M acetic acid. The suspension was homogenized at 4 °C to prevent collagen gelatinization during mixing and was degassed before use [12].

40 % mineral scaffolds (MCG) were prepared from type I collagen (1.93% w/v) isolated from bovine dermis (Sigma-Aldrich, St. Louis, MO) and chondroitin sulfate (0.84% w/v) derived from shark cartilage in 0.1456M phosphoric acid / 0.037M calcium hydroxide buffer solution. The suspension was homogenized at 4 °C to prevent collagen gelatinization during mixing. Calcium salts ( $\text{Ca}(\text{OH})_2$ ) and  $\text{Ca}(\text{NO}_3)_2 \cdot 4\text{H}_2\text{O}$  were added during homogenization and suspension was degassed before use [12].

In order to create monolithic scaffolds with varying degrees of stiffness, we changed the ratio of 1% collagen to 40% minerals described above. In making scaffolds that were 10% minerals, we used 75% of 1% collagen and 25% of 40% mineral. Similarly, for 20% scaffolds we added 50% of 1% collagen with 50% of 40 % mineral, and 25% of 1 % collagen with 75% of 40% mineral were added for 30% scaffold.

All of the scaffold suspensions were then placed in 5x5 inch custom made containers.

The suspension-loaded mold was placed on a freeze-dryer (VirTis, Gardiner, NY) at 20 °C. The sample temperature was then ramped down to -40 °C at a rate of 1 °C/min and held at -40 °C for 1 hour in order to ensure complete freezing. The sample temperature was ramped up to 0 °C at a rate of 1 °C/min while pulling a 200 mTorr vacuum in order to remove ice crystals via sublimation [12, 14, 17]. Afterwards, scaffold samples are cut to the desired sample size using a razor blade and placed in hydrate in 100% ethanol overnight. They were rinsed several times in PBS and were soaked in PBS for 24 hours before crosslinking [12].

#### 4.2.2 *Indentation methods for hydrated collagen scaffold*

Samples for the indentation experiment were cut into a 20x20x5 mm sheet. In plan dimensions were established using FE simulation so that the side boundary is sufficiently distant so that it does not exert any influence on the indentation force deflection curve. The scaffold placed in a petri dish over 3 grams of PDMS (1:5 ratio of the PDMS catalyst to the PDMS monomer), which was uniformly spread into a thin layer. The PDMS was then incubated at 37 degrees for 1 hour and 20 minutes, at which point the scaffold is added.

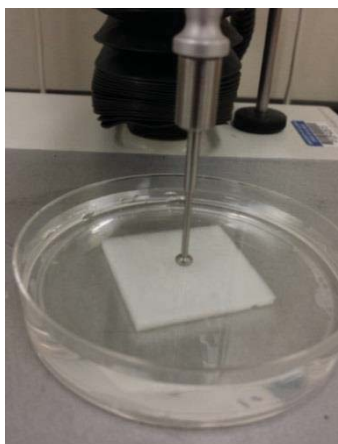


Figure 4.2: 20x20x5 mm collagen scaffold placed in petri dish over 3 grams of PDMS and submerged with PBS.

Samples with all-mineral concentrations (0%, 10%, 20%, 30%, 40%) were tested without the effects of indenter-sample adhesions, using the technique established in chapter 3. Adhesive forces were minimized by adding a layer of PBS to the scaffold samples and coating the probe surface with a polymer mold release (Pol-Ease2300, Polytek Development Corp. Easton, PA). In order to ensure the consistency of the results, each sample was tested at five different locations.

### **4.3 Numerical Simulation of Indentation Using FE**

#### *4.3.1 FE Simulation for monolithic scaffolds model*

The 3D finite-element simulation model was used to address two important aspects of the submerged scaffold indentation. First, it was used to establish the minimum sample size where boundaries exert little to no influence on the force-displacement response. Once that was established, one can use the Dimitriadis model for data reduction. Second, this validated simulation model was used to construct a multi-compartment numerical model to study the material boundary effect on indentation response. ABAQUS 6.13 finite-element software [62] was employed to simulate the quasi-static indentation experiment without surface adhesions. An 8-noded 3-D element (C3D8) was used to model the scaffolds. An analytical rigid surface was used to model the indenter probe with a radius of 2.5 mm. The rigid surface was pushed downward a distance of 0.5 mm in the negative Y direction. Frictionless contact is assumed to be the case between the indenter rigid surface and scaffold surface. Due to symmetry conditions (with respect to the XY plane) half of the sample was discretized, which resulted in a reduction of the model size and run time. Although  $20 \times 10 \times 5 \text{ mm}^3$  would have been sufficient to model the collagen scaffold when considering symmetry conditions, we decided to use a  $40 \times 10 \times 5 \text{ mm}^3$

model because we needed to use the model later in multi-compartment scaffolds simulation. Figure 4.3 shows the finite element model (FEM).

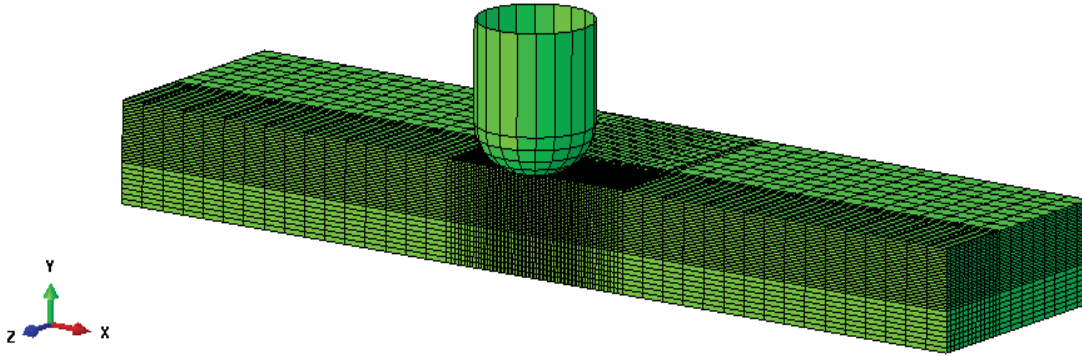


Figure 4.3: 3D image of the half symmetry finite element mesh of collagen scaffold samples. Finer mesh size (0.08 mm) is enforced at the contact region under the rigid indenter.

The element size was initially set to 0.08 mm in the contact area under the rigid spherical indenter. It was gradually increased to a uniform 1.00 mm after reaching a distance of 3 mm from the indenter, along the positive and negative X-axes.

Changing the element size away from the contact area allowed the model to converge faster while maintaining a manageable computational load. A no-slip boundary condition was enforced at the sample bottom surfaces. Figure 4.4 depicts the von-Mises stress pattern under the contact area between the rigid probe and sample top surface.

It shows that the stress pattern is localized under the indenter and across the thickness. This confirms the need to account for the influence of the bottom boundary when estimating the elastic modulus by adapting the Dimitriadis correction. (This issue was addressed in chapter 2).

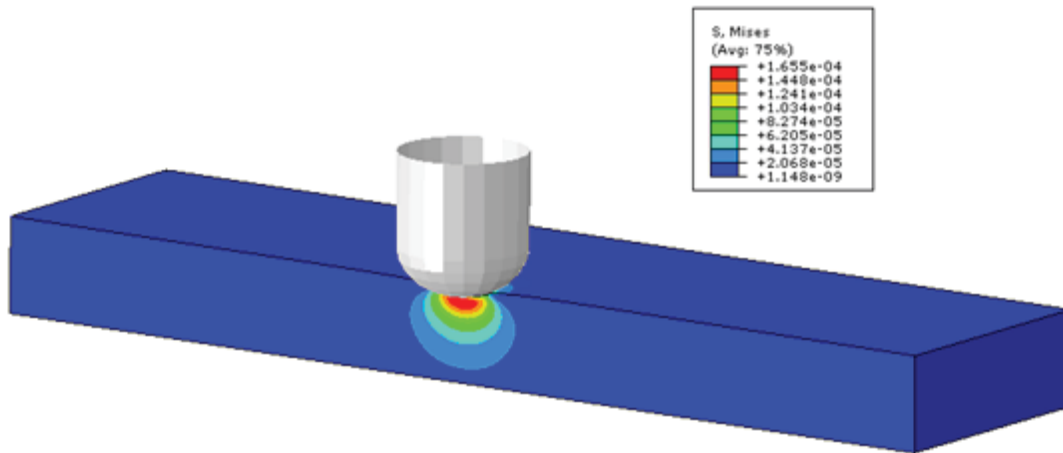


Figure 4.4: 3D image of von-Mises stress plot for 0% monolithic collagen scaffolds- sample under full load of 0.5 mm displacement in the negative Y direction.

#### 4.3.2 FE simulation for multi-compartment thin scaffold

The challenge of measuring the elastic modulus of thin scaffolds is confounded when dealing with two compartments which are heterogeneously joined. Our objective is to provide tissue engineers with an indentation method that can correct for elastic modulus measurement bias at the interface region.

We used the validated FE simulation model (established for the monolithic scaffolds) to investigate the determination of the intrinsic elastic modulus near the interface due to the lack of actual samples with discontinuities at the interface.

The multi-compartment scaffolds FE Model is constructed by assigning two different material properties to each compartment, which generates step change in the elastic modulus at the interface.

Both materials were assigned based on monolithic indentation tests conducted on mineralized and non-mineralized scaffolds independently. Mineralized compartments (40% mineral) are situated to the left of the interface (negative x). Non-mineralized compartments are situated to the right of the interface (positive x). Figure 4.5 shows a von-Mises stress pattern when indenting two compartment scaffolds vs. the homogenous monolithic scaffolds shown in Figure 4.4.

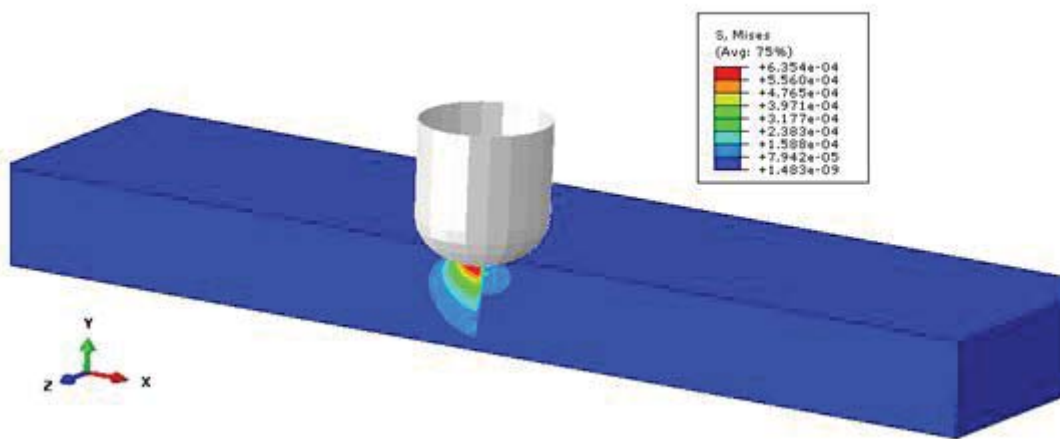


Figure 4.5: 3D image of a von-Mises stress plot for two-compartment collagen scaffolds sample under full load of 0.5 mm displacement in the negative Y direction. 0% minerals on one end (left-side) and 40% minerals on the other side of the interface (right-side).

Two-compartment heterogeneity presents an insurmountable challenge for indentation data interpretation, particularly when using the Hertzian or Dimitriadis correction. Figure 4.7 shows the elastic modulus is determined by series of FE indentations, (one at the interface line and eight indentation points on each side of the interface) as shown schematically in Figure 4.6

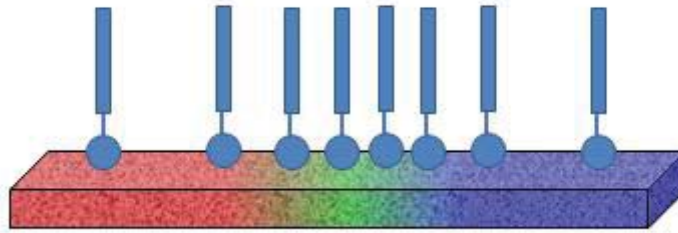


Figure 4.6: Schematic showing series of 17 indentations taken place along scaffold x axes and on both sides of the interface; one at the interface line and eight indentation points on each side of the interface. 0% minerals on one end (left-side) and 40% minerals on the other side of the interface (right-side).

The first five indentation locations were equally spaced, starting at 0.2 mm from the interface. The last three indentation locations were spaced 0.5 mm apart. The elastic modulus values converged to each compartment's unique modulus value found at 2.5 mm on either side of the interface.

Figure 4.5 shows the influence of the boundary condition on estimations of the elastic modulus around the interface region. This is displayed by predicting incorrect values of intrinsic properties. At the interface, the elastic modulus is the average of the left and right elastic moduli.

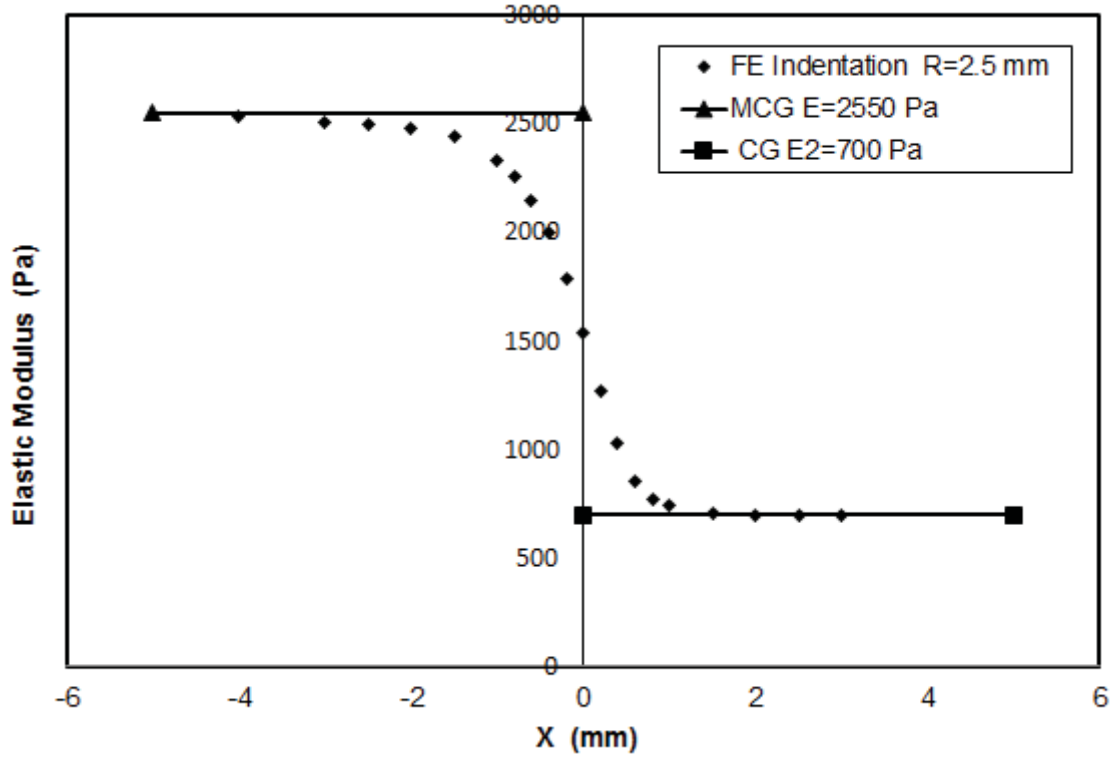


Figure 4.7: Solid black line with square markers and with triangle shaped markers, which represent the two levels of elastic modulus 700 Pa and 2550 Pa associated with non-mineralized and mineralized compartments respectively. Diamond black markers represent elastic modulus values obtained by FE indentation after processing force-displacement with the Dimitriadis contact model.

#### 4.4 New Proposed Method for Correcting Indentation Measurement Bias

In order to correct for the measurement bias shown in figure 4.7, we propose a new approach which is analogous to the linear shift variant system used in signal processing where measurements can be described using the following equation

$$y(x) = \int h(x, x') f(x') dx', \quad (4.1)$$

where  $y(x)$  is a function of space representing the measured elastic modulus at any spatial location  $x$ ,  $f(x)$  which is also a function of space which represents the exact elastic modulus at spatial location  $x$ .

In addition,  $h(x, x')$  is the correction function which maps  $f(x)$  to  $y(x)$  and can reflect blurring and filtering caused by the indentation process as well as the mechanical properties of the scaffolds. Once  $h(x, x')$  is known, it can be used to obtain  $f(x)$  from  $y(x)$  by solving the integral equation the 4.1 for  $f(x)$  (note:  $y(x)$  is determined by carrying out indentation simulation when  $f(x)$  is not known) and therefore assist in determining the intrinsic elastic modulus values in the actual (physical) space  $f(x)$ , as illustrated in figure 4.8.

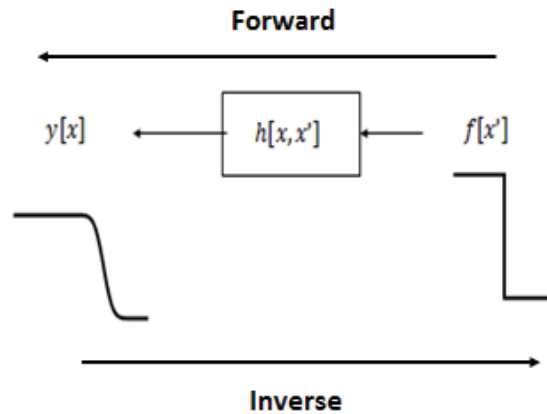


Figure 4.8: Schematic illustrating function  $h$  can be applied to indentation results in order to obtain the intrinsic elastic modulus at the scaffolds interface.

#### 4.4.1 Modeling the forward problem

In order to find  $h(x, x')$  we look at the FE indentation results shown in figure 4.7. The FE results indicate that measurements response is not symmetric with respect to the interface location, which is defined at  $x=0$ . While the elastic modulus values converge toward the intrinsic value, which is approximately 1 mm away from the interface in the non-mineralized (CG) compartment, it is approximately 2 mm away from the interface in the mineralized (MCG) compartment.

Therefore, we chose to model this behavior using the Gaussian shift-variant filter  $h(x, x')$ , where the standard deviation  $\sigma(x)$  is a function of  $x$  and will allow for different stiffness contributions to the elastic modulus based on the location w.r.t the interface.

$$h(x, x') = \frac{1}{\sqrt{2\pi} \sigma(x')} e^{-\frac{(x-x')^2}{2\sigma^2(x)}}, \quad (4.2)$$

In order to estimate  $\sigma$ , we start with simple and known  $f(x)$ , which is the step function defined by the values of the elastic modulus which describe both parts of scaffolds, (known as monolithic indentation). In addition, when we know  $y(x)$ , which is the FE indentation simulation result, and use Equation 4.1 and 4.2, we obtain a set of  $\sigma$  values which we can use to transform  $f(x)$  to  $y(x)$ . Figure 4.9 shows that the  $\sigma$  we derived is a piecewise linear function of  $x$ .

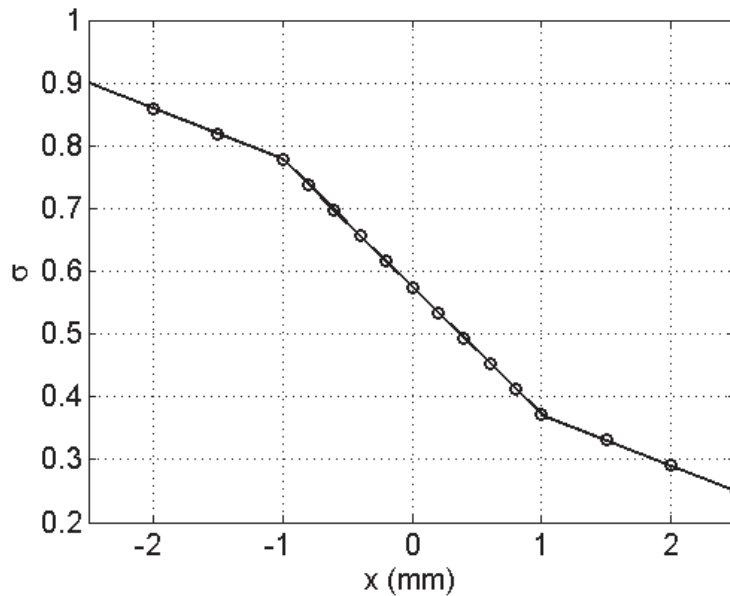


Figure 4.9: Gaussian filter  $\sigma$  values plotted vs. measurement location.

Once the  $\sigma$  values are identified, we can use these  $\sigma$  values to determine  $f(x)$  for any interface once  $y(x)$  is available, assuming that the system represented by Equation 4.1 is linear.

#### 4.4.2 Model verification

Figure 4.10 shows the results for a sharp interface represented by a step function. FE simulation results are compared with the predictions using the shift-variant Gaussian filter model proposed in section 4.1.

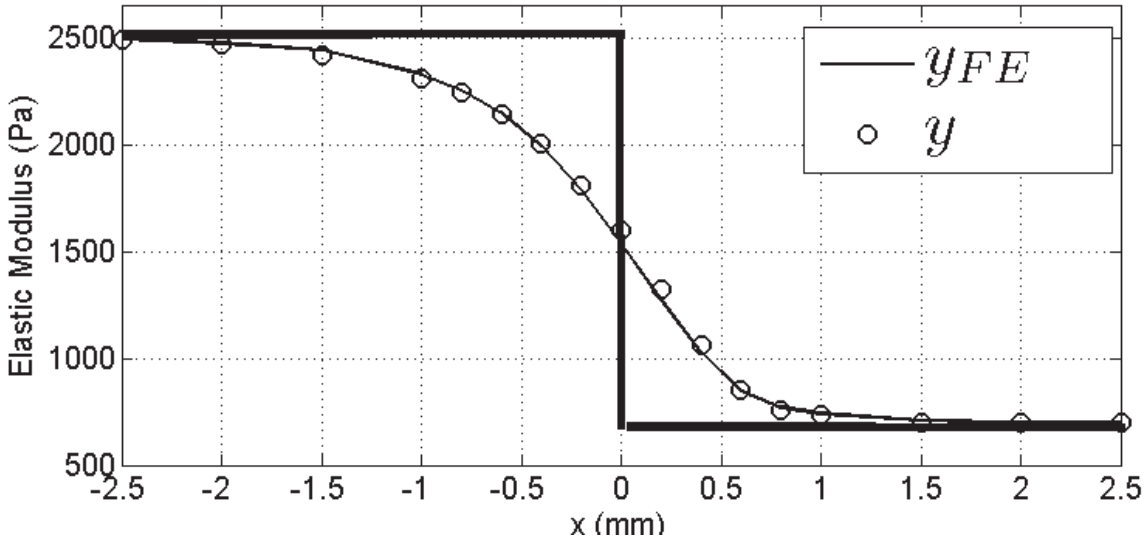


Figure 4.10: The solid thick black line shows a step function representing the two level of stiffness in the two-compartment scaffolds with sharp interfaces, with the thin black line representing the FE simulation results  $y_{FE}$ ,  $y$  is shown with black circle markers which represent Model Verification.

The model prediction matches the FE simulation results closely. Our model consists of defining an adequate correlation filter or function  $h(x, x')$  that we develop by solving the forward problem, i.e., the elastic modulus is known for each of the two adjacent materials.

Although sigma values mathematically are related to the spread between  $f(x)$  and  $y(x)$ , their physical meaning is that they represent the mixture of local material stiffness and the distance from the interface. That is why we see sigma values at the stiffer material side and far away from interface having higher values due the local measurement of stiffer material side being less influenced with the soft material on the other side of the interface.

Figure 4.11 illustrates how Gaussian function change width based on the distance from the interface.

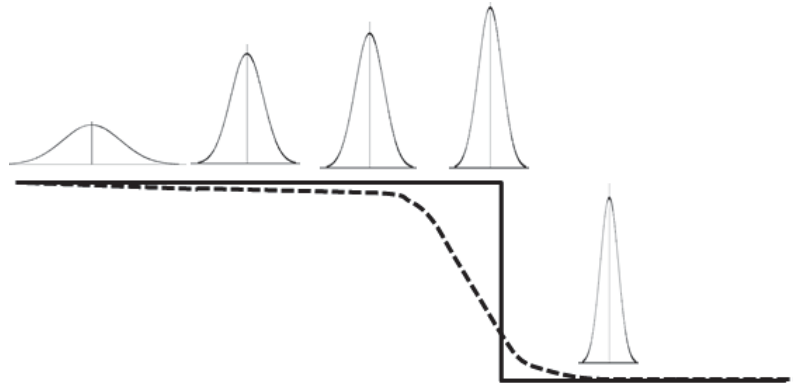


Figure 4.11: Sigma values are reduced in regions very close to the sharp interface, which indicates the local influence of material heterogeneity on the local stiffness. The Solid Black line represents the intrinsic elastic modulus of the two materials and the dashed Black line represents the measured local value of elastic modulus.

These sigma values are sensitive to location (distance away) from the interface and to the stiffness levels represented by the elastic modulus of each material on each of the sides of the interface. To further illustrate this point, we subjected our model to the following test. Let us generate FE data for a larger step where the elastic modulus is 700 Pa on one side of the interface and 7000 Pa on the other side of the interface, rather than the small step previously established at 700 Pa and 2550 Pa. Using the  $\sigma$  values of the small step to transfer  $f$  (Large Step) to  $y$  (Large Step) data. Figure 4.12 shows that  $y$  (Large Step) is not on top of  $y_{FE}$  (Large Step), as it is for the smaller step, which indicate that sigma values are sensitive to local stiffness values within the range.

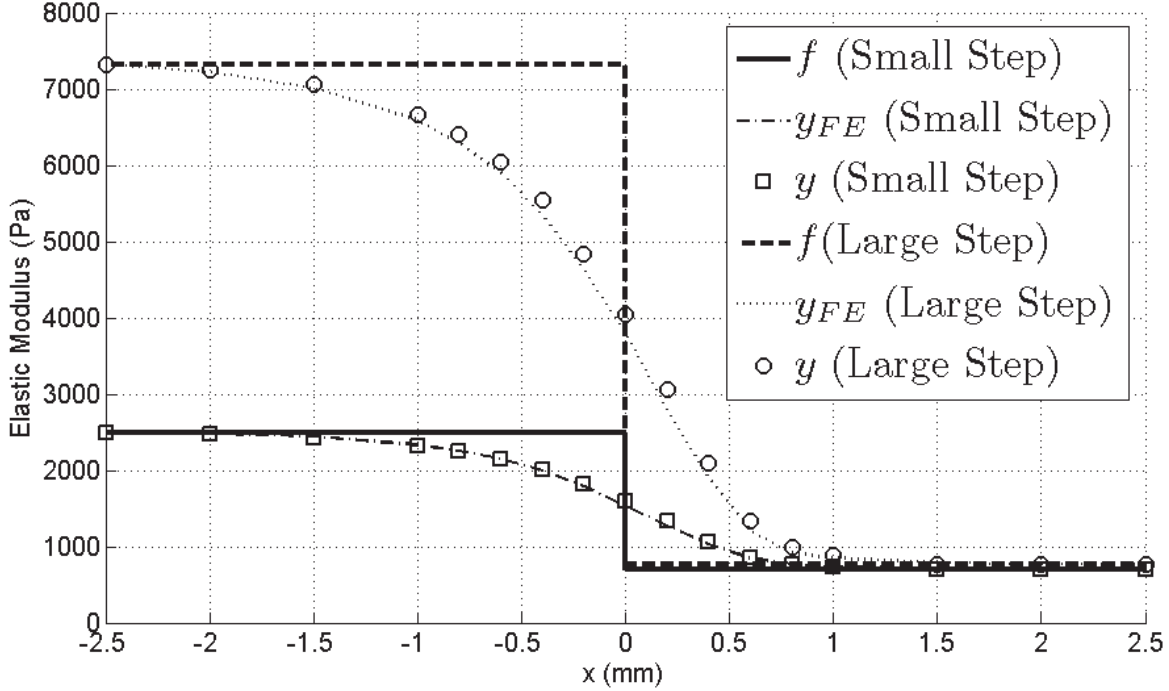


Figure 4.12:  $y$  (Large Step) points, circle markers, are slightly shifted above  $y_{FE}$  (Large Step) when using  $\sigma$  values generated from  $f, y_{FE}$  (Small Step).

#### 4.4.3 Solution to the inverse problem

Figure 4.10 shows that our model consists of defining an adequate correlation filter in the forward problem, i.e., the elastic modulus is known for each of the two adjacent materials. However, our objective is to find the intrinsic elastic modulus of the material around the interface region where measurements are biased. Therefore, we need to find  $f$  by solving the inverse problem  $f = H^{-1}y$ , where  $y = Hf$  is matrix operator notation representing Equation 4.1. Considering that  $H$  is not a square matrix due to a discrepancy in the dimensions between the measurement space (number of indentation locations) and the estimation space, so the inverse solution under the least square error criteria is found using

$$f = (HH^T)^{-1}H^T y, \quad (4.3)$$

Because  $(HH^T)^{-1}$  is ill-conditioned, we used Tikhonof regularization [63] in order to obtain a stable inverse solution  $\hat{f}$

$$\hat{f} = (HH^T + \alpha I)^{-1}H^T y, \quad (4.4)$$

Where  $\alpha$ , the Tikhonof regularization term, was adjusted to find a reasonable trade-off between solution accuracy and stability.

## 4.5 Results

### 4.5.1 Monolithic scaffolds

#### 4.5.1.1 Indentation Measurements for Monolithic Thin Samples

Elastic modulus estimates ( $N = 3$ ) were made using monolithic scaffolds with 0%, 10%, 20%, 30% and 40% mineral concentrations. The mean values reported from the macro indentation were averaged using measurements of at least three samples. Error bars indicate the standard deviations. The results are presented in Figure 4.13, which shows that elastic modulus values increase as the percent of mineral concentrations increase. Each sample was indented at 5 different locations; at the center and at 12, 3, 6 and 9 o'clock locations. Limited data points from the sample with 10% minerals resulted in a smaller error bar.

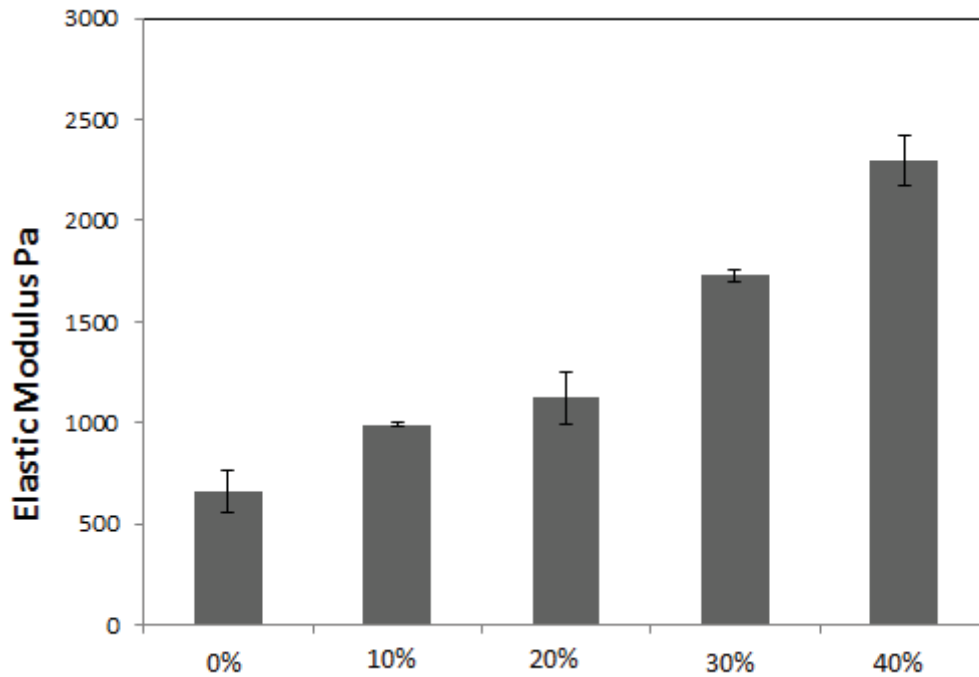


Figure 4.13: Elastic Modulus for CG with different mineralization percentages.

#### 4.5.1.2 Percent mineral characterization via $\mu$ CT

The same scaffolds used in the macro indentation test were also imaged using Micro-computed tomography ( $\mu$ CT). Figure 4.14 shows a cross section-scan of one group consisting of four scaffolds with three different mineral concentrations.

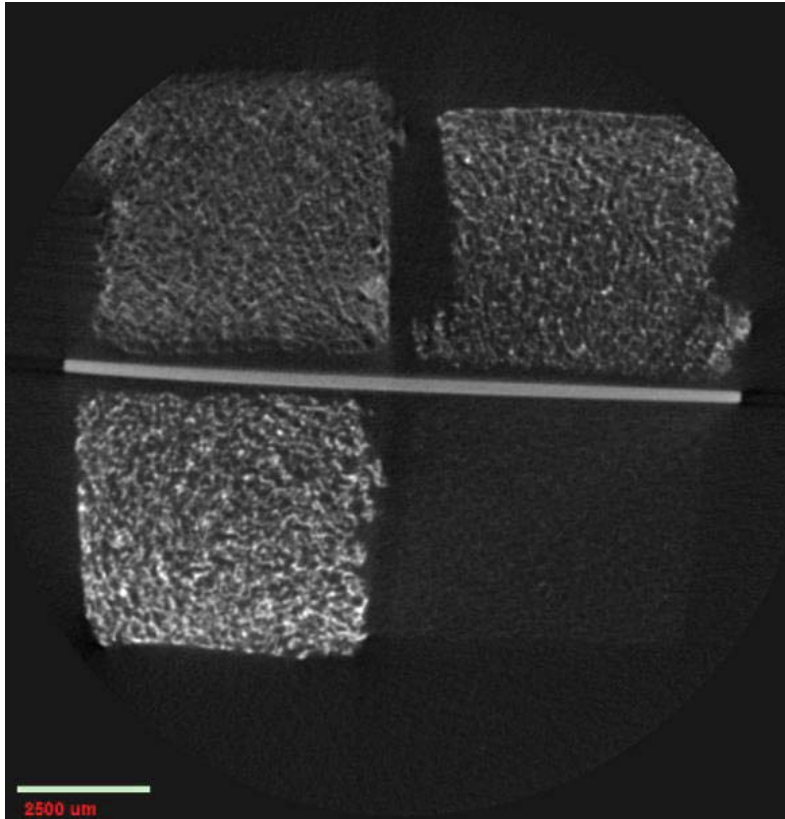


Figure 4.14: image of  $\mu$ CT scan of a cross-section area of 4 scaffolds with 0% mineral concentrations at the bottom right corner and 40% mineral concentrations on the bottom left corner with 20% mineral concentrations for the scaffold on the top.

The image contrast is clear. After reading the image to MATLAB, we took average pixel intensity inside the square window positioned at the center of each scaffold image. We were then able to link image intensity to the percent of mineral concentration, as shown in figure 4.15. Plot shows that pixel intensity increases in a linear manner with mineral concentration, as expected.

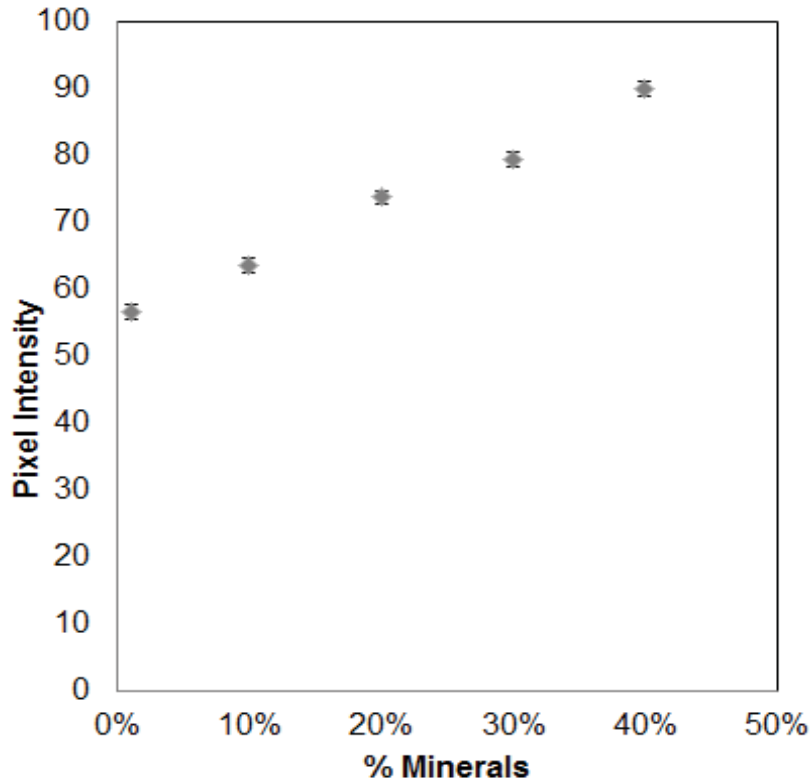


Figure 4.15: Mineral concentrations vs. pixel intensity obtained by processing  $\mu$ CT images using MATLAB.

#### 4.5.1.3 FE simulation for monolithic thin scaffold

Each numerical indentation led to a force-displacement curve that agrees with the Dimitriadis contact model for an infinitesimal indentation depth (0.2-0.3 mm). Figure 4.16 shows three force displacement curves: the test curve is shown in solid gray, the FE curve is shown using gray circle markers, and the solid black curve is the theoretical contact model used to estimate elastic modulus based on Dimitriadis [34], (as described in detail in chapter 2). Several numerical iterations were needed for the FE model in order to achieve good validation for both the theoretical and test results.

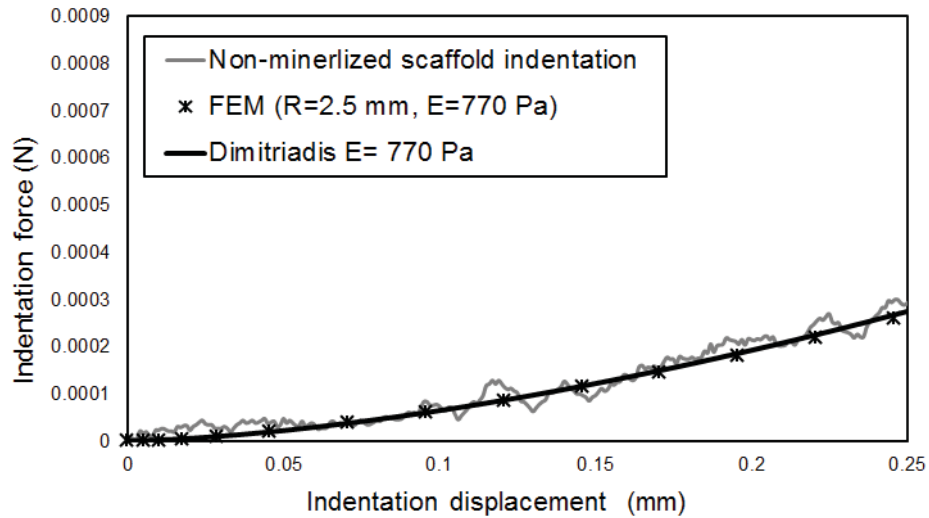


Figure 4.16: Force displacement indentation curves for 0% minerals; gray line is for the hydrated indentation test, black asterisk markers are for the Dimitriadis model and solid black is for the FE simulation.

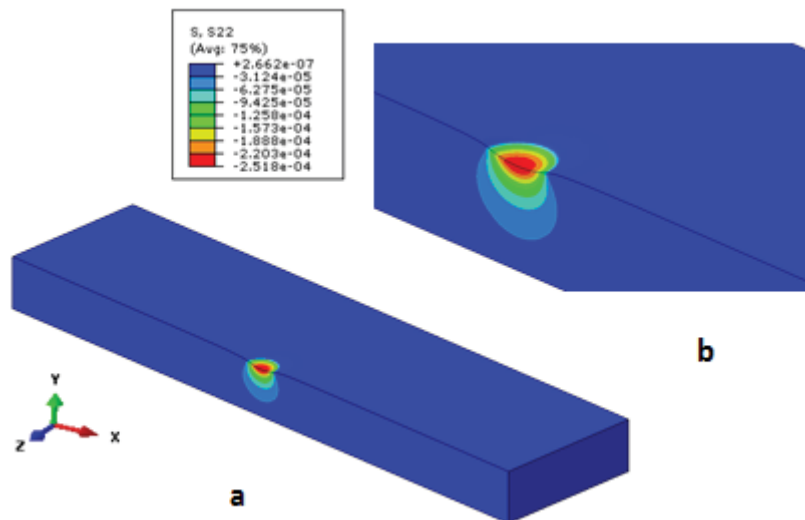


Figure 4.17: 3D image of Y stress component for 0% Mineralized collagen scaffold sample under full load of 0.5 mm displacement in the negative Y direction. (a) Shows full 3D half symmetry image of the scaffold model. (b) Shows zoom-in view of indented area under full load.

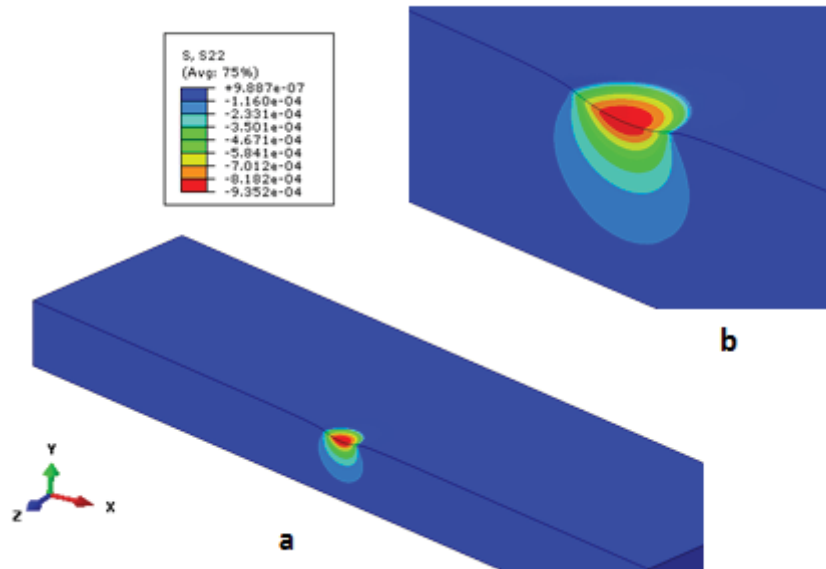


Figure 4.18: 3D image of Y stress component for 40% Mineralized collagen scaffold sample under full load of 0.5 mm displacement in the negative Y direction. (a) Shows full 3D half symmetry image of the scaffold model. (b) Shows zoom-in view of indented area under full load.

#### 4.5.2 FE simulation of multi- compartment scaffolds

##### 4.5.2.1 Two compartments with step interfaces

Figures 4.19 presented distribution of  $\sigma_{22}$  stress across the interface when indenting at the interface of the two compartments. ( $E= 700$  Pa at non-mineralized or CG compartment, and  $E=2550$  Pa at the mineralized or MCG). As shown, the stress component at the interface is continuous, but with a higher stress gradient as a result of the abrupt degree of stiffness change between the two compartments.

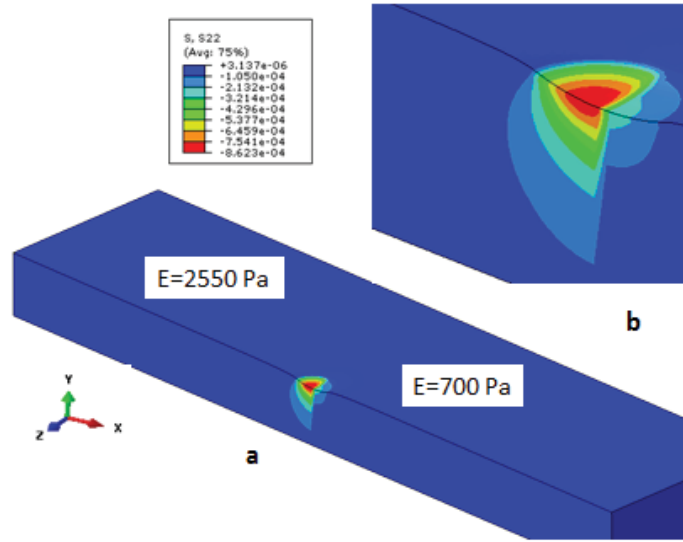


Figure 4.19: 3D image of  $\sigma_{22}$  stress component for two-compartment collagen scaffolds sample under full load of 0.5 mm displacement in the negative Y direction. (a) Shows full 3D half symmetry image of the scaffold model. (b) Shows zoomed in view of indented area under full load. 0% minerals on one end (left-side) and 40% minerals on the other side of the interface (right-side).

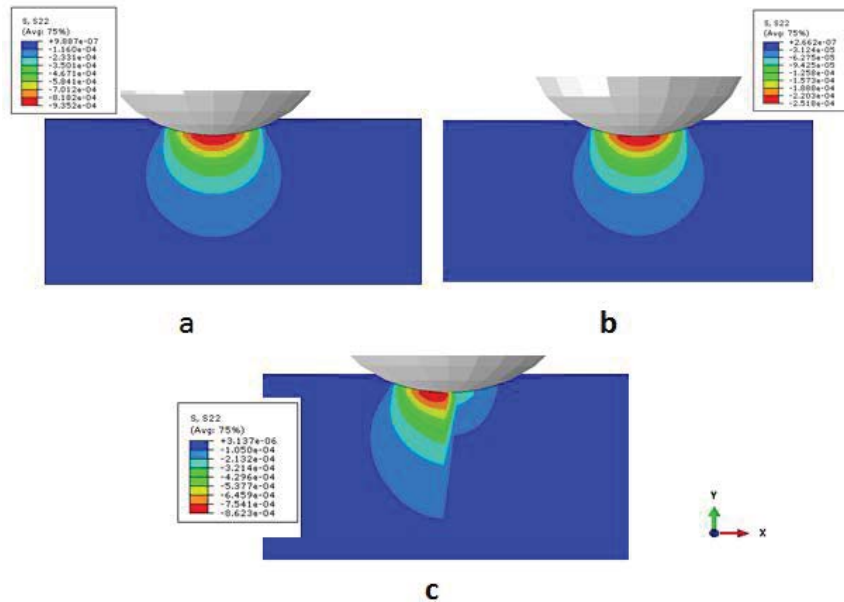


Figure 4.20: 2D image of  $\sigma_{22}$  stress component for three models. All of the stress plots are captured under full load of 0.5 mm displacement in the negative y direction; (a) 0% Mineralized

collagen scaffold sample with  $E=700$  Pa, (b) 40% Mineralized collagen scaffold sample with  $E=2550$  Pa (c) Two-compartment collagen scaffolds sample with  $E=700$  Pa on the left and  $E=2550$  Pa on the right of the interface.

Figure 4.21, 4.23 and 4.24 show  $\sigma_{11}$  stress components for 0% mineral, 40% mineral homogenous vs combine 0% and 40% heterogeneous samples.

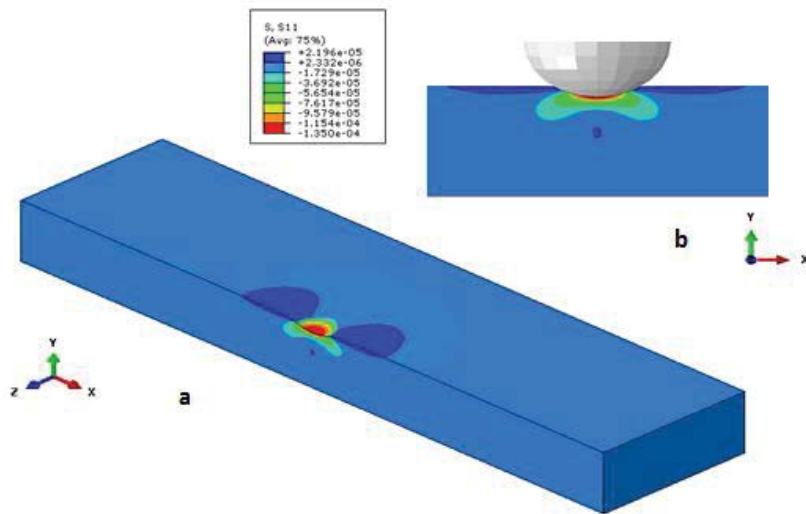


Figure 4.21: 3D image of  $\sigma_{11}$  stress component for 0% Mineralized collagen scaffold sample under full load of 0.5 mm displacement in the negative Y direction. (a) Shows full 3D half symmetry image of the scaffold model. (b) Shows zoom-in 2D view of indented area under full load.

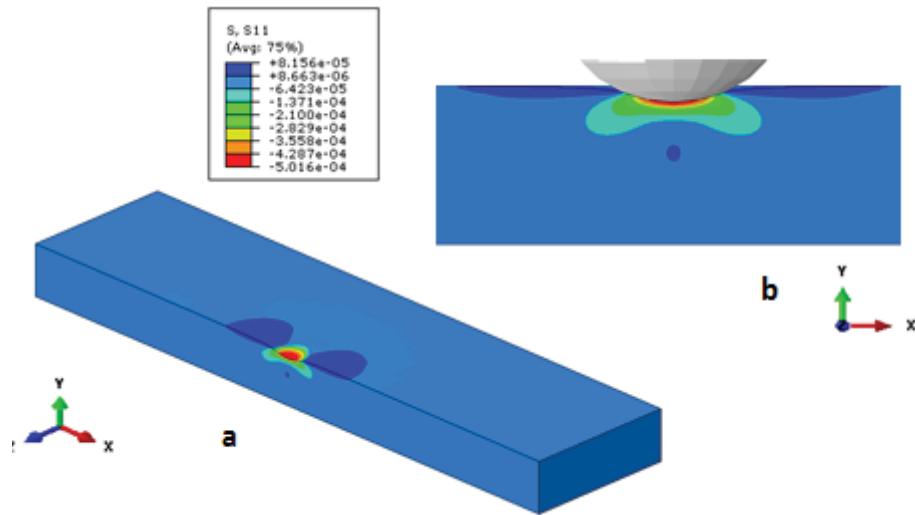


Figure 4.22: 3D image of  $\sigma_{11}$  stress component for 40% Mineralized collagen scaffold sample under full load of 0.5 mm displacement in the negative Y direction. (a) Shows full 3D half symmetry image of the scaffold model. (b) Shows zoom-in 2D view of indented area under full load.

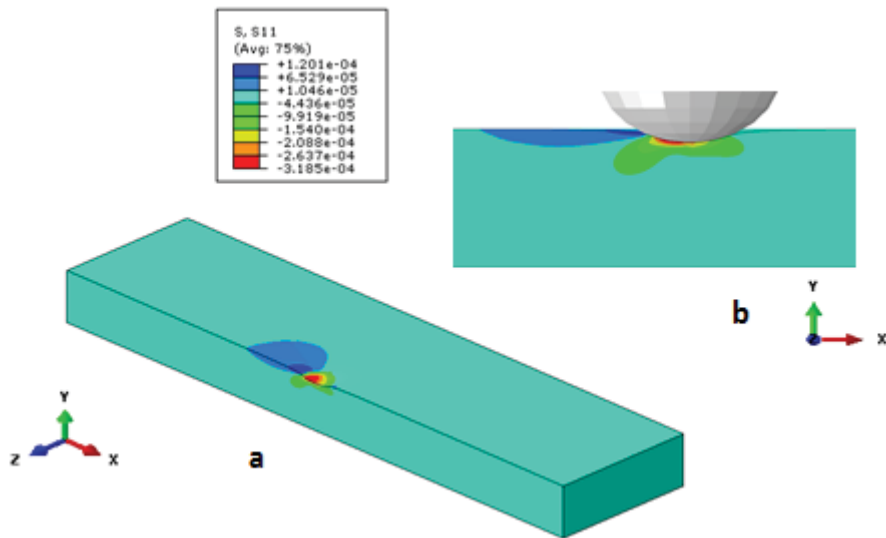


Figure 4.23: 3D image of  $\sigma_{11}$  stress component for two-compartment collagen scaffolds; combined 0% and 40% Mineralized collagen scaffold sample under full load of 0.5 mm displacement in negative Y direction. (a) Shows full 3D half symmetry image of the scaffold model. (b) Shows zoom-in 2D view of indented area under full load. 0% minerals on one end (left-side) and 40% minerals on the other side of the interface (right-side).

As shown in figure 4.23, the traction in the X direction is continuous across the interface, and is similar to the stress component in the Y direction. Shear stress symmetry is depicted for both 0% and 40 % mineralized conditions with respect to the YZ interface plane as shown in Figure 4.24 and 4.25. Shear stress values are similar on both sides of the indenter. Higher shear stress magnitude is shown in the 40% mineralized collagen in the two-compartment scaffolds, as shown in figure 4.26.

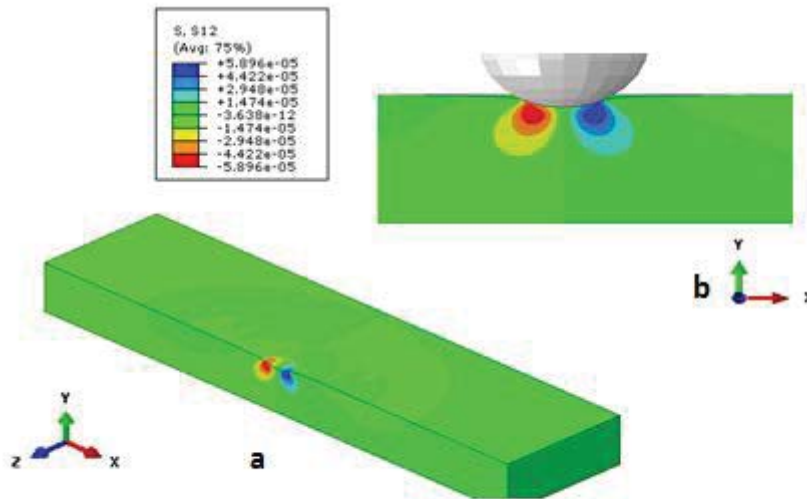


Figure 4.24: 3D image of  $\sigma_{11}$  stress component for 0% Mineralized collagen scaffold sample under full load of 0.5 mm displacement in the negative Y direction. (a) Shows full 3D half symmetry image of the scaffold model. (b) Shows zoom-in 2D view of indented area under full load.

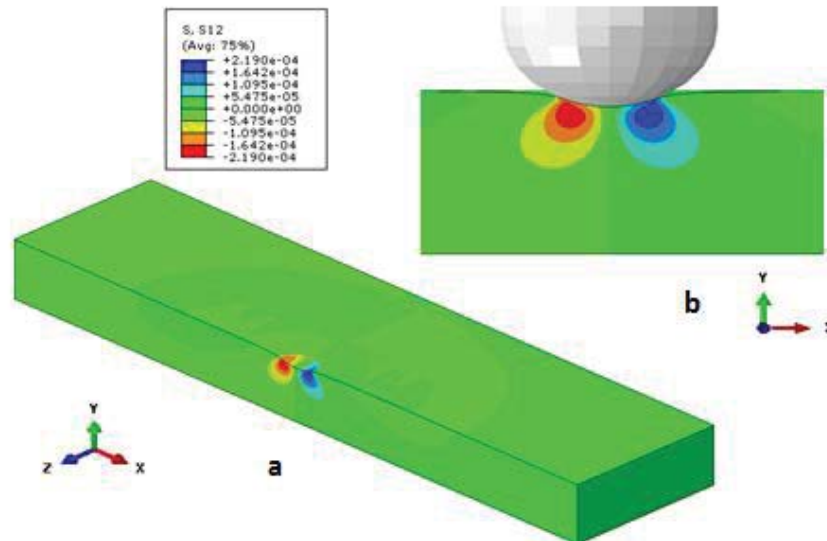


Figure 4.25: 3D image of  $\sigma_{12}$  stress component for two-compartment collagen scaffolds; combined 0% and 40% Mineralized collagen scaffold samples under full load of 0.5 mm displacement in the  $-Y$  direction. 0% minerals on one end (left-side) and 40% minerals on the other side of the interface (right-side).

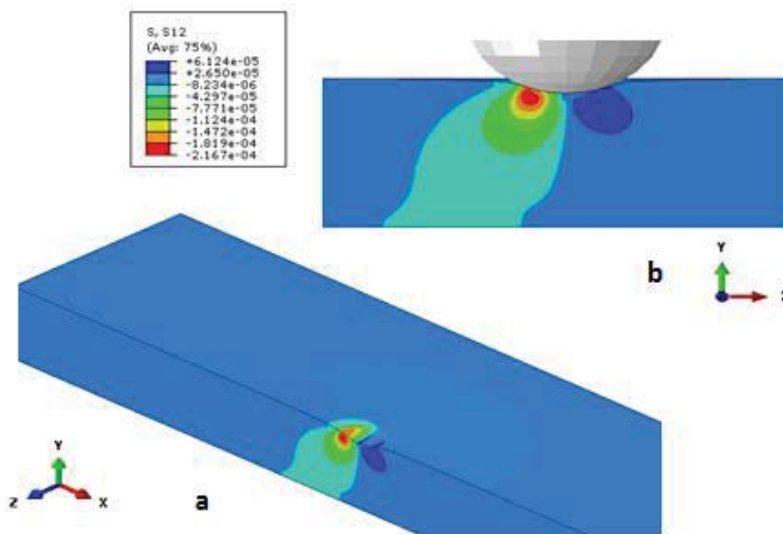


Figure 4.26: 3D image of  $\sigma_{12}$  stress component for two-compartment collagen scaffolds; combined 0% and 40% Mineralized collagen scaffold sample under full load of 0.5 mm displacement in the negative  $Y$  direction. (a) Shows full 3D half symmetry image of the scaffold model. (b) Shows zoom-in 2D view of indented area under full load. 0% minerals on one end (left-side) and 40% minerals on the other side of the interface (right-side).

Figure 4.27 shows the elastic modulus values at  $\pm 2.5$  mm away from the interface where a series of 17 FE indentations were performed at locations shown on the X axes. Black diamond markers represent the elastic modulus values at the indentation locations. These values diverge significantly from the intrinsic values of the two levels on both sides of the interface. In addition, the E values at these locations exhibit asymmetric behavior because the E values converge faster toward the intrinsic value of E on the non-mineralized side of the interface.

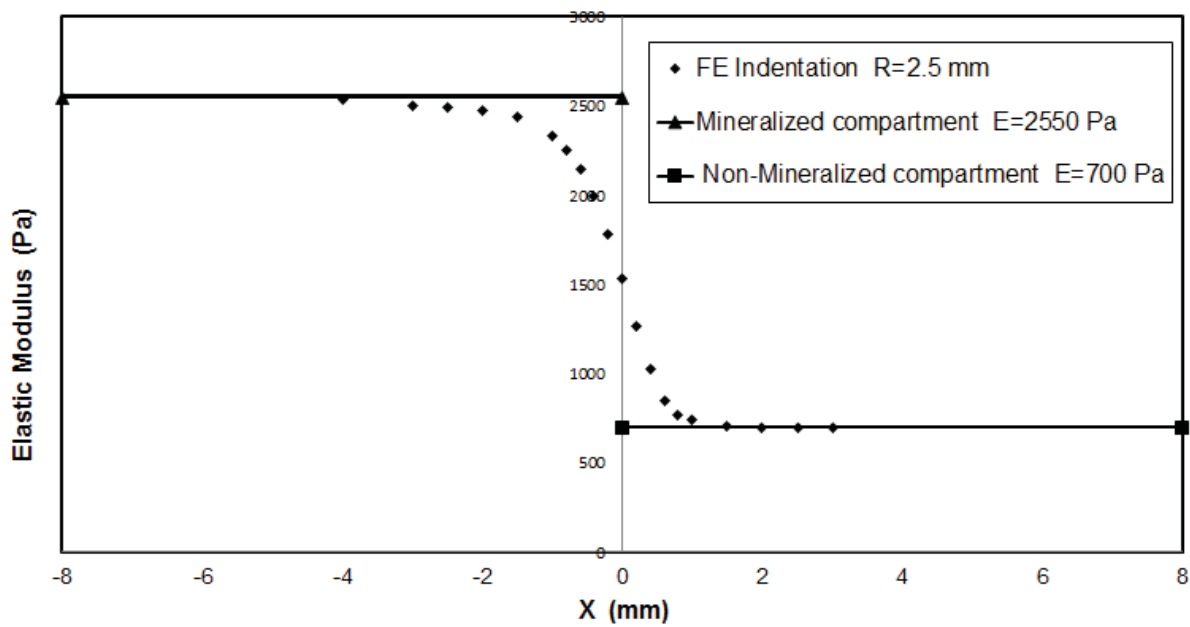


Figure 4.27: Elastic modulus at  $\pm 2.5$  mm on both sides of interface is shown with black diamond markers. There is a clear bias and difference between elastic modulus values obtained from FE indentation vs. the intrinsic values associated with each individual material.

#### 4.5.2.2 Two Compartments with a ramp interface

The  $\mu$ CT scan shown in Figure 4.1 indicates that the actual interface is not a sharply-defined step. It is instead graded, which results in stiffness variance. Therefore, we need to enhance our approach using an interface with a gradient. We model the gradient as a series of four small steps, and each step is  $160 \mu\text{m}$  wide with two elements across the width. An elastic

modulus was assigned to each step based on the values obtained from indentation tests performed on the monolithic samples. Figure 4.28 shows the compressive stress plot of the FE indentation with a graded interface.

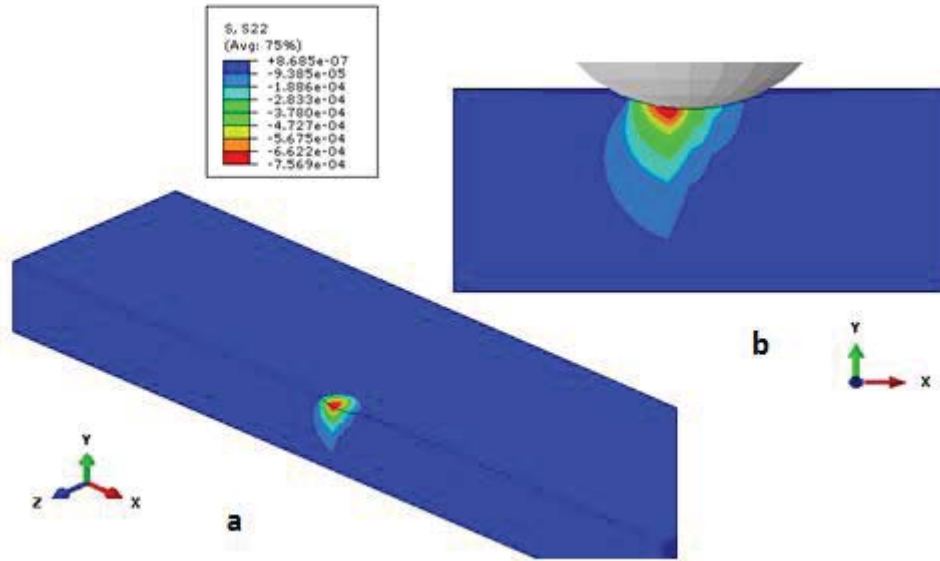


Figure 4.28: 3D image of  $\sigma_{22}$  stress component for two-compartment collagen scaffolds sample with a graded interface under the full load of 0.5 mm displacement in the negative Y direction. (a) Shows full 3D half symmetry image of the scaffold model. (b) Shows zoom-in 2D view of indented area under full load. 0% minerals on one end (left-side) and 40% minerals on the other side of the interface (right-side).

Stress continuity is observed with less stress gradient compared to the FE results with a sharp interface as shown in figure 4.19. Figure 4.29 shows  $f$  (original or intrinsic) is represented as having 4 steps over 5 levels of elastic modulus. It also shows  $y_{FE}$  which represents the FE indentation results at 17 different locations around the interface. Elastic modulus bias, which is a result of the material boundary conditions, was observed. The discrete ramp of the FE simulation curve crosses the  $x=0$  axis at a different stiffness level than what was seen with the sharp step interface. This is due to a gradual change in the degree of stiffness between the

mineralized and non-mineralized parts of the scaffold. The overall behavior of elastic modulus measurement bias with respect to intrinsic values is still similar to the one which was observed with the sharp step considering that we limited the step width to  $460\ \mu\text{m}$ .

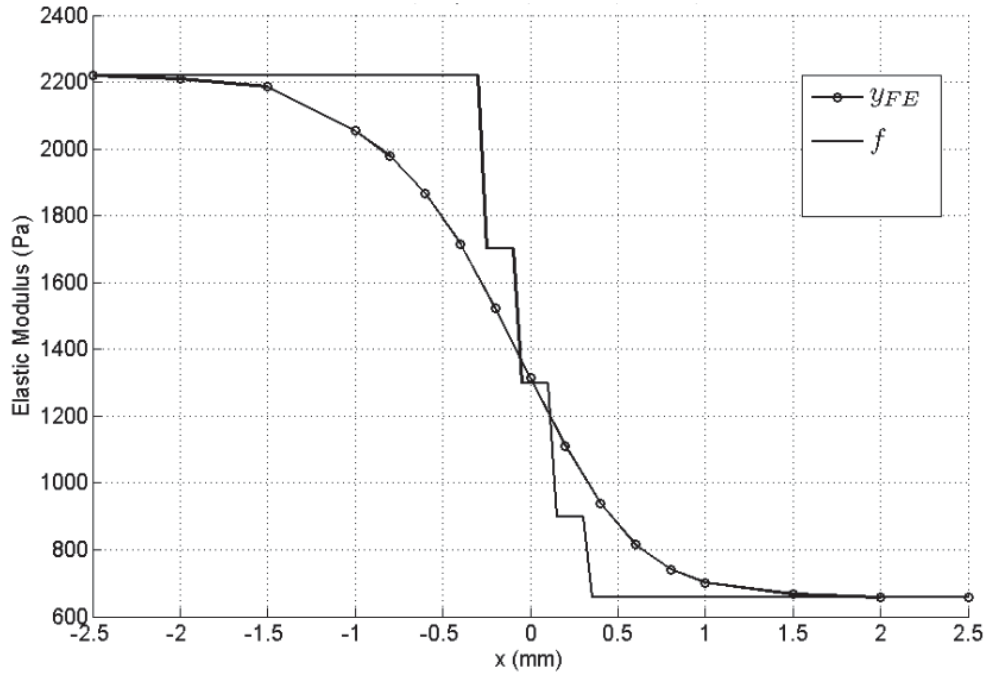


Figure 4.29: Ramp interface was molded using 4 small steps. Elastic modulus at  $\pm 2.5$  mm on both sides of the step-stairs interface is shown using a black line with circle markers. There is a clear bias between elastic modulus values obtained from FE indentation vs. the intrinsic values assigned to all steps.

## 4.6 Inverse Solution

### 4.6.1 Step interface

Using piecewise linear sigma values generated from the forward solution which solve the inverse problem following Equation 4.4, we find an estimate of the intrinsic elastic modulus  $\hat{f}$ .  $\hat{f}$  denotes our model prediction for elastic modulus after de-correcting the measurement bias which resulted from material heterogeneity around the interface. The dark circle markers shown in figure 4.30 show that the elastic modulus values are much closer to the intrinsic elastic modulus,

which is indicated by  $f$ .  $\hat{f}$  was generated after adding random noise with a variance of 3dB to  $y_{FE}$  in order to model measurement noise.

Amplitude value is determined from testing monolithic scaffolds by performing multiple indentations at the same location. In order to eliminate the ripples in the inverse solution caused by sharp interfaces, we used a smoothing median filter and adjusted its window size to the period of oscillations. This period is different on the two sides of the interface, which makes it impossible to eliminate all of the oscillations by using a fixed window size. The result is that we observe minimal oscillations in Figure 4.30, and these are the result of this problem.

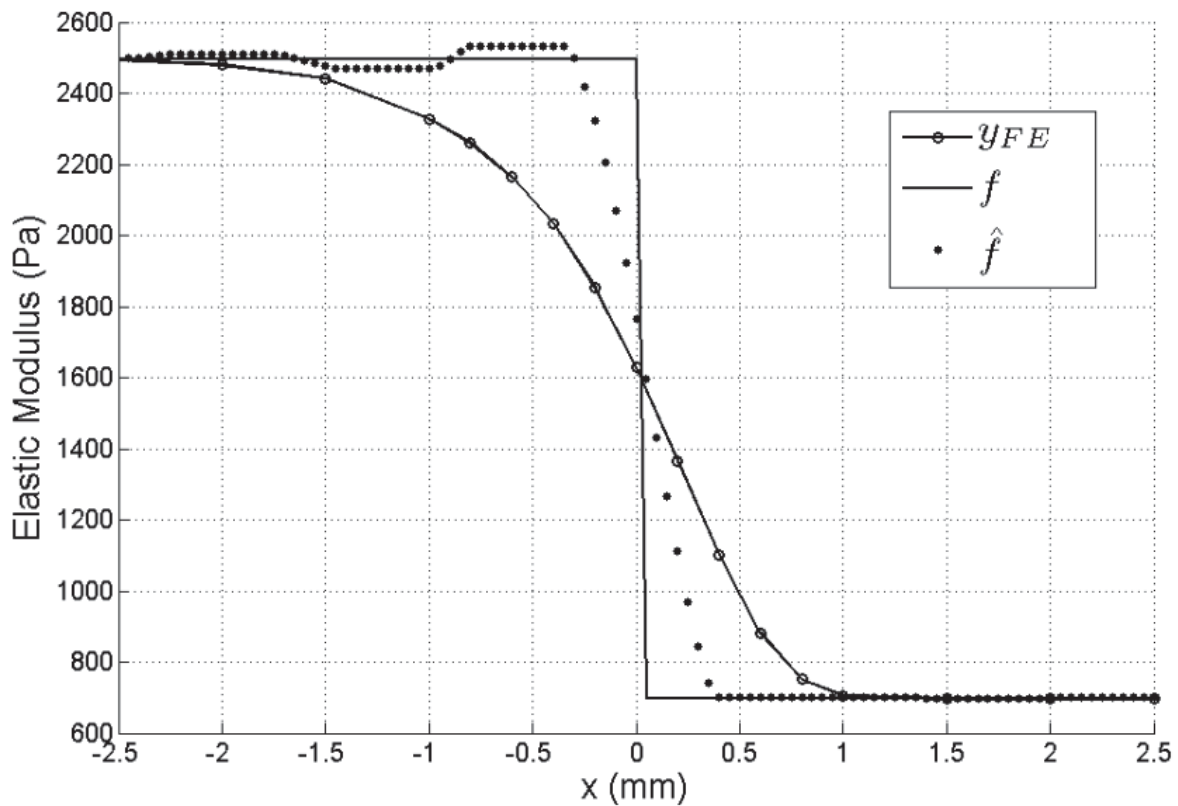


Figure 4.30: Inverse solution,  $\hat{f}$ , is shown with black circle markers representing the correction to the E values obtained from  $y_{FE}$ .  $y_{FE}$ , is shown using a black line with circle markers which represent E values obtained from FE simulation.  $f$  is shown with a black line which represents the intrinsic E values assigned to each side of the interface.

The results show  $\hat{f}$  is making a considerable correction to indentation data. For example, an E value of  $\hat{f}$  at a 0.4 mm distance from interface reflects the intrinsic properties of each compartment. E of  $y_{FE}$  shows 1100 Pa to the right of the interface, and 1950 to the right of the interface. However, at approximately a 0.35 mm distance from the interface, the bias still exists. This is due to the indenter size (R=2.5 mm) being large and still engaging considerable material on each side of the interface. This indicates that a smaller indenter could provide better spatial resolution and that the simulation results of elastic modulus would be closer to the intrinsic ones.

#### 4.6.2 Ramp interface

As noted in section 4.5.2.2, the ramp interface was modeled using 4 steps in order to generate  $y_{FE}$ . Once  $y_{FE}$  is obtained and we make use of sigma values developed for sharp step interfaces, we can solve the inverse problem by using Equation 4.4 to find  $\hat{f}$  for the ramp interface. The dark circle markers shown in Figure 4.31 present our model correction for elastic modulus values, and we compared them with the ones obtained by numerical indentation  $y_{FE}$ . In a manner similar to the sharp step interface, random noise with variance was added to  $y_{FE}$ , and a median filter was used as an inverse solution. It oscillated around the means at both ends of the interface stiffness. Elastic modulus values associated with  $\hat{f}$  reflect significant improvement over the ones which were associated with  $y_{FE}$  when compared with the intrinsic values represented by  $f$ .

The discrepancy shown to the right of the interface is an artifact which results from using a constant window size for the median filter.

In addition, the interface generated by  $\hat{f}$  is shifted to the left of the original interface location due to the indenter size compared to the step width within the interface.

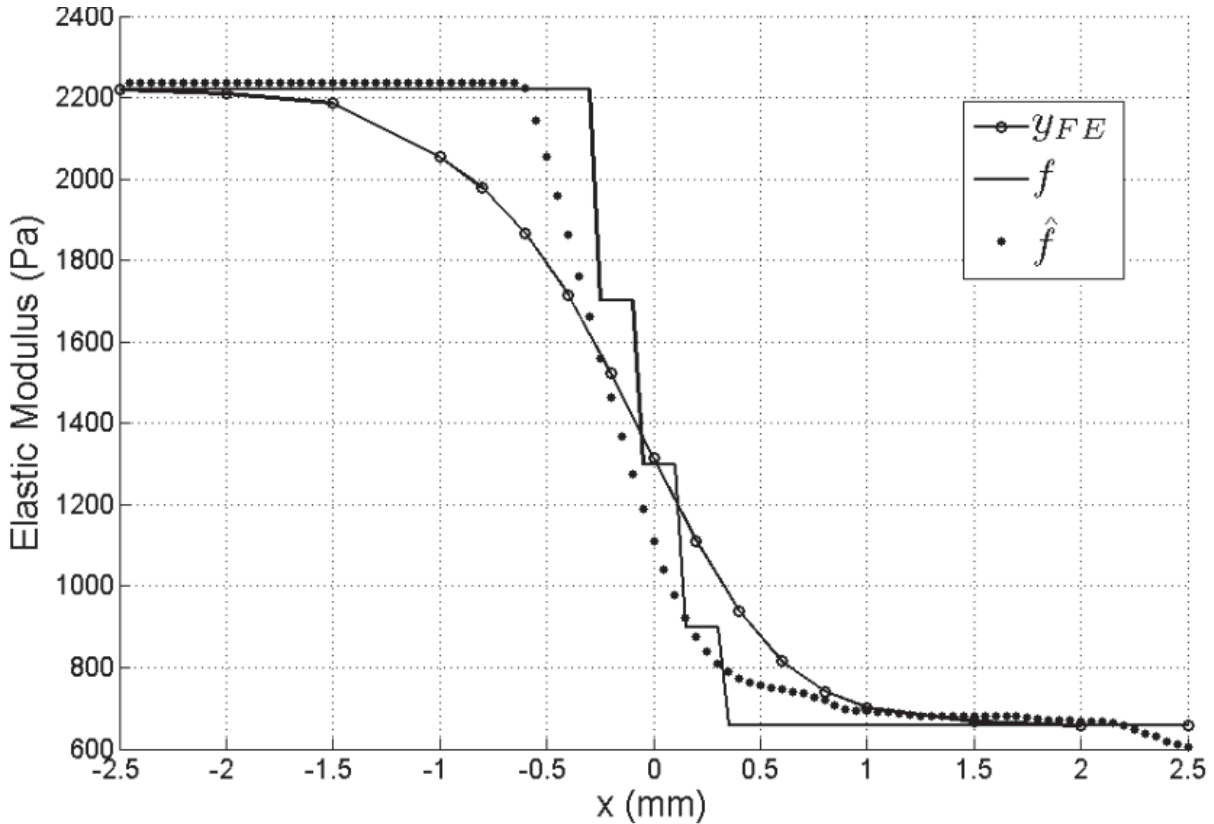


Figure 4.31: Inverse solution,  $\hat{f}$ , is shown with black circle markers which represent the correction to E values obtained from  $y_{FE}$ .  $y_{FE}$ . It is shown with a black line with circle markers which represent E values obtained from the FE simulation.  $f$  is shown with a black line which represents intrinsic E values assigned to the steps.

## 4.7 Discussion

### 4.7.1 Monolithic scaffolds testing and UCT imaging

Monolithic scaffolds indentation provided the benefit of validating the finite element model, which is an enabling step towards the establishment and validation of our novel new approach to stiffness prediction across interfaces. That information, coupled with the  $\mu$ CT of two

compartment scaffolds, provided us with the opportunity to create a stiffness gradient for the purpose of simulation the ramp interface.

Figure 4.32 shows that we combined the monolithic scaffolds pixel intensity obtained from  $\mu$ CT imaging with the elastic modulus obtained from indentation testing. These results present an opportunity to link the elastic modulus to gray-scale pixel intensity, which will provide a quick and easy way of approximating the elastic modulus based on the  $\mu$ CT images of multi-compartment scaffolds. We do not anticipate that the elastic modulus values obtained from  $\mu$ CT images will be fully accurate, due to errors associated with averaging pixel intensity and setting a reference frame for the gray scale. Nevertheless, we believe that such approximations have value because they are easy to obtain and therefore have the potential to aid the multi-compartment manufacturing process by providing rapid feedback concerning the stiffness gradient.

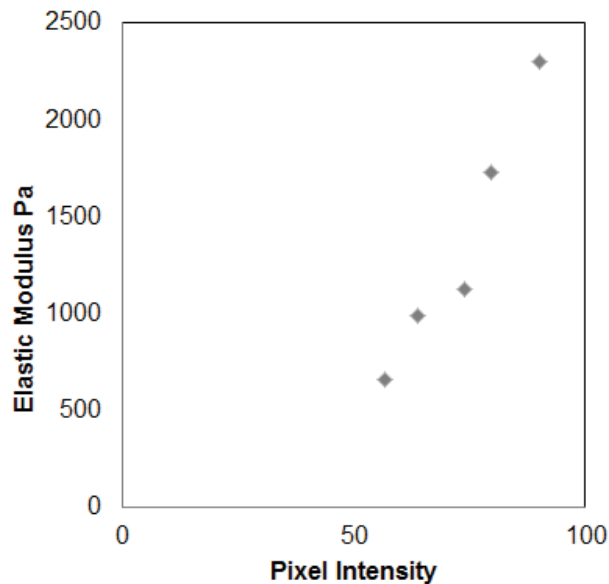


Figure 4.32: Elastic modulus vs. pixel intensity obtained from  $\mu$ CT of monolithic scaffolds five points shown are for 5 mineral concentrations, (0%,10%,20%,30%,40%), respectively.

Pixel intensity is increasing in a linear manner with elastic modulus. The third point representing 20% minerals deviates from the regression line due its reported elastic modulus value.

#### 4.7.2 Correction for elastic modulus

There are significant improvements in estimations of the elastic modulus values that are produced by processing macro-indentation results when using our model and the inverse solution. Commonly used contact models introduce significant errors into the prediction of the elastic modulus when used in conjunction with multi-compartment scaffolds. The inverse solution represented by  $\hat{f}$  for step and ramp interface is shown in Figures 4.30 and 4.31, and provides a substantial improvement in predictions of intrinsic values. Figures 4.33 and 4.34 show the percent error reduction for both sharp and ramp (represented by 4 small steps) interfaces.

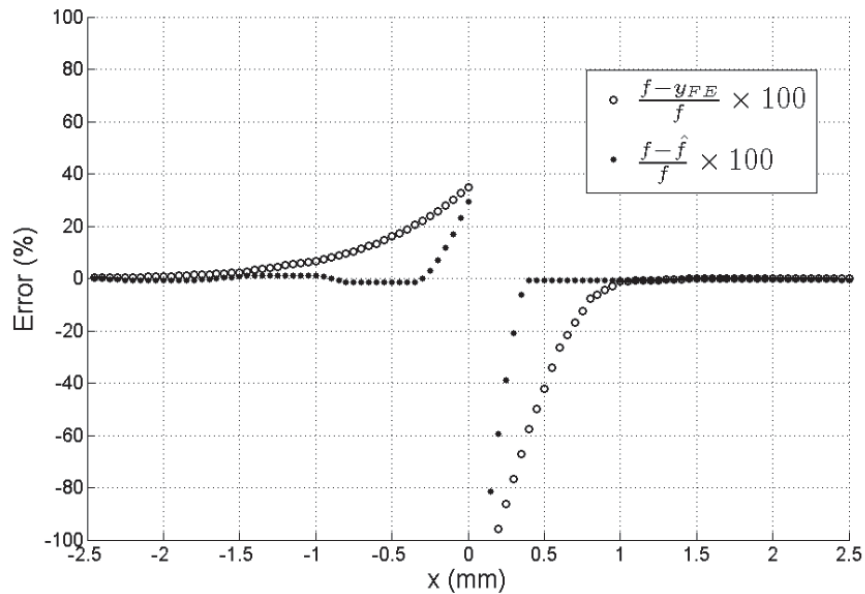


Figure 4.33: Percent error reduction obtained when comparing  $y_{FE}$  and  $\hat{f}$  to  $f$  for sharp step interfaces with a 2.5 mm indenter radius.

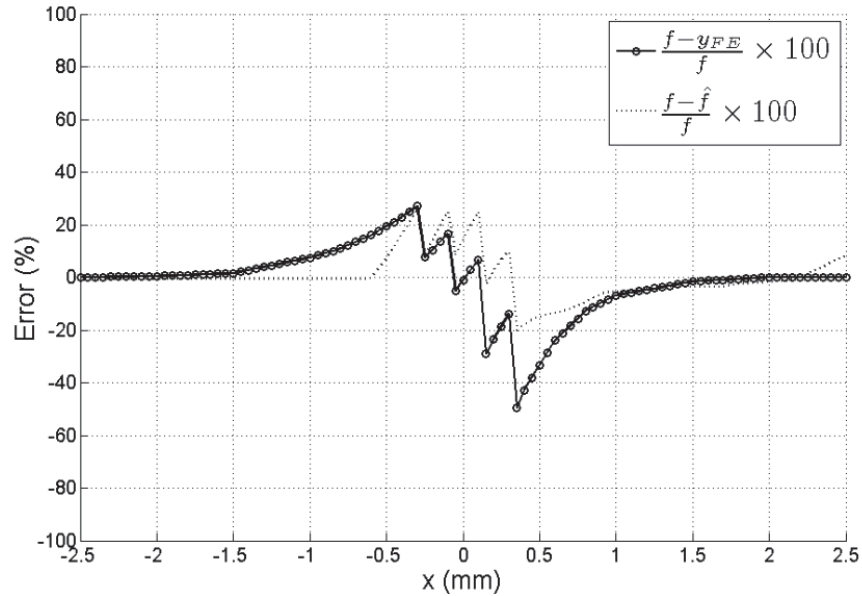


Figure 4.34: Percent error reduction when comparing  $y_{FE}$  and  $\hat{f}$  to  $f$  for a ramp interface with a 2.5 mm indenter radius.

Figure 4.33 shows that errors in elastic modulus are reduced by 60% at an approximate distance of +0.4 mm from the interface and by 20% at an approximate distance of -0.4 mm from the interface. Given the very sharp step interface, the results are numerically unstable at the interface, and tend to overshoot. More reliable data can be found in Figure 4.34, with 4 steps representing the ramp interface, where the largest error range is reduced from 50% to less than 20%.

Another aspect that can influence the measurement bias is related to indenter size. Reducing indenter size also reduces its contact area with the sample. Therefore, we expect to reduce the contribution to the local modulus values from the adjacent material with different degrees of stiffness, hence reducing the sigma values of the Gaussian filter and reducing the blurring between the elastic modulus from simulation data vs intrinsic one.

Next, we examined the effect of indenter size on predictions regarding the intrinsic modulus by reducing the probe radius from 2.5 mm to 1.25 mm, and later reduced it to 0.625 mm. The FE indentation simulation results for the sharp step interface when using different indenter sizes are shown in Figure 4.35. Elastic modulus values obtained using an indenter with 1.25 mm radius are closer to intrinsic values in comparison with elastic values obtained when using a 2.5 mm indenter radius. The modulus values that were obtained with a 0.625mm indenter radius converge even closer to the intrinsic values than 1.25mm.

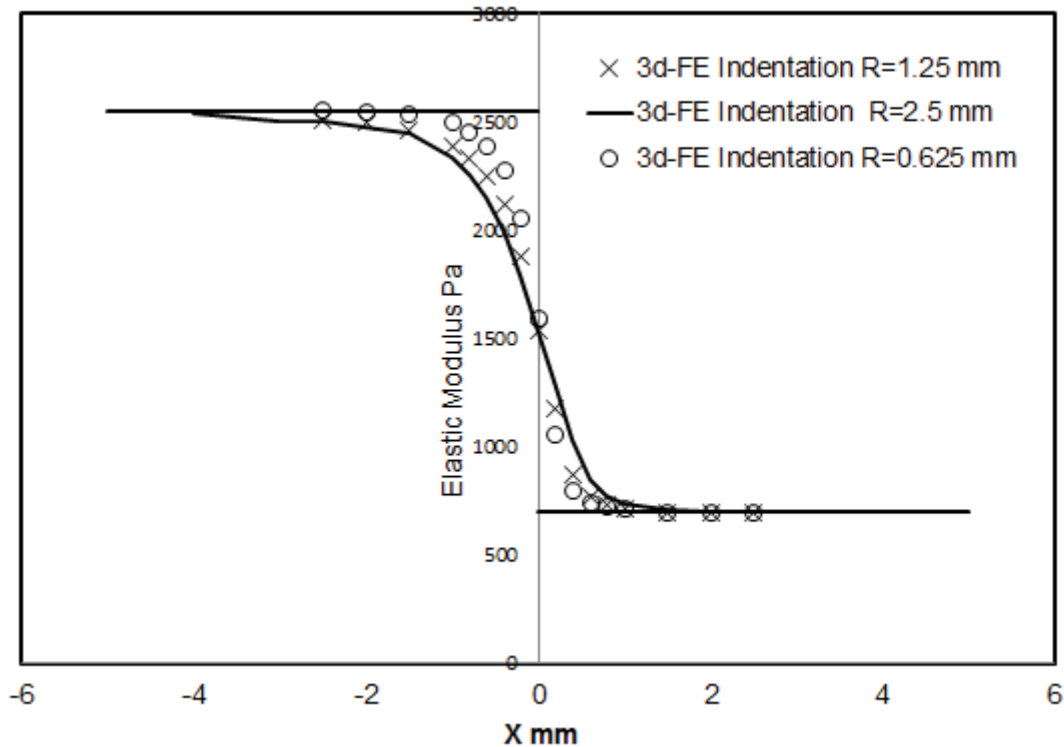


Figure 4.35: Elastic modulus at  $\pm 2.5$  mm on both sides of interface is shown with black line x shape, and circle shape markers show elastic modulus values using indenter size  $R=1.25$  mm and  $R=0.625$  mm respectively. Bias between elastic modulus values obtained from FE indentation vs. the intrinsic values is reduced as indenter size is reduced.

As indenter radius get smaller the pressure forces under the probe are reduced and localized resulting in less blurring effect from interface, and therefore produce measurement with less bias. It is noted that as indenter radius is reduced the spread between the elastic modulus produced using FE models vs the intrinsic, more on the stiffer side of the scaffolds com on the softer side as indenter radius is reduced

Following the same process used with the original 2.5 mm indenter, we reproduced the sigma values for 1.25 mm and 0.625 mm indenters using a forward solution for the step interface. Figures 4.36 and 4.37 show the sigma values vs. position with respect to the interface.

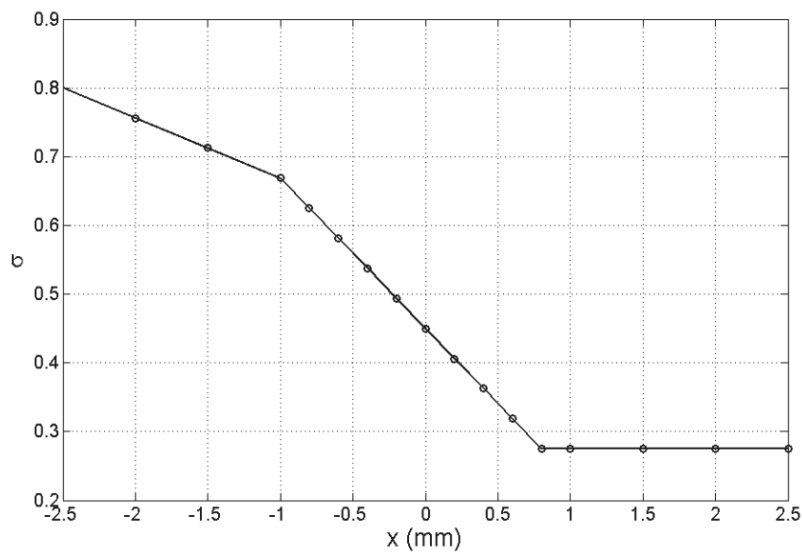


Figure 4.36:  $\sigma$  values plotted vs. measurement location for a 1.25 mm indenter.

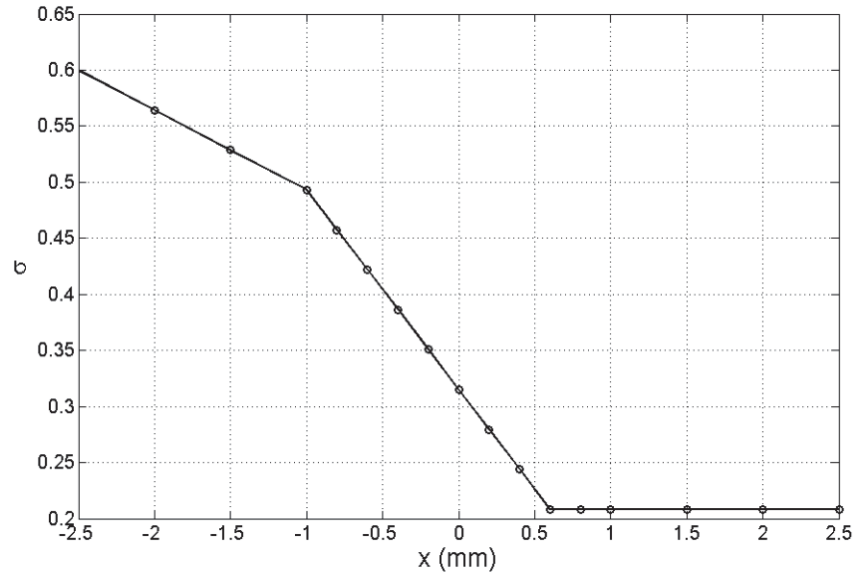


Figure 4.37:  $\sigma$  values plotted vs. measurement location for a 0.625 mm indenter.

As expected, the values for sigmas of the Gaussian filter model were reduced as we decreased indenter size. This confirms our interpretation of the physical meaning of sigma, as mentioned earlier. Using the sigma values plotted above for both of the indenters, and solving the inverse as was done for 2.5 mm indenter, leads us to obtain and compare  $\hat{f}$  for three probe sizes as shown in Figure 4.38.

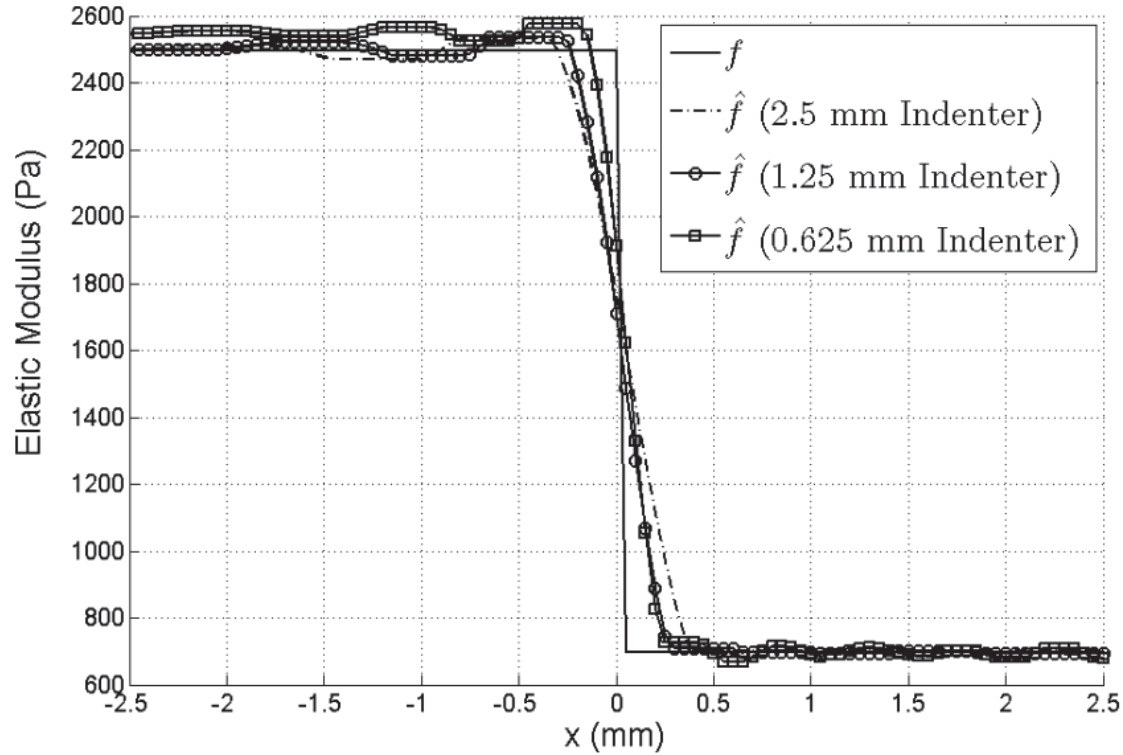


Figure 4.38:  $\hat{f}$  with different size indenters vs.  $f$  for step interfaces

In general, the elastic modulus values that were obtained using a smaller indenter converge closer to scaffolds intrinsic values. Modulus values obtained for stiffer material (the mineralized side of the interface) are more sensitive to probe size changes than the one obtained for softer material side. As distance from the interface increases, the correlation effect modeled by Gaussian filtering becomes negligible. We assume that a constant sigma after attaining a certain distance will not affect the model prediction results, particularly on the softer side where the Gaussian filter is very narrow.

Figures 4.39 and 4.40 show a reduction in percent error between  $y_{FE}$  and  $\hat{f}$  when compared with intrinsic values  $f$  for 1.26 and 0.625 mm indenters.

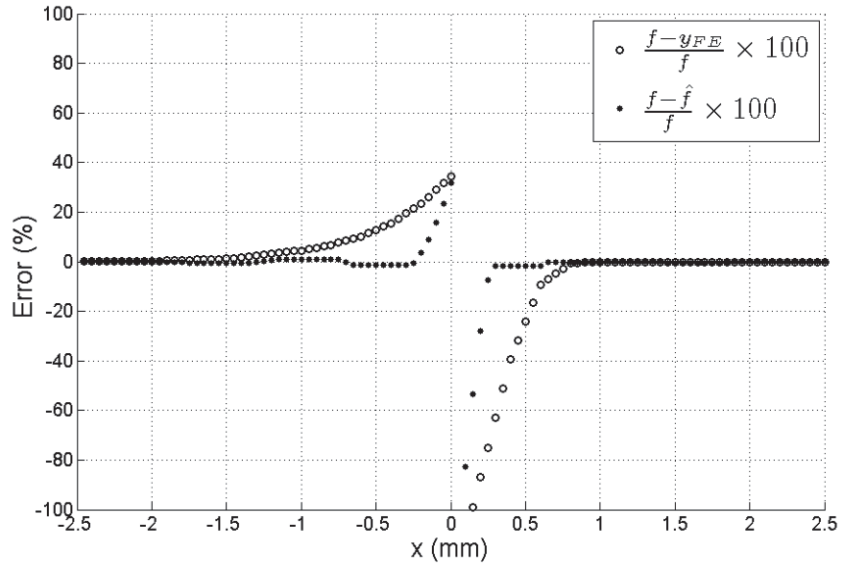


Figure 4.39: Percent error reduction when comparing  $y_{FE}$  and  $\hat{f}$  to  $f$  for a sharp step interface with a 1.25 mm indenter radius.

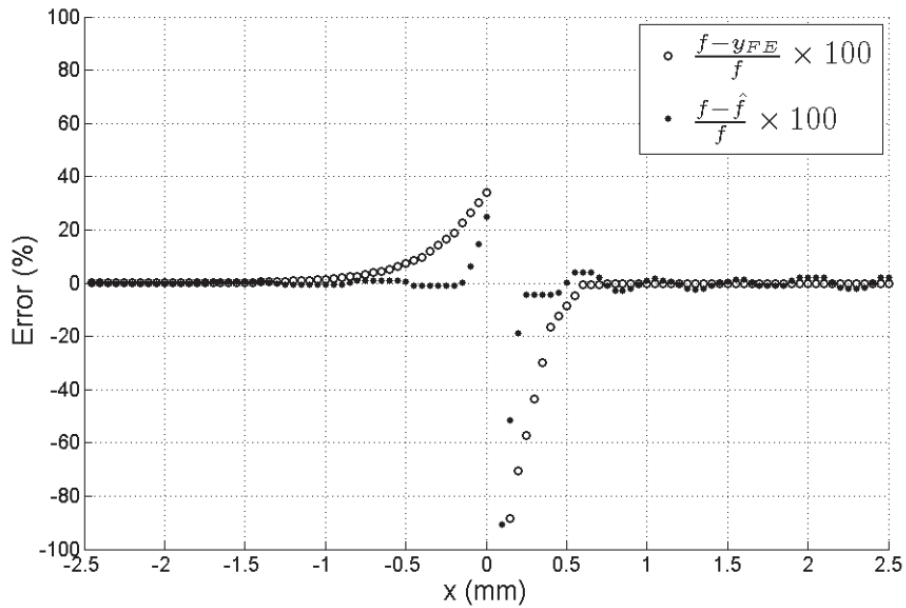


Figure 4.40: Percent error reduction when comparing  $y_{FE}$  and  $\hat{f}$  to  $f$  for sharp step interfaces with a 0.625 mm indenter radius.

An indenter with  $R=0.625$  outperforms other indenters in terms of measurement bias reduction and ability to approach the interface. However, both the 1.25 mm and 0.625 mm radius indenters appear to perform equally on the softer side of the interface.

It should be noted that although reducing indenter size improves measurement bias compared with intrinsic modulus values, it does bring up other challenges for indentation accuracy, such as force-to-noise ratio as taken from actual measurements. Given our monolithic indentation measurements, a reduction in indenter size will increase error in force measurements, as shown in Figure 4.41.

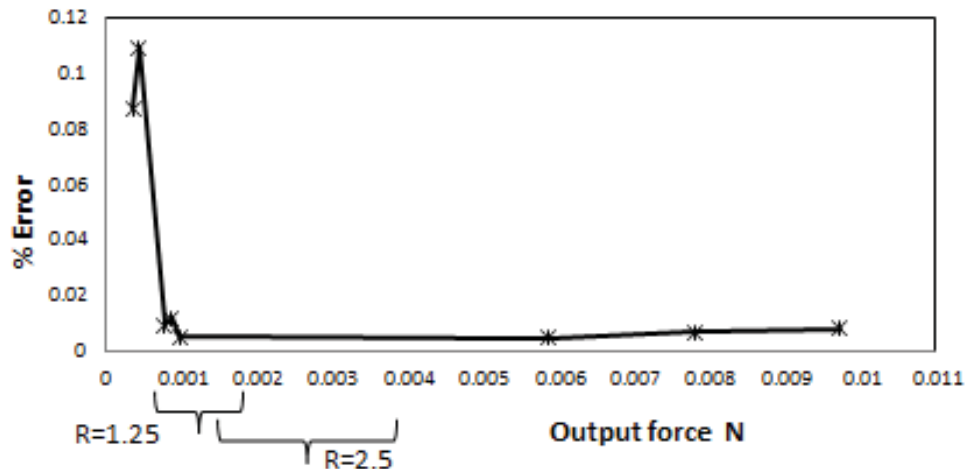


Figure 4.41: Percent error in force measurement vs. indentation force measured when using a 1kg load cell. The small bracket is for ranges of force seen for the indenter with a 1.25 mm radius, and the big bracket is for ranges observed when the indenter has a 2.5 mm radius.

Each bracket represents a range of force measured using indenter size (R), when indenting scaffolds at stiffness levels that correspond to 0% and 40% minerals.

In a manner similar to measured data, when processing the inverse problem numerically, the solution tends to be unstable when the sigma values are quite small, particularly when using a 0.625 mm indenter radius.

Changing the indenter radius from 2.5 mm to 1.25 mm yielded a substantial improvement for the ramp interface. Figure 4.42 shows that the elastic modulus values represented by  $\hat{f}$  closer to the intrinsic values, and the slope of the interface generated by  $\hat{f}$  shows an improvement over the one obtained when using an indenter with a 2.5 mm radius, as shown in Figure 4.17.

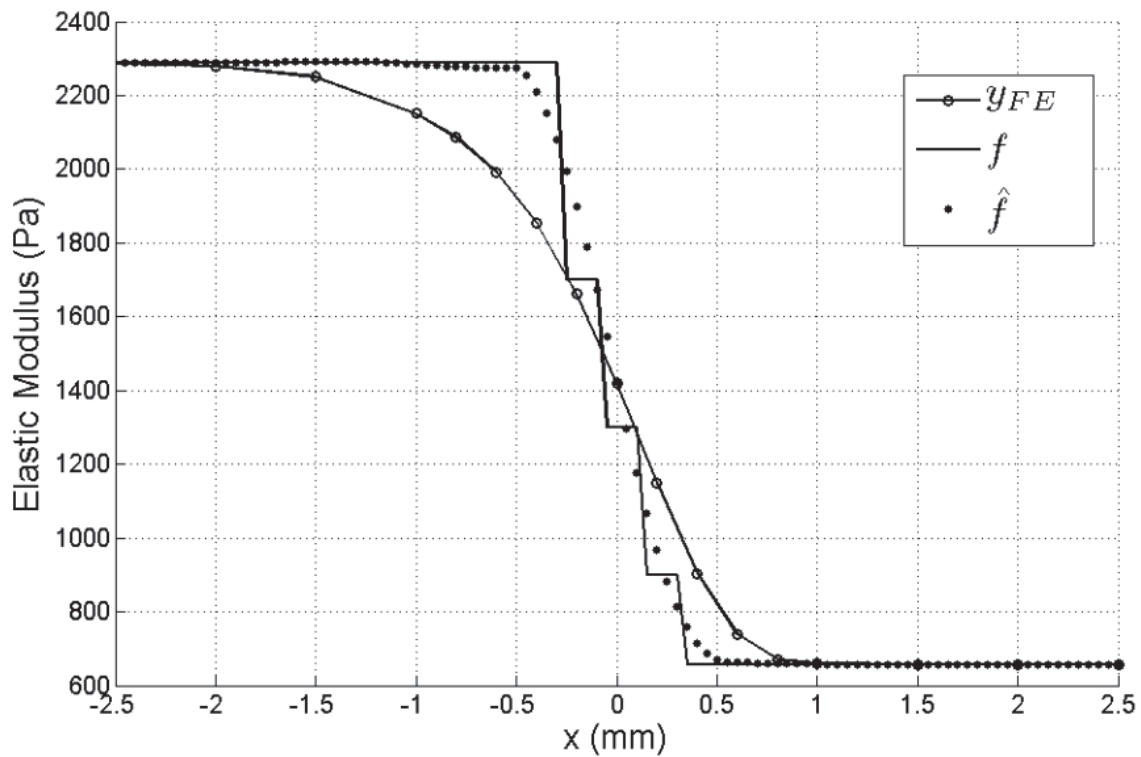


Figure 4.42: Inverse solution,  $\hat{f}$  is shown using black circle markers which represent the corrections to E values obtained from  $y_{FE}$ .  $y_{FE}$  is shown with a black line with circle markers which represent the E values obtained from FE simulation.  $f$  is shown with a black line which represents the intrinsic E values assigned to the steps.

A significant reduction in elastic modulus percent error was observed when an indenter radius of 1.25 mm was used. Figure 4.43 shows that the overall percent error range was reduced from (-60%, +25%) to (-18%, +10%).

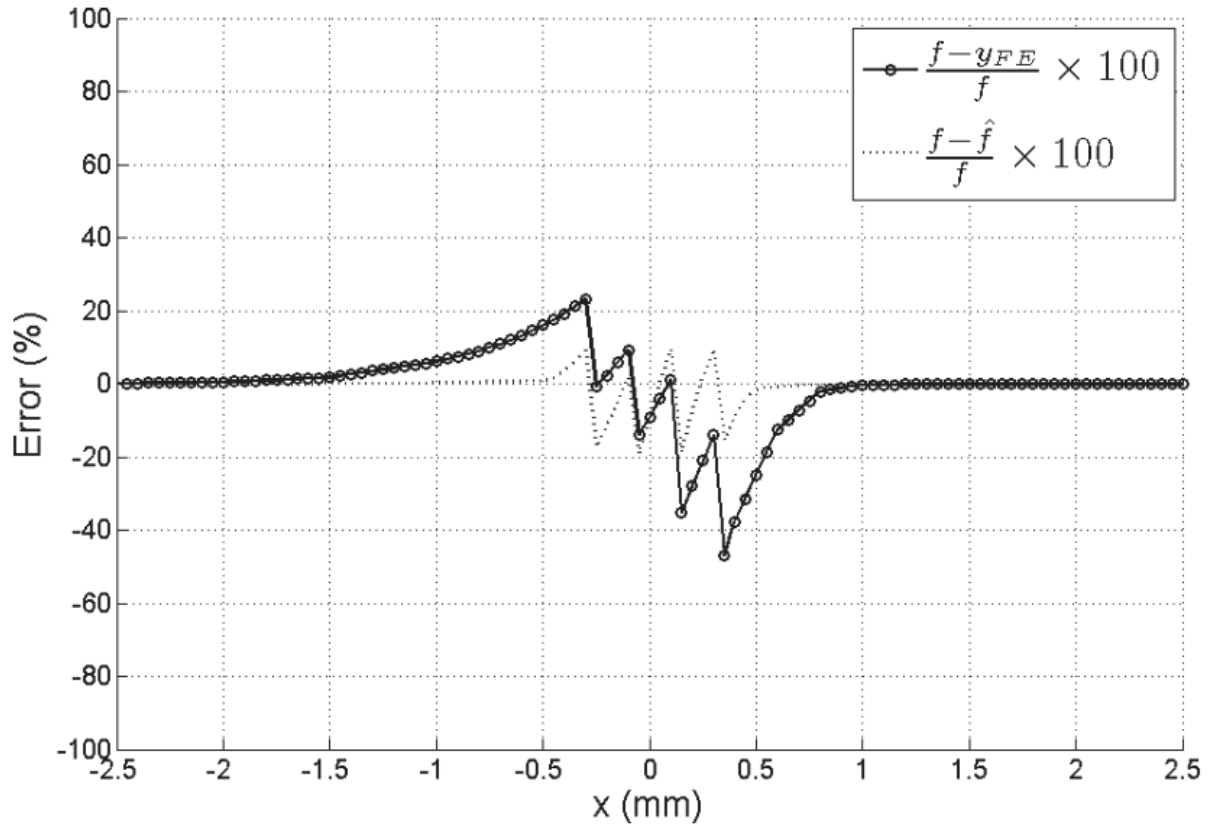


Figure 4.43: Percent error reduction when comparing  $y_{FE}$  and  $\hat{f}$  to  $f$  for ramp interfaces with a 1.25 mm indenter radius.

Other aspects to consider when evaluating indenter probe sizes are spatial resolution, and pore size. A pore size of (90-131  $\mu\text{m}$ ) was a characteristic of the monolithic scaffolds considered in our study [12]. Pore size is a critical limitation due to its effect on cell mobility and adhesion [6, 8]. Therefore, we recommend limiting the indenter size to a 1.25 mm hemispherical indenter because it is near 10 times the pore size of (90- 131  $\mu\text{m}$ ).

This is critical because our objective is to measure the scaffold bulk modulus and not to be limited with respect to the microstructure interaction. Our indenter size limit also takes into consideration the ability to maintain the bulk modulus measurements after the scaffolds are seeded with cells.

One important observation was that the ability of the inverse solution method to estimate the intrinsic values is limited by either the width of the interface, or the sharpness of the ramp, in addition to the size of the indenter. We measured the accuracy of the estimation using a mean square error (MSE), and normalized it using the square of the absolute value of  $f$ . As noted in Figure 4.44, for a fixed indenter size, the MSE decreased as interface width increases. On the other hand, for a fixed interface width, the MSE decreases as indenter size decreases. Therefore, an indenter with a 0.625 mm radius provides the right balance between pore size and interface width.

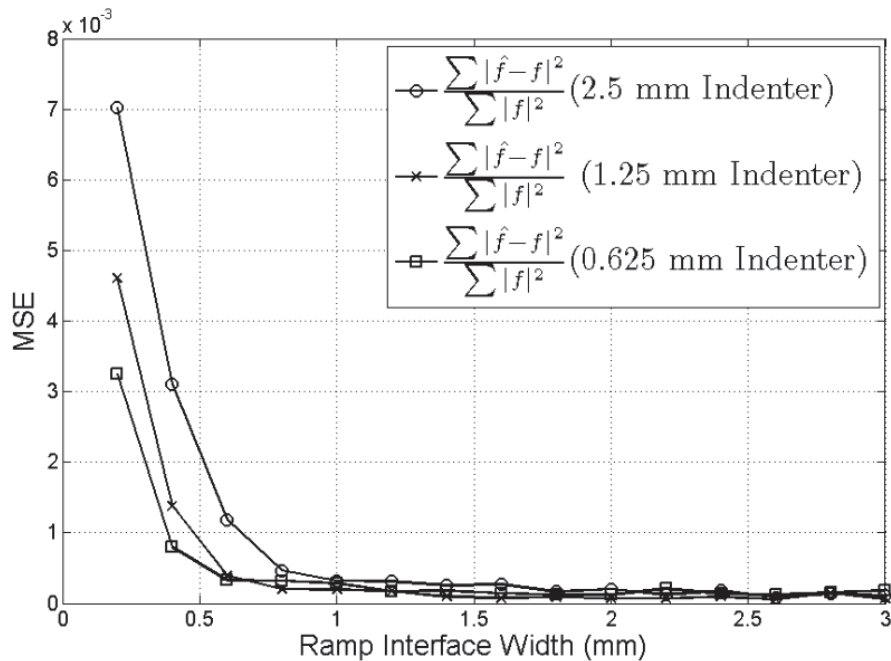


Figure 4.44: MSE of  $\hat{f}$  divided by square of  $f$  vs. ramp interface width for indenters for three different radii (2.5, 1.25 and 0.626) mm.

Here, we report MSE (unit less) to be used as a comparative indicator between probe size and interface width. It is also used to obtain the insight that if the interface width is greater than 1 mm, any one of the three indenters can be used during an indentation experiment.

Finally, even though the elastic modulus has to change two orders of magnitude when cell phenotype changes from tendon to bone (shown in Figure 4.45 [64-65]), our approach provides a high degree of resolution for capturing dramatic TBJ stiffness changes in a relatively narrow interface region (600-400  $\mu\text{m}$ ). Therefore, accurate elastic modulus measurements of these scaffolds will greatly improve the process of manufacturing them, and also improve the ability to provide a standardized framework for both in vitro interactions between cells and scaffolds and in vivo tissue engineering studies.

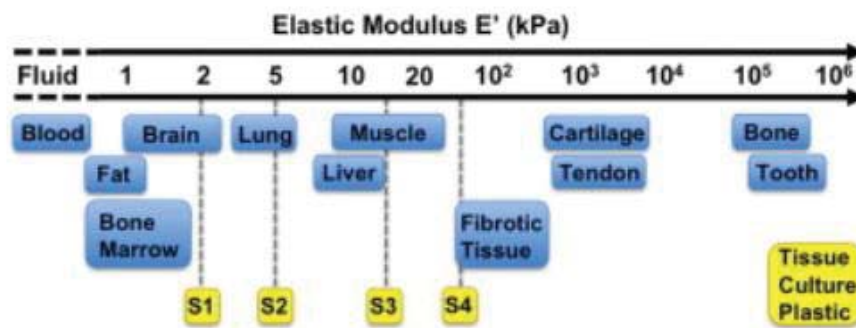


Figure 4.45: Plastic surfaces are currently used for the majority of cell and tissue cultures. S1, S2, S2, and S4 represent the substrates' stiffnesses [64].

#### 4.8 Conclusions and Directions for Future Research

This chapter addressed the limitations of indentation measurements when applied to multiple compartment-thin scaffolds with varying degrees of stiffness.

We presented a novel approach to processing macro-indentation data which significantly reduces the measurement error for scaffolds

with ramp interfaces. The intrinsic value of an elastic modulus around the interface can be obtained conveniently by solving the inverse problem after indentation measurements and the sigma values for the indenter are obtained. Sigma values are unique to indenter size and sample stiffness.

Therefore, sigma values developed from a step interface can be used for a ramp interface when the same stiffness levels are maintained (far from the interface). We have presented our technique, and evaluated it using FE models for both step interfaces and ramp interfaces. Further experimental testing has the potential to give us more confidence in this technique, and make this approach more robust and ready for use.

Applying numerical indentation methods to soft (500-2600 Pa) multi-compartment scaffolds, with heterogenic mechanical properties around the interface, leads to unreliable estimates of intrinsic elastic properties. Using our novel approach allowed us to reduce these effects and show that indentation with a hemispherical indenter probe (on the spatial scale of 1.25 mm) will yield improved measurements for multi-compartment scaffolds with an interface width of 400-600  $\mu\text{m}$ .

## **CHAPTER 5: CONCLUSIONS AND DIRECTIONS FOR FUTURE RESEARCH**

### **5.1 Conclusions**

The overall objective of this research was to characterize the elastic modulus at the interface region consisting of mineralized and non-mineralized type I collagen scaffolds. Our work focused on developing an indentation technique for the accurate measurement of the elastic modulus. This is done in order to precisely control and quantify stiffness changes throughout the scaffold, particularly at the interface region. In order to accomplish our objectives, we addressed two major challenges: The first challenge involved establishing a reliable measurement of elastic modulus for very soft (<1kPa) materials. (The non-mineralized part of the collagen scaffold has an elastic modulus between 300-800 Pa). The second challenge involved uncoupling the measurements from sample boundaries that arise out of, a) sample thickness, and b) the interface region due to material heterogeneity.

In order to address the first challenge, we used the hydrated indentation method (w/o surface adhesion) to measure the elastic modulus of gelatin. Because surface adhesion increases the measured forces, which is to be expected purely as a result of contact interaction between the probe and the sample under Hertzian contact assumptions, it must be eliminated.

Hydrated indentation is also introduced in the experiment to overcome the uncertainty in establishing the initial contact point between the sample and indenter probe.

This was important for the data reduction process using the Hertzian contact model. In order to verify the accuracy of the results, we compared the hydrated indentation measurements of the elastic modulus of gelatin with two other measurement techniques (indentation with surface adhesion and shear wave imaging). We chose gelatin hydrogel for conducting the comparison because it is linear isotropic for all measurements, and because its stiffness can be easily controlled by changing the gelatin concentration inside the hydrogel. The results for all of the measurements showed that all of the experimental techniques resulted in equivalent elastic modulus estimates (when the sample dimensions exceeded 10 times the indenter radius). The results also showed that the elastic modulus of gelatin is constant with load frequency, and thus quasi-static and dynamic measurements should be equal in the linear regime. The results also showed how each measurement was coupled with material and geometric properties of the gel sample in a unique manner. Therefore, we classified the material-geometry combination as a *sample system* so that we could focus on comparing indentation and shear-wave measurement techniques without developing methods to decouple the measurements from the sample geometry.

Finally, the consistency of the elastic modulus values led us to conclude that hydrated indentation with a sterile probe on the spatial scale of 1-5 mm could provide a reliable means of measuring an elastic modulus on homogeneous soft materials, once the effects of sample geometry are eliminated from the measurements.

Monolithic collagen scaffold were then indented using the knowledge we developed as a result of the first challenge. We used FE modeling and monolithic indentation of the scaffolds to show that the correction factor put forward by Dimitriadis, et al., is sufficient for correcting for elastic modulus measurement with sample thickness reduction.

We developed a new approach for addressing the influence of material heterogeneity on the indentation results for the multi-compartment scaffold. We used finite element simulation and performed a series of indentation across a step interface to learn that measurement bias is asymmetric with respect to the interface. We modeled the asymmetry and uncoupled the spread in the applied indenter force from the material interface using a shift-variant Gaussian filter. We found that the sigma values of the Gaussian filter descend across the interface from the stiffer side to the softer side.

Using the sigma values obtained from the forward solution of the step interface, we developed an inverse approach for correcting the indentation measurement bias near the continuously-varying interfaces between the mineralized and the non-mineralized regions.

We tested our technique using FE models for a range of scaffold-like stiffnesses and interface shapes in order to evaluate the impact of interface width and indenter size on the inverse solution. Our approach significantly reduced indentation measurement bias near the step interfaces by more than 60% when using a 2.5 mm-diameter hemispherical indenter. The improvement was more than 35% for a ramp interface using the same indenter size.

FE modeling gives us the ability to obtain insights about the impact of the indenter radius on the spatial resolution of the results.

We concluded that a probe on the spatial scale of 1.25 mm will yield improved measurements for the multi-compartment scaffolds, with an interface width of 600-400  $\mu\text{m}$  and a pore size of 90-131  $\mu\text{m}$ , which is very useful tool for aiding scaffold development for TBJ applications.

## **5.2 Possible Directions for Future Research**

We presented our novel technique for using macro indentation to measure the elastic modulus near the interfaces of multi-compartment scaffolds. Our evaluation was conducted using validated FE models. Extending this study to include additional testing will provide an additional level of confidence and might make this approach more robust and ready for use.

We have proven that macro indentation can be used as a reliable tool for accurately mapping spatial stiffness variations across an interface. However, our study was limited to elastic materials with controlled pore sizes and indentation rates. Evaluating our model under viscoelastic conditions in order to observe the effects on elastic modulus estimates can provide temporal stiffness maps. This will further improve the ability to engineer tissues for the purpose of eliciting a cellular response similar to that found at the TBJ.

## REFERENCES

- [1] Butcher D.T., Alliston T., Weaver V.M., 2009, “A tense situation: forcing tumour progression,” *Nat Rev Cancer*. 9(2), pp. 108-122.
- [2] Guillot C., Lecuit T., 2013, “Mechanics of epithelial tissue homeostasis and morphogenesis,” *Science*. 340(6137), pp. 1185-1189.
- [3] Yannas IV. “Tissue and organ regeneration in adults” New York: Springer; 2001.
- [4] Freyman TM, Yannas IV, Gibson LJ., 2001, “Cellular materials as porous scaffolds for tissue engineering” *Progress in Materials Science*. 46 (3-4), p 273-282.
- [5] Vickers SM. 2007, “Cell-seeded type II collagen scaffolds for articular cartilage tissue engineering”. PhD Thesis; Mechanical Engineering; Massachusetts Institute of Technology p. 241.
- [6] F.J. O’Brien, B.A. Harley, I.V. Yannas, L.J. Gibson, 2005, “The effect of pore size on cell adhesion in collagen-GAG scaffolds” *Biomaterials*. 26 (4), pp. 433–441.
- [7] O’Brien FJ, Harley BA, Yannas IV, Gibson LJ., 2004, “Influence of freezing rate on pore structure in freeze-dried collagen–gag scaffolds” *Biomaterials*. 25: pp. 1077–86.
- [8] O’Brien FJ, Harley BA, Waller MA, Yannas IV, Gibson LJ, Prendergast PJ., 2007, “The effect of pore size on permeability and cell attachment in collagen scaffolds for tissue engineering” *Technol Health Care*. 15: pp. 3–17.
- [9] C.-M. Lo, H.-B. Wang, M. Dembo, Y.-l. Wang. 2000, “Cell Movement Is Guided by the Rigidity of the Substrate” *Biophys J*, 79 (1), pp. 144–152.
- [10] N.D. Leipzig, M.S. Shoichet, 2009, “The effect of substrate stiffness on adult neural stem cell behavior” *Biomaterials*, 30 (36), pp. 6867–6878.
- [11] H.P. Wiesmann, U. Joos, U. Meyer. 2004, “Biological and biophysical principles in extracorporeal bone tissue engineering” Part II *Int J Oral and Maxillofacial Sur*, 33 (6), p. 523.
- [12] Mozdzen L.C. 2014, “DIFFERENTIAL HUMAN MESENCHYMAL STEM CELL RESPONSES ACROSS MULTICOMPARTMENT SCAFFOLDS FOR TENDON-BONE REGENERATION,” Master’s Thesis; Chemical Engineering; University of Illinois at Urbana-Champaign.
- [13] Gibson LJ, Ashby MF. 1997, “Cellular solids: structure and properties”. 2<sup>nd</sup> ed. Cambridge, UK: Cambridge University Press.

- [14] Harley, B.A., Leung, J.H., Silva, E.C., Gibson, L.J., 2007, "Mechanical characterization of collagen-glycosaminoglycan scaffolds" *Acta Biomaterials* 3, pp. 463–474.
- [15] Kanungo P.B., 2009, "Mechanical Properties of Collagen-Based Scaffolds for Tissue Regeneration, engineering" PhD Thesis; Material Science and Engineering; Massachusetts Institute of Technology.
- [16] Caliarì R.S., 2013, "The Influence Of Collagen-Gag Scaffold Architectural And Biological Cues On Tenocyte And Mesenchymal Stem Cell Bioactivity For Musculoskeletal Tissue Engineering" Ph.D Thesis; Chemical Engineering; University of Illinois at Urbana-Champaign.
- [17] Weisgerber D.W., Kelkhoff D.O., Caliarì S.R., Barley B.A., 2013, "The impact of discrete compartments of multi-compartment collagen-GAG scaffold on overall construct biophysical properties" *Journal of the Mechanical Behavior of Biomedical Materials*, 28, pp. 26-36.
- [18] Harley B.A., Freyman T.M., Wong M.Q., Gibson L.J., 2007, "A New Technique for Calculating Individual Dermal Fibroblast Contractile Forces Generated within Collagen-GAG Scaffolds," *Biophys J.*, 93, pp. 2911-2922.
- [19] Gibson LJ, Ashby MF. *Cellular solids: structure and properties*. 2<sup>nd</sup> ed. Cambridge, UK: Cambridge University Press; 1997.
- [20] Freyman, TM, Yannas, IV, Pek, Y-S, Yoko, R, Gibson. LJ, 2001, "Micromechanics of fibroblast contraction of a collagen-gag matrix" *Exp. Cell Res.*, 269: pp. 140–53.
- [21] Kanungo B.P., Silva E., Van Vliet, K. Gibson L.J., 2008, "Characterization of mineralized collagen-glycosaminoglycan scaffolds for bone regeneration," *Acta Biomaterials* 4: pp. 490–503.
- [22] Martínez-Díaz S., García-Giralt N., Lebourg M., Gómez-Tejedor J., Vila G., Cáceres E., Benito P., Monleón Pradas M., Nogues X., Ribelles J. G., Monllau J.C., 2010, "In Vivo Evaluation of 3-Dimensional Polycaprolactone Scaffolds for Cartilage Repair in Rabbits" *Am J Sports Med*, 38: pp. 509-519
- [23] Gershuni DH, Kuei SC., 2005, "Articular cartilage deformation following experimental synovitis in the rabbit hip" *J Orthop Res*; 1 (3): pp. 313-318.
- [24] Hoch DH, Grodzinsky AJ, Koob TJ, Albert ML, Eyre DR., 1983, "Early changes in material properties of rabbit articular cartilage after meniscectomy" *J Orthop Res*. 1(1): pp. 4-12.
- [25] Parsons JR, Black J., 1977, "The viscoelastic shear behavior of normal rabbit articular cartilage" *J Biomech*. 10(1): pp. 21-29.
- [26] Yanxia Zhu, 2001, "Determination of mechanical properties of soft tissue scaffolds by atomic force microscopy nanoindentation" *J of biomechanics*, 44(13), pp. 2356-2361.

- [27] Harley BA., 2006, "Cell-matrix interactions: collagen-gag scaffold fabrication, characterization, and measurement of cell migratory and contractile behavior via confocal microscopy." Sc.D. Thesis, Massachusetts Institute of Technology, Cambridge, MA. pp. 199–256.
- [28] Harley BA, Zaman MH, Kim H-D, Yannas IV, Gibson LJ. Study of cell behavior in 3d: quantification of individual cell migration and contraction behavior within a well-characterized collagen– glycosaminoglycan scaffold. In: Proceeding of the first international conference on mech. of biomaterials & Tissues, Kona, HI; 2005.
- [29] Farrell E., O'Brien F.J., Doyle P., Fischer J., Yannas I., Harley B.A., O'Connell B., 2006, "A collagen–glycosaminoglycan scaffold supports adult rat mesenchymal stem cell differentiation along the osteogenic and chondrogenic routes" *Tissue Eng*, 12: pp. 459–68.
- [30] Harley BA, Lynn AK, Wissner-Gross Z, Bonfield W, Yannas IV, Gibson LJ. Design and fabrication of a multiphase osteochondral scaffold. In: Proc. First Intl. Conf. on Mech. of Biomaterials & Tissues, Kona, HI; 2005.
- [31] Azeloglu E.U., Costa K.D., 2011, "Atomic force microscopy in mechanobiology: measuring microelastic heterogeneity of living cells," *Methods Mol Biol*. 736, pp. 303-329.
- [32] Heinisch JJ, Lipke PN, Beaussart A, El Kirat Chatel S, Dupres V, Alsteens D, Dufrêne YF., 2012, "Atomic force microscopy - looking at mechanosensors on the cell surface," *J Cell Sci*, 125(Pt 18): pp. 4189-4195.
- [33] Hertz, H., 1882. Über die Berührung fester elastischer Körper. *Journal für die Reine und Angewandte Mathematik* 92, 156–171. [34] Dimitriadis E. K., Horkay F., Maresca J., Kachar B., Chadwick R. S., 2002, "Determination of elastic moduli of thin layers of soft materials using atomic force microscope. *Biophys J.*, 82, pp. 2798-2810.
- [35] Johnson K. L., Kendall K., Roberts A.D., 1971, "Surface energy and contact of elastic solids," *Proc R Soc London, A*, 324, pp. 301-313.
- [36] Lin, D.C., Dimitriadis, E.K., Horkay, F., 2007, "Robust strategies for automated AFM force curve analysis-II: Adhesion-influenced indentation of soft, elastic materials," *J Biomech Eng*. 129(6), pp. 904-912.
- [37] Oyen, M.L., Cook, R.F., 2009, "A practical guide for analysis of nanoindentation data," *J Mechan Behavior Biomech Mat*. 2(4), pp. 396-407.
- [38] L. D. and E. M. Lifshitz, *Theory of Elasticity* (1959).
- [39] Valentin L. Popov: *Contact Mechanics and Friction: Physical Principles and Applications*, 2010

- [40] Rajarashi R., Desai J.P., 2014, "Determination of Mechanical Properties of Spatially Heterogeneous Breast Tissue Specimens Using Contact Mode Atomic Force Microscopy(AFM)". *Annals of Biomedical Engineering*, 42(9), pp. 1806–1822.
- [41] Long, R., M. Hall, M. Wu., and C-Y Hui., 2011, "Effect of gel thickness on microscopic indentation measurements of gel modulus". *Biophys. J.* 101 (3): pp. 643-650.
- [42] Hand book of Micro/Nanotribology, ed. Bharat Bhushan, CRC Press N.Y., 199, p.269.
- [43] Ebenstein D.M., Wahl: K.J., 2006 "A comparison of JKR-based methods to analyze quasi-static and dynamic indentation force curves," *J Colloid Interface Sci*, 298, pp. 652-662.
- [44] Deuschle S. E., Arzt E., Surface detection in nanoindentation of soft polymers, *Mater. Res.*, Vol. 22, No. 11, Nov 2007.
- [45] G. Lewis and J.S. Nyman, 2008, "The use of nanoindentation for characterizing the properties of mineralized hard tissues":State-of the art review. *J. Biomed. Mater. Res. Part B* 87B, p. 286.
- [46] J.D. Kaufman, G.J. Miller, E.F. Morgan, and C.M. Klapperich, 2008, "Time-dependent mechanical characterization of poly(2-hydroxyethyl methacrylate) hydrogels using nanoindentation and unconfined compression". *J. Mater. Res.* 23, p. 1472.
- [46] O. Franke, M. Goken, and A.M. Hodge, 2008, "The nanoindentation of soft tissue: Current and developing approaches". *JOM* 60, p. 49.
- [47] A.B. Mann and J.B. Pethica, 1996, "Nanoindentation studies in a liquid environment". *Langmuir* 12, p. 4583.
- [48] Burnham, N.A., Colton, R.J., and Pollock, H. M.,1991, "International Issues in Force Microscopy", *J. Vac. Sci. Technol. A*, 9(4), pp. 2548-2556.
- [49] Ebenstein D.M., Pruitt L.A., 2006, "Nanoindentation of biological materials," *Nano Today* 1(3), pp. 26-33.
- [50] Ebenstein D.M., 2011, "Nano-JKR force curve method overcomes challenges of surface detection and adhesion for nanoindentation of a compliant polymer in air and water" *J. Mater. Res.* 26 (8), pp. 1026-1035.
- [51] Guillonneau G., Kermouche G., Bec S., Loubet J. 2012, "Determination of mechanical properties by nanoindentation independently of indentation depth measurement". *Journal of Materials Research, Materials Research Society*, 27, pp. 2551-2560.
- [52] Qiang B., Greenleaf J., Oyen M.L. Zhang X., 2011, "Estimating material elasticity by spherical indentation load relaxation test on viscoelastic sample of finite thickness," *IEEE Trans Ultrason Ferroelect Freq control*, 58(7), pp. 1418-1429.

- [53] Sun Y., Akhremitchev B., Walker G.C., 2004, "Using the Adhesive Interaction between Atomic Force Microscopy Tips and Polymer Surfaces to Measure the Elastic Modulus of Compliant Samples", *Langmuir*, 20, pp. 5837-5845.
- [54] Orescanin M., Insana M., 2010, "Shear modulus estimation with vibrating needle stimulation," *IEEE Trans Ultrason Ferroelectr Freq Control*, 57(6), pp. 1358-1367.
- [55] Wang Y., Shemonski N.D., Adie S.G., Boppart S.A., Insana M.F., 2013, "Dynamic method of optical coherence elastography in determining viscoelasticity of polymers and tissues," *Proc IEEE Eng Med Biol*, pp. 117-120.
- [56] Gilsenan P.M., Ross-Murphy S.B., 2001, "Shear creep of gelatin gel from mammalian and piscine collagens," *Int J Biol Macromol*, 29, pp. 53-61.
- [57] Orescanin M., Toohey K., Insana M.F., 2009, "Material properties from acoustic radiation force step response," *J Acoust Soc Am*, 125(5), pp. 2928-2936.
- [58] Sridhar M., Liu J., Insana M.F., 2007, "Elasticity imaging of polymeric media," *ASME J Biomechan Eng*, 129(2), pp. 259-272.
- [59] Barr R.G., 2012, "Sonographic breast elastography: a primer," *J Ultrasound Med*, 31(5), pp. 773-783.
- [60] Sarvazyan A.P., Rudenko O.V., Swanson S.D., Fowlkes J.B., Emelianov S.Y., 1998, "Shear wave elasticity imaging: a new ultrasonic technology of medical diagnostics," *Ultrasound Med Biol*, 24(9), pp. 1419-1435.
- [61] Veis, A., *The Macromolecular Chemistry of Gelatin*, Academic Press, New York. 1964.
- [62] SIMULA online documentation ABAQUS version 6.13, 2013.
- [63] [http://en.wikipedia.org/wiki/Tikhonov\\_regularization](http://en.wikipedia.org/wiki/Tikhonov_regularization)
- [64] Skardl A., Mack D., Atala A., Soker S., 2013, "Substrate elasticity controls cell proliferation, surface marker expression and motile phenotype in amniotic fluid-derived stem cells" *J. of the Mechanical Behavior of Biomedical Materials*, 17, pp. 307-316.
- [65] Engler A.J., Griffin M.A., Sen S., Bonnemann C.G., Sweeney H.L., Discher D.E., 2013, "Myotubes differentiate optimally on substrates with tissue-like stiffness: pathological implications for soft or stiff microenvironments" *J. Cell Biol.*, 166 (2004), pp. 877-887
- [66] SIMULA online documentation ABAQUS version 6.12, 2012.